University of Birmingham

Zoe Schofield

Experimental and Computational Investigation of The Mechanisms behind Deep Vein Thrombosis

24/Sept/2019

EXPERIMENTAL AND COMPUTATIONAL INVESTIGATION OF THE MECHANISMS BEHIND DEEP VEIN THROMBOSIS

by

ZOE SCHOFIELD

A thesis submitted to
The University of Birmingham
for the degree of
DOCTOR OF PHILOSOPHY

School of Chemical Engineering
College of Engineering and Physical Sciences
The University of Birmingham
24/Sept/2019

Abstract

Deep vein thrombosis (DVT) is a life threatening condition which is on the rise in the western world [1] yet the mechanisms behind DVT remain unknown. Using microfluidics and simulations it is possible to determine the physical mechanisms that could be the cause of DVT. By mimicking the murine model (stenosis model) it was possible to see if the amount of stenosis and presence of side branches influenced flow. I was determined that the influence of a restriction did not alterr the flow enough to encourage thrombus formation, however the stenosis would increase the number of cell-cell collisions which could be the reason for a thrombus occurring *in vivo*. Finite element modelling was also used to surpass the limitations of the experiment, resulting in a the same conclusions. A major limitation of the murine model is that it ignores the possibility of a bypass of the stenosed region, leading to the second model.The bypass model was used to determine which set of parameters are important to encouraging a bypass: position of side branch, width of side branch channel and the size of stenosis. Finally, a third model was also developed, the valve model to explore how flow is influenced by flexible valves. The valves are fabricated with varying stiffness to better understand how the stiffness of valves can influence flow through a vein inducing pro-thrombotic conditions. This model is more relevant for larger mammals. Three models of biology have been implemented to demonstrate DVT can be instigated by physical parameters and these fundamental conditions are not to be dismissed.

ACKNOWLEDGEMENTS

Throughout my PhD I have had the pleasure to work alongside some outstanding researcher's and staff. Firstly I would like to thank the outstanding supervision of Dr. Daniele Vigolo, who has supported, guided and advised me through every aspect of my PhD and career choices. I could not ask for a better primary supervisor, his patience and encouragement has undoubtedly inspired me for my future career in academia. I would also like to thank my secondary supervisors: Dr. Alessio Alexiadis for his patience with computational aspects of my work as well as providing me with teaching opportunities within his module. Dr. Alexander Brill for his enthusiasm towards the project and constant drive towards publications and future experiments. And finally, Professor Gerard Nash, as without his experience and knowledge of academia would not have been able to rationalise expectations of the project. Collectively, my supervisors helped to keep my motivation and enthusiasm for the project.

My research would have not have been possible without the support of my friends, including the routine enforced by Twelve O' Clock Lunch Crew in my final year. I would also like to acknowledge Meg Cooke, Kamlesh Patel and Daniel Lighter, the writing and pizza nights, the late nights in the office in final year and the stressing in unison reminded me I was not alone in this journey. I would also like to acknowledge Birmingham Moseley Womens Rugby team as it is not only friends made in academia that provide support and encouragement.

Finally I would like to thank my partner Richard Kidson and Family both of which have been equally there in moments of need. My PhD has been a roller-coaster of emotion and knowing I have an exceptional family and partner has ensured my success in completing this thesis.

CONTENTS

LIST OF FIGURES

LIST OF TABLES

ABBREVIATIONS

BP - Bypass

CAD - Computer aided design

CCD - Charge coupled device

CFD - Computational fluid dynamics

CMOS - complimentary metal oxide semiconductor

D - Diameter

d - depth of valve (μm)

DDM - Differential dynamic microscopy

DLS - Dynamic light scattering

DMHS - Discrete multi-hybrid system

DVT - Deep vein thrombosis

E - Young's Modulus

FE - Finite element

FEM - Finite element methods

GPV - Ghost particle velocimetry

H - Device width

IVC - Inferior vena cava

$\mathbf{L}_p$ - Length of pump geometry (Bypass Design)

MCB4 - Main channel before side branch

MC Aft SB - Main channel after side branch (but before stenosis)

MC AftSten - Main channel after stenosis

MRI - Magnetic resonance imaging

NA_c - Numerical Aperture of the condenser lens

PDMS - poly(dimethylsiloxane)

PE - Pulmonary embolism

PEGDA - polyethylene glycol-*di*acrylate

PI - Photo initiator

PIV - Particle image velocimetry

PRP - platelet rich plasma

PS - Poly-styrene

rPSGL-Ig - recombinant P-selectin glycoprotein ligand Ig

PTV - Particle tracking velocimetry

RAM - Risk assessment models

R - Radius of cylinder design

r - Radius of stenosis of cylinder design

Re - Reynold number

ROI - Region of interest

SB - Side branch

T- Time

UV - Ultra-Violet

μPIV - micro particle image velocimetry

W - Device width (μm)

W_{SB} - width of side branch

ρ - Density (kg/m^3)

CHAPTER 1

INTRODUCTION

1.1 Background

Deep vein Thrombosis (DVT) is a painful and dangerous condition where blood clots within the deep veins (e.g. common femoral vein). The clots can become unstable and travel to the lungs resulting in a life threatening condition called a pulmonary embolism (PE). DVT and PE combined cause 25,000 deaths annually in the UK [6], yet the physical mechanisms behind DVT remain unknown. This is due to the lack of *in vitro* research behind the physical parameters encouraging thrombus formation. It is believed that venous valves play a fundamental role into the development of a thrombus either: behind the valve flaps or on the leaflet itself. However, it is has not been determined where or how a thrombus is initiated within the deep veins. Using fundamental fluid dynamics used daily in engineering it is possible to investigate various possibilities into how DVT occurs and grows within a venous system. In industry, fluid dynamics is rudimental for the designing, understanding and the running of many chemical plants from: cosmetic, pharmaceutical, house hold and oil to name a few. From the initial designing of a chemical plant, it is first considered how fluid will be transported around the plant from reagents to packaging.

The physiology of the cardiovascular system can be considered as a complex network of pipelines with varying diameters and two pumping systems: the cardiac pump (heart) for arterial flow and the skeletal muscle pumps for venous flow. Thinking from a physical

science perspective, and stripping away biology it is possible to model and understand complex flow patterns within the venous system. Engineers have to consider many parameters of fluid properties: the viscosity, Newtonian/non-Newtonian characteristics, composition, temperature dependencies [7] to plant design: the diameter and roughness of the piping, positioning of pumps and valves [7]. All of these factors contribute to the smooth transportation of fluid around the plant and aim to reduce blockages forming. It is also a lot easier to make minor alteration to the pipework to improve efficiency of the plant, both of which are not possible in nature. However, it is possible to use the theories and technology intended for physical sciences and apply them to a biological problem. Throughout this thesis it shall be explained how physical sciences can be used to highlight potential pro-thrombotic conditions in DVT.

Currently there is plentiful research into arterial and heart related cardiovascular diseases yet the venous system is under appreciated. It is only until recently that DVT has become a topical research focus for the NHS. The main risk factors are: old age, immobility (bed ridden after surgery, long haul flights, etc) and pregnancy. Obviously, all risk factors are increased when combined with old age. There is a dramatic, increased risk of DVT in patients over the age of 50 increasing from 1-3 individuals per 1000 to 1 in 100 annually in the United States[8]. Current methods for determining the prognosis of DVT is a risk assessment model (RAM) scoring approach [9]. This technique relies on electronic records being up to date to develop a data base to aid diagnosis as well as predicting the likelihood of developing DVT. However, these systems are less than accurate and there is vast room for improvement. In an attempt to improve the scoring systems D-dimer and p-selectin bio-markers were added in order to assess the risk of developing DVT [9]. However, in order to progress the scoring system further it would be useful to understand how geometry of veins and valves influence clot formation. It is hypothesised that there is a link between venous geometry and flow characteristics correlating to thrombus formation[10]. Despite the increase in identification and treatment of DVT the number of people developing this disease is increasing annually in the western population[11]. Current systems are not sufficient enough for initial diagnosis, as

the criteria is far too vague. This means there needs to be a better, non-invasive alternative. This can be carried out by determining biophysical predictors which can be visualised using ultrasound doppler techniques [12].

The cardiovascular system is a complex network of blood vessels (figure 1.1 A). The physiological differences between the vessels is to ensure the efficiency of blood flow around the body (figure1.1 B). Typical diameters,D, of veins and arteries depend on where in the body they are located, sex, age, weight etc and shall be discussed later in section 1.2.

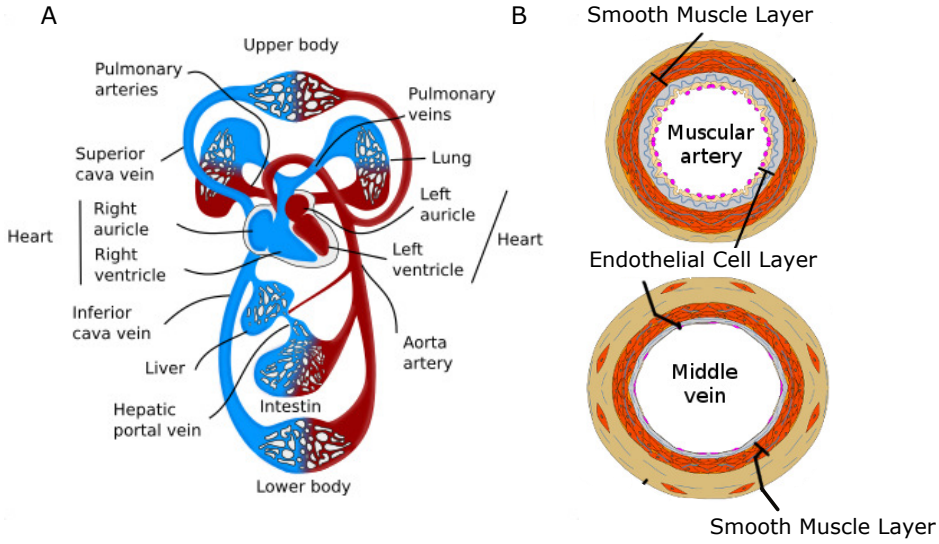

Figure 1.1: A schematic of the cardiovascular system and vessel physiology. Adapted from [2]

Arterial flow is pumped by the cardiac muscle (heart) around the body at high pressure (represented in red in figure 1.1), in order to withstand this pressure the arteries have a thick layer of smooth muscle compared to veins [13] which maintains the shape of the artery. The increased rigidity of the arteries also helps maintain the pressure of the blood ensuring it reaches the capillaries. The capillaries have a significantly reduced vessel diameter. The decrease in diameter results in a pressure drop after the capillaries [14]. The capillaries are at the end of the arterial network and therefore the pressure exerted at the beginning by the heart has now been exhausted by the time it reaches veins. The capillaries have a vessel wall that is only one endothelial cell thick, meaning they cannot withstand high pressures without rupturing. The endothelial cells enable the transfer of oxygen to surrounding tissues,

and the removal of carbon dioxide created in aerobic respiration [14]. As the blood is now at a significantly reduced pressure, the veins have to be specialised to enable the return of blood back to heart. Venous blood vessels only have a small layer of smooth muscle (figure 1.1) making the walls very flexible, this is beneficial as venous flow is dependent on the contraction of surrounding muscles (figure 1.2). Another feature present in veins is valves, the valves prevent back flow of blood and open and close in an alternate fashion (i.e. one valve opens as the previous one closes), figure 1.2.

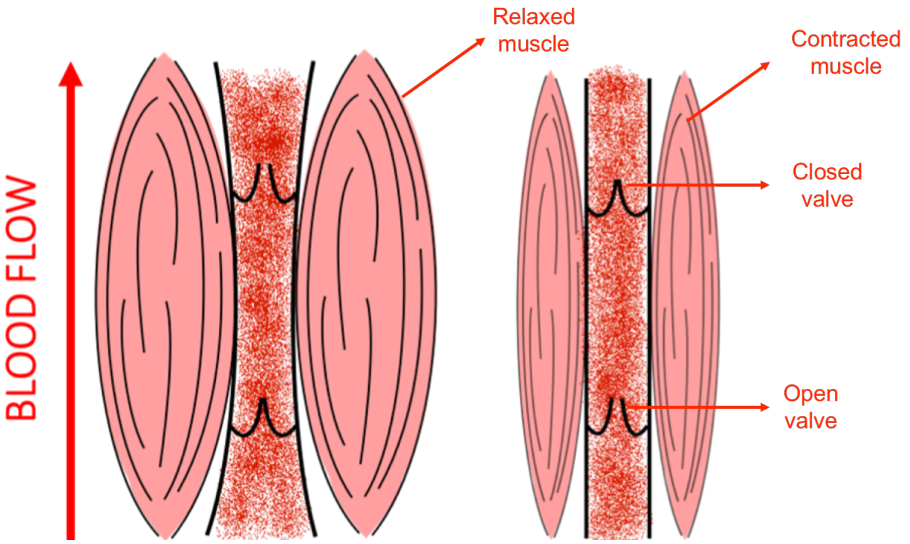

Figure 1.2: A schematic of how the muscle contraction pump works. One valve opens as the one behind closes to prevent back flow. Not to scale

The physiological differences between arterial and venous blood vessels are important factors to consider when trying to understand mechanisms behind thrombosis. It can be assumed that *in vitro* models to represent arterial thrombosis are not relevant when trying to understand venous thrombus formation. Further evidence supporting the assumption that there are two mechanisms behind thrombus formation for arteries and veins. The differing in mechanisms behind thrombosis alter the composition of the thrombus. Blood clots contain a mixture of platelets, fibrin and red blood cells [8]. Importantly, the combination of these cells/proteins highly depend on where the blood clots are formed under specific conditions. Arterial thrombus formation occurs under high wall shear stress conditions ($20-30 N/cm^2$) [15], and is usually a result of damage to the vessel wall or after an atherscle-

rotic plaque. They are platelet rich and generally treated with an anti-platelet drug [8]. This is different to thrombus formation within the veins, as thrombus formation occurs at lower shear stress condition ($1-2N/cm^2$) and is generally fibrin rich and containing majority red blood cells with a platelet head and is therefore treated with anticoagulants [8].

In 1884 Virchow proposed a triad of conditions which would increase the likelihood of thrombus formation (see figure 1.3) [11]. It became the fundamental understanding behind thrombosis progressing advancing research for over 20 years triggering research into looking at vessel damage [16, 17, 18, 19], activation of platelets, [20, 21, 22, 23] and stasis [24, 25, 26].

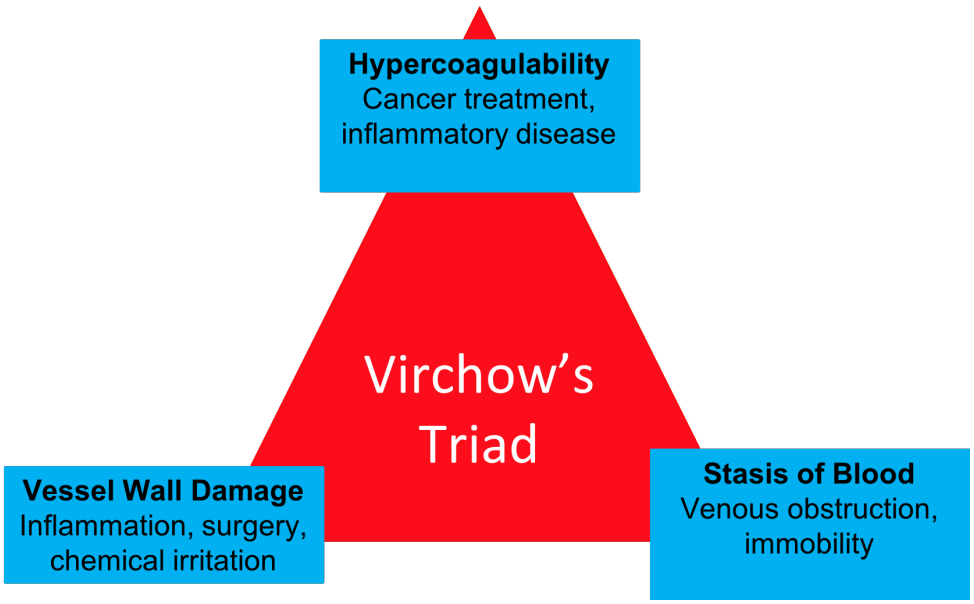

Figure 1.3: A diagram illustrating Virchow's Triad

However, thrombosis within veins is not a result of vessel damage as it is not under high pressure. Primarily DVT is caused by stasis and hyper-coagulability as mentioned previously. Once a person is diagnosed with DVT, they are at a higher risk of developing DVT again indicating that it is a geometrical influence on flow that promotes thrombus formation [11]. There could also be physiological differences that develop with age. It has been said that the older population have an increased reactivity of platelets [27]. The reason for the increased reactivity is unknown, and could be a result of many physical factors: stiffening of blood vessels, change in blood rheology or stiffening of venous valves. All of which will re-

sult in changes to the flow patterns within veins, changing flow conditions around the venous valve. A change in flow pattern could be a larger stagnant region behind the valve, in the valve sinus. This large area of stasis would encourage clot formation because blood is a non-Newtonian fluid, meaning when blood is stagnant it will thicken and eventually clot. Valve stiffness has been investigated for cardiac flow [28] and even more recently for venous valves [29]. Both indicate that valve stiffness increases with age. Another suggestion could be that with the increased stiffness of the blood vessels, degradation of muscle tissue in the lower extremities could reduce the amount of blood flow through the deep veins and result in pooling behind the valve pocket.

1.2 Current *in vivo* Models

Research into mechanisms behind DVT is limited to physical and chemical interventions to induce thrombus formation in a variety of animal models [30, 10, 31].

Table 1.1: Typical diameter of *in vivo* veins and study

Animal	**Diameter of Vein**	**Valves Present (Y/N)**	**Study**	**Reference**
Mouse	200 μm	NA	Stenosis of inferior vena cava to model DVT	[32]
Mouse	NA	Not Mentioned	Stenosis of inferior vena cava to model DVT	[33]
Mouse	NA	Not Mentioned	Stenosis of inferior vena cava to model DVT	[26]
Rat	3 mm	N/A	Stenosis of inferior vena cava to mode DVT	[34, 35]
Pig	1.5 cm	Y	Jugular Vein Stenosis. The degree of stenosis and the influence on the mass of a thrombus.	[10, 30, 36]
Pig	NA	NA	Applying a stenosis to IVC of a pig in combination with thrombin as a model for DVT	[37]
Dog	$\approx 0.8cm$	Y	Right jugular vein stenosis. An animal model for spontaneous PE from DVT	[38]
Dog	NA	NA	Fast-ultrosonography of the vena cava in dogs	[39]
Dog	NA	NA	Investigation of cane venous structure	[40]
Baboon	NA	Y	Inferior vena cava balloon occlusion	[41, 42]
Human	8.42 mm	Y	Common Femoral Vein. Investigation into vessel diameter depending on sex, age, weight.	[43]
Human	8.55 mm	Y	Superficial Vein. Investigation into vessel diameter depending on sex, age, weight.	[43]
Human	11.07 mm	Y	Jugular vein. Investigation into vessel diameter depending on sex, age, weight.	[43]

1.2.1 Murine Model

The most established model for investigating DVT is the murine model as it is the most simple, reproducible, controllable *in vivo* methodology [44]. However mice are not susceptible to thrombus formation, meaning that they have to be genetically modified to induce thrombosis. Genetic modification can also be advantageous as it enables research in t the identification of biomarkers. Usually these studies are compared to a wild type mouse [45, 46, 47]. The studies have been beneficial for highlighting specific genes and bio-molecules that are important to the development of DVT. The methodology is well established and originally involved the full ligation of the inferior vena cava, IVC (see figure 1.4 A). This will stop blood flow completely through the IVC and therefore result in the formation of a thrombus. Further development of this model has involved the partial restriction of the IVC, known as a stenosis as seen in figure 1.4 B. The IVC is a popular choice as it is the largest vein in a mouse [44]. The full ligation of the IVC ensured the reproducibility of thrombus size and weight, allowing for specific investigation of biochemical markers of DVT [45, 48, 49], however this is not true for the stenosis model [33]. The reason for this is that the needle used to apply the stenosis may not be blunted which could cause injury to the vessel wall [44]. Yet both have been pioneering for understanding the chemistry behind thrombus formation and have aided drug development.

The murine model has briefly looked at geometric influences on thrombus formation. One particular study investigates the presence of back branches and side branches on the size of thrombus. J. Diaz et al found that thrombus formation was reduced when back branches were not ligated [33]. It is hypothesised from this study that the back/side branches are important to thrombus formation and that their presence disrupts flow within the IVC [33]. It was also found that when the IVC is stenosed, and all back/side branches are closed, the thrombus formed weighs more ($\approx$32 mg) than in conditions where only the back or side branches are closed (not both) [33]. This is interesting as it suggests that again flow will not only determine whether a thrombus will form but also how big the thrombus will become with in the same time scale. Since the study carried out by J. Diaz et al there has been no

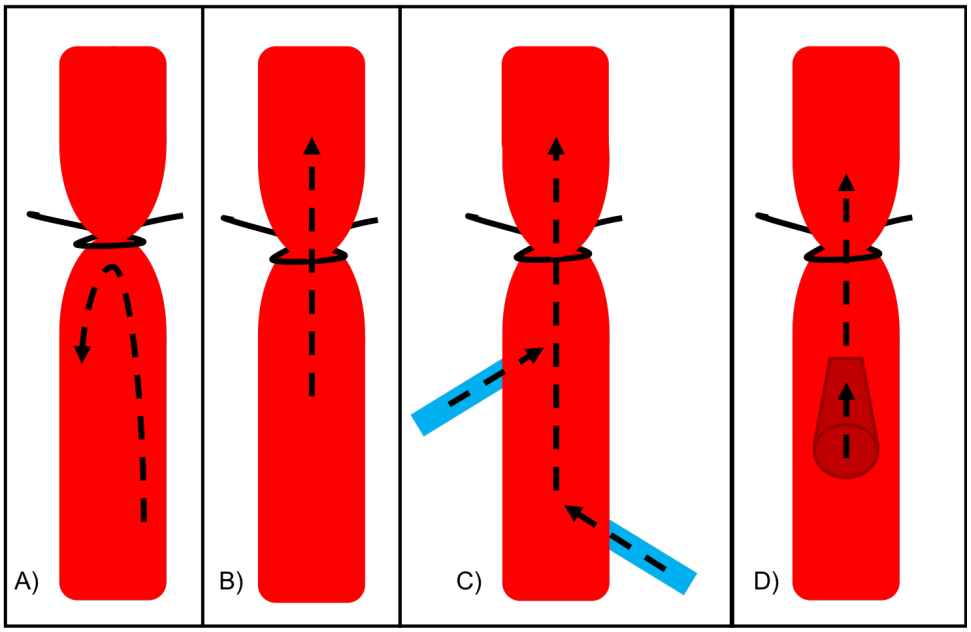

Figure 1.4: Schematic images indicating the differences between A) a full ligation, B) a stenosis as well as showing the presence of C) side branches highlighted in blue and D) back branches in dark red.

further investigation into the influence of side branches and its effect on thrombosis. Therefore, within this thesis, this will be starting point for investigating DVT as the presence of side and back branches may not disrupt flow, but could be providing a bypass route back to the heart. In the stasis models (full ligation of the IVC) the mouse is alive while the thrombus forms suggesting there is an alternative route back to the heart.

The murine model dominates research into DVT due to its technical simplicity and reproducibility [31]. Unfortunately it is unable to determine the physical predictors due to the complication of *in vivo* imaging of blood flow. A thrombus can be detected as early as 3 hrs after the surgical procedure, however typically thrombi are measured after 48 hrs [44]. This large time gap between when they can detect a thrombus to when they are typically measured suggests there is limited understanding behind how a thrombus is initiated and the growth rate. Imaging blood flow *in vivo* is a major hindrance of understanding the physical mechanisms behind DVT. As mentioned previously blood does not exhibit optical transparency, therefore fluorescently labelled platelets are required to track the velocity through the vein. A popular approach for measuring DVT is intravital microscopy [50]. Usually intrav-

ital microscope uses confocal microscopy allowing for 3D imaging of the blood flow through the vein, however, within these studies it is not stated which plane the flow of platelets is being investigated. This means the platelets can be at the vessel wall, where the velocity is slow, or in the centre, where the velocity would be at its highest. Therefore the ability to compare findings between these studies is relatively restricted. Intravital microscopy allows for the investigation of blood flow *in vivo* whilst the animal is still alive [51]. In the case of investigating blood flow in the murine model, platelets are generally fluorescently labelled [45]. An interesting study implemented intravital microscopy to investigate the growth and composition of thrombus formation in mice. To induce thrombus formation ferric chloride was used to induce injury to the vascular wall of the venules [52]. It was found that thrombus formation occurred in a matter of minutes, differently to what has been reported in other studies where hours have been waited before thrombus composition has been studied.

To reiterate, a major drawback to the IVC stenosis model is the inability to reproduce thrombus size and weight for accurate pharmaceutical studies [53]. It would be ideal for thrombus formation and growth to be predictable and therefore more work needs to be carried out to determine the mechanisms behind DVT. Throughout the majority of the stenosis models there is a lack of consideration for the possibility of a bypass. Yet it is reported that even if there is full ligation of the IVC in a mouse it will behave normally, and not be impaired with the stopped blood flow through a major vein for at least a day [44]. Mice are obviously physiologically and genetically different to humans meaning that the mechanisms behind thrombosis will be different [54]. Another important factor is that the IVC runs horizontally along the mouse to the heart and therefore will lack gravitational effects which would be possible in larger animals and humans. It has not yet been reported whether or not mice have valves within their venous network, yet it is believed they play an important role in DVT in humans. For this reason, more research needs to be carried out investigating blood flow around valves in order to understand how and where thrombosis occurs within the venous network.

1.2.2 Large Mammal Models

The use of larger animals ensures a better representation of humans for pharmaceutical development and investigation into mechanisms behind DVT. It was found that with a greater stenosis (80-90%) there is an increased probability of the occurrence of a thrombus in pig models [10]. The time scale for these experiments varied from 2 hours to 5 days depending on the intervention inducing thrombus [10].

It is thought that most venous thrombi originate in the valve pockets as a result of low oxygen tension, and they develop over a period of hours – days [44]. The large variability in time scales indicates no one truly knows how DVT is initiated or propagates. In order to study thrombus formation which are more physiologically relevant to the human disease, DVT, larger mammals need to be investigated [55]. Larger mammals generally have valves in order to get the blood back to the heart and prevent back flow. There is not yet an *in vitro* model allowing for this investigation.

The canine model mentioned in table 1.1 temporarily stops blood flow through a 3 cm section of the right jugular vein, however there is no mention of the vein reaching normal diameter after the clamps are removed [38]. Although the dogs were treated with sodium morrhuate which is a drug diagnosed to help with vein dilation, there is no report on how each dog is affected [38]. This could be the reasons for why there appears to be no clear correlation between thrombus weight and age. The data is complimentary to other findings in that there is obviously geometry influences the size and weight of the thrombus over time as this is missing in their comparative study and the results focus on how large deviations occur depending on human interpretation, weight and age of the thrombus and weight of the dog [38].

The same can be said for the study carried out on baboons which, similarly to the murine model, had thrombosis induced by blocking their renal IVC for 6 hrs [41]. The main focus of this study was to understand the role of P-selectin in thrombus formation. In order to do this, 8 of 12 baboons were injected with recombinant P-selectin glycoprotein ligand Ig (rPSGL-Ig) which has a high affinity to P-selectin, thus reducing the effect of P-selectin [41, 18]. However,

it fails to report if there is a difference in IVC diameter, and although this may have been disregarded as irrelevant due to the promising and consistent results from the mouse model, it could have been an obvious reason to why there were inconsistent results within this study. Albeit, the baboons underwent full occlusion of the IVC for 6 hrs, which is not representative of how thrombosis occurs. Therefore, a further study could investigate a partial stenosis to emulate a constricted vein and the effectiveness of rPSGL-Ig in correlation with vessel diameter and degree of constriction.

A blatant observation from table 1.1 is the lack of information regarding vessel diameter and presence of valves. The majority of *in vivo* research seems to disregard the possibility that vein diameter and venous valves are an important factor when looking into thrombus formation and yet it is a fundamental physiology for the efficient, continuous blood flow around the body; human, non-human, small and large animals. This can be standardised and controlled using an *in vitro* approach. In addition, another limitation to current *in vivo* models is that in order to induce thrombus formation there has to be a physical (stenosis), chemical or genetic intervention [31]. The stenosis model in particular induces thrombus formation by forming a 'bottle neck' increasing the cell-cell interaction and therefore encouraging the initiation of thrombosis.

As hinted at previously, within the murine model the animals have a fully ligated IVC which is the largest vein within a mouse yet they survive for many hours [53]. Even in the stenosis model where the thrombus fully blocks the IVC the mouse is only euthanised 48 hours after the stenosis [45]. The mice remain alive and although their activity is not reported it are presumed unaffected by the blockage otherwise the time before euthanasia would be brought forward. This indicates that there must be an alternative route back to the heart bypassing the obstruction. The idea of a bypass has been underestimated when it comes to using the murine model to understand physical mechanisms behind thrombosis. It was reported that the presence of side branches and back branches reduced the size and probability of developing a thrombus due to recirculation around the stenosed region [53]. Although this is very unlikely to be true due to the size and properties of blood within a

mouse being laminar (discussed in greater detail in sections 1.3.1 and chapter 3).

Unfortunately the presence of a bypass in humans may not be as obvious, although blood does make its way back to the heart. When a patient has been diagnosed with DVT one of the symptoms is swelling and pain of the limb. This swelling is due to a build up in pressure within the smaller veins and capillaries causing severe pain. The pressure build up could be caused by ageing veins having a decreased elastic tissue. A decrease in elastic tissue would mean that the veins are more prone to compression [58, 59], inducing a similar effect to a stenosis (figure 1.4). This could also explain how immobility is a risk factor for DVT with prolonged stenosis of a major vein blood may flow similarly to that seen in the murine model making it a good starting point.

1.3 *In Vitro* Approach

1.3.1 Microfluidics

Microfluidics is a field which has been developing rapidly over the last 20 years [60, 61]. Generally it is a small channel on a micro-scale which exhibits unique fluid properties. Microfluidic fabrication methods hit a major breakthrough when Whitesides et al developed poly(dimethylsiloxane) (PDMS)device fabrication; increasing speed and ease of making microfluidic chips [62]. It is possible to design complex geometries using computer aided design (CAD) and fabricate using photo-lithography achieving a feature size of 1 μm depending on the resolution of the photo-mask. Photo-lithography is a well established microfabrication technique using UV curable photo-resists. Using a mask aligner uniform UV light is projected through a mask curing the resist in the desired geometries (see methods section 2.2.1). There are different photo-resists depending on the lithography technique being used; they can be classified into two categories: positive and negative resist (see figure 1.5). Negative moulds have the channel left behind whereas positive moulds have the inverse of the channel design. In this thesis, a negative photo resist was used to fabricate PDMS devices by

soft lithography. Mask quality can be chosen depending on feature size, for ten to hundreds of microns an acetate mask is suitable whereas for geometries with much smaller feature sizes a higher resolution mask, aka a quartz mask.

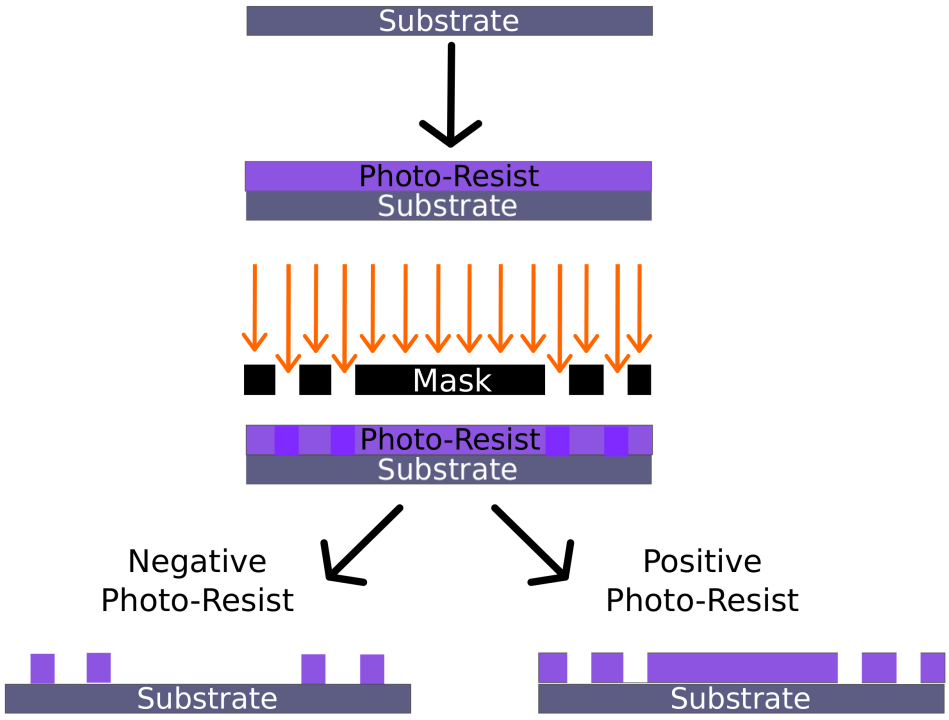

Figure 1.5: A schematic diagram illustrating the difference between positive and negative photoresists used in photo-lithography

Initially the main attraction to microfluidic devices is the high throughput experimentation and that they are economically desirable due to being: cheap fabrication costs and require low volumes of reagents and create very little waste. This is an attractive quality for diagnostic and drug development applications. As mentioned previously, due to the micro scale of the channel, flow will always be laminar according to the equation 1.1 for determining the Reynold's number [63]:

$$Re = \frac{\rho u(\frac{4A}{P})}{\upsilon} \tag{1.1}$$

where, ρ is the density, u is the velocity, A is the cross sectional area, P is the wetted perimeter and υ is the viscosity of the fluid. If the $Re < 2000$ the flow is considered laminar and due to the size of the microfluidic devices, the Re number will never exceed this threshold [**?**]. Re number takes into consideration parameters that influence flow, allowing for the comparison of different fluid properties and relative velocities. This will be useful when comparing a simple fluid with larger scaled vessels, denser fluid, reduced viscosity and velocity, characteristics apparent in different animal models and *in vitro* conditions. Further development of microfluidic technologies have allowed the field to advance into drug development with the ability to carry out single cell analysis [64] and advance into organ on a chip *in vitro* models [65], thus aiming to reduce the need for extensive *in vivo* animal research. There have been some highly complex biological models, with the integration of cells. These are either 2D cultures or co-cultures, however they have advanced into tissue arrays with co-cultures of cells and the extra cellular matrix [66]. A few of examples of these are: cardiac muscle on a chip [67], lungs on a chip [68] and spleen on a chip [69]. It is evident the physical conditions in which the cells are cultured within the chip influence cell phenotype and extracellular matrix constituents [70, 71, 68]. It should be noted that this level of complexity has not yet reached vein on a chip investigations due to the intricacy and difficulty of integrating valves and pumps to microfluidic channels to mimic the physiology of the venous system. Within microfluidics it has been recognised that the dynamic environment aids with the cultivation of cells which better represent *in vivo* cell biomarkers. This is a very attractive concept

as a living organism is dynamic, with chemical and physical changes constantly occurring and differing from person to person. For this reason microfluidic devices provide a micro environment with scope to control many of the physical parameters to manipulate cells.

Microfluidic devices are becoming more popular in blood flow studies, whether it be looking at rheology [72], platelet activation [73], white blood cell activation, red blood cell aggregation as well as chemical responses in drug discovery and delivery studies [74]. The micro-environments make it easier to visualise cellular responses. There is also an abundance of research into arterial thrombosis, *in vitro*. Microfluidic devices have helped determine biochemical processes behind arterial thrombus formation as well as biophysical parameters. Investigation into physical parameters include differing the shear rate to study platelet activation and accumulation [75, 76, 73]. It has also been possible to use microfluidic devices to look at protein expression in response to shear rate resulting in the platelet activation [77] and adhesion [78]. All studies show that high shear rates increases the number of platelets sticking to the channel walls [78, 72, 75, 79]. The shear can be increased by altering the velocity or viscosity of the fluid through the channel. Generally, when investigating platelet adhesion/aggregation whole blood is not used, and instead platelet rich plasma (PRP) is used [72]. Plasma is a lot less optically challenging to work with as the fluid itself is relatively transparent and the platelets can be fluorescently labelled to enhance the flow detection and allow for the quantification of platelet adhesion and aggregation based on the fluorescent signal.

Currently there has been no investigation using *in vitro* conditions due to the high variability with in physical parameters. The velocity of the blood through veins is variable dependent on multiple environmental conditions such as: position of body, fluid intake [80], health of patient: inflammation, infection and age. This variability can be mimicked using microfluidic devices and will allow for the examination of physical parameters leading to pro-thrombotic conditions. Microfluidic flows can be easily manipulated using pressure controllers and syringe pumps, ensuring full control over the velocity. Having complete control over the velocity is advantageous when mimicking the variable conditions in the veins.

However, *in vitro* microfluidic blood flow will have a considerably lower Re number than a large mammal case (*in vivo*). This is because according to 1.1 Re number is determined by the size of the vessel and in a microfluidic case this is in the scale microns whereas blood vessels of large mammals (e.g. humans) is ≈11 cm [81]. To over come this limitation, finite element modelling can be implemented to exceed the boundaries of the experimental set up (discussed later in section 1.4).

The idea of a bypass and thrombosis appears to be only touched upon in literature [56]. Maddala et al use a basic ladder microfluidic device. Within this study they use finite element modelling (discussed later in section 1.4) to help understand the blood flow which is causing the thrombus formation. Using finite element modelling, FEM in this way overcomes the issues of visualising blood flow within the microfluidic channels. It was found that geometrical factors influence thrombus formation [56]. They state that their model shows stagnant regions and points of high shear, however the geometry itself is a ladder which is not representative of an *in vitro* network of blood vessels. It was found that the platelets occur at the regions of high shear, on the corners of the ladder network. Within this thesis, complex microfluidic devices are designed with flexible valves as well as static systems which have a side branch rather than a ladder network. Even though valves have not been reported in the IVC of a mouse they are present within the venous network [57], however thrombosis does not occur. Assuming that this is due to longitudinal flow of blood along the mouse body back to the heart, then surrounding veins may also be valveless, this would allow for a bypass to happen.

1.3.2 Evaluation of Flow

There are multiple ways to track flow through a microfluidic device, the most common being particle tracking velocimetry, PTV, particle image velocimetry (PIV) and micro-particle image velocimetry, μPIV, [82, 83]. Unfortunately PTV requires particles to be optically resolved as it relies on the tracking of individual particles; this is therefore not useful for analysis of flow through microfluidic devices [84]. Generally, fewer particles is beneficial for PTV. PIV,

however tracks velocity fields using pulsed lasers then recorded using charge coupled device, CCD [85, 86] and complimentary metal oxide semiconductor, CMOS [87] cameras. Both cameras have a series of random errors, of which CMOS performed slightly better on single particle image in an interrogation window containing 10 particle images in PIV [88]. In PIV a displacement vector for a window within the region of interest generally consists of multiple particles in comparison to PTV which uses a lower concentration of particles. In order to determine the displacement vector in PIV the signal is processed using a cross-correlation algorithm, converting the signal into a velocity using the time between the pulsed laser and the pixel size and taking an average [89, 90, 91]. A main limitation of PIV is the inability to track flow within the z-plane making it difficult to determine velocity profiles for turbulent flow [89, 92].

The advancement from PIV into μPIV overcomes the major limitation of having to have each individual fluorescent tracer in plane making it a popular choice for microfluidic flow visualisation [83, 84]. For μPIV it is important that particles are small enough to follow the flow field religiously, therefore fluorescent 300 nm particles are a good choice [83]. When using such small particles it is key to consider the effects of Brownian motion, to account for this error depending on the diffusion coefficient (equation 1.2) [93].

$$D = \frac{KT}{6\pi\eta R} \tag{1.2}$$

Where K is the Boltzmann constant, T is the temperature and η is the viscosity of the liquid. The mean square distance of diffusion, $\langle s^2 \rangle$ is calculated as [83]:

$$\langle s^2 \rangle = 2D\Delta t \tag{1.3}$$

where the time intervals Δt are much greater than Brownian motion meaning that the relative error can be determined by the following equation [83]:

$$\epsilon_B = \frac{\langle s^2 \rangle^{1/2}}{\Delta x} = \frac{1}{u}\sqrt{\frac{2D}{\Delta t}} \tag{1.4}$$

where u is the velocity and x is the pixel position. Equation 1.4 indicates the lower limit of Δt and large velocity gradients will have much more complicated errors to consider with regards to Brownian motion [83]. All these imaging techniques use cross-correlation algorithms to track the particles from frame-to-frame [94]. In order to have a successful cross-correlation algorithm the following parameters need to be considered: a statistical measure of the most probable particle displacement, a mean of particle displacements is taken, giving a vector [95]. Generally, when tracking blood flow *in vivo* or *in vitro* PTV or μPIV [96] are used. In general it would seem that microfluidic technologies are favoured for investigating blood flow in complex geometries.

Ghost Particle Velocimetry

Ghost particle velocimetry, GPV, is a relatively new technique for analysing flow [84]. Unlike the typical techniques PIV and μPIV, GPV does not require a complicated experimental set up and expensive lasers. Instead GPV only requires a bright field microscope and a high speed (CMOS), camera to capture a 'speckle pattern' obtained from particles smaller than the diffraction limit (<300 nm). The physics behind the acquisition of the speckle pattern is similar to that of dynamic light scattering, DLS [97]. DLS is a well established technique that utilises the Brownian motion and the time correlation of the scattered light intensity to determine the size of particles [84]. When coherent light hits a particle it is scattered in all directions causing constructive and destructive interferences with the light scattered by the surrounding particles resulting in intensity fluctuations which can be visualised as a speckle pattern [98]. Depending on the time it takes for the displacement of the particle due to Brownian motion will enable the quantification of the size of spherical particles in suspension. The mobility of particles undergoing Brownian motion can also be described as the diffusion coefficient, D, which is affected by the radius of the particle, R through the Stokes-Einstein equation 1.2 [93].

It is not possible to precisely know how each particle moves in solution from the scattered light. However, the movement of particles is relative to each other therefore a mathematical

function called autocorrelation is used to indicate how similar scattered light, I_s at time, t, is to itself after a time interval, t' which can be defined as:

$$C_{(t')} \equiv \langle I_s(t) \times I_s(t+t') \rangle = \lim_{T \to \infty} \frac{1}{2T} \int_{-T}^{T} I_s(t) I_s(t+t') dt \tag{1.5}$$

DLS has $C(t' \to \infty)$ as the baseline autocorrelation function which is dependent on the detector area, optical alignment and scattering properties [98]. Assuming it is a mono-dispersed suspension of spherical particles the autocorrelation of scattered light signal is represented by an exponential decay curve [98, 93]:

$$C_{(t')} = [C(t'=0) - C(t' \to \infty)] exp\left(-\frac{t'}{\tau}\right) + C(t' \to \infty) \tag{1.6}$$

where τ is the characteristic time constant of the above decay function. τ is also related to the diffusion coefficient, D:

$$\tau = (2Dk_s)^{-1} \tag{1.7}$$

where k_s is the scattering wave vector which (for completeness) can be defined by the following:

$$k_s = n \cdot \frac{4\pi}{\lambda} sin\frac{\theta}{2} \tag{1.8}$$

where n is the refractive index of the liquid, λ is the wavelength of the light in a vacuum and θ is the scattering angle [98]. The relationship between equations 1.2 to 1.7 is used in and scattered light [98]. DLS combined with microscopy has been used to study the properties of blood cells [99]. One limitation of DLS is that it requires an advanced optical set up with lasers.

It is now possible to determine particle size and viscosity of a fluid using a standard bright field microscope by a technique called differential dynamic microscopy, DDM [3]. DDM enables the quantification of sub-resolution nanoparticles using simple bright field microscopy [3]. Brightfield microscopy generally use halogen or more recently LED light sources to illuminate the sample with white light, in-coherent light. However, Cerbino et al

overcame this issue by developing a method by simply quantifying the speckle pattern from the scattered light without the need of any expensive lasers or filters [3]. Firstly, the light is focused into a Köhler illumination. Köhler illumination is required to ensure a uniform distribution of light over the region of interest (ROI), which is important to obtain high quality images. Secondly, the numerical aperture of the condenser lens, NA_c is closed to 0.2-0.3 manipulating the in-coherent LED light into a 'partially coherent' light path. This manipulation of light was determined by Cerbino et al for DDM [3]. The more closed the NA_c the better the speckle pattern.

However, with regards this becomes a disadvantage to GPV as the speckle pattern will be acquired over multiple focal planes according to the equation:

$$\delta_z \approx \lambda/(NA_c)^2 \tag{1.9}$$

where δ_z is the longitudinal speckle characteristic size μm and λ is the wave length of light (nm). It is desirable within GPV to have uniform motion at velocity, v over one focal plane enabling the possibility to develop 3D flow profiles throughout a microfluidic device [84]. This is the reason the NA_c is opened to 0.15 to produce a depth of correlation of $\delta_z \approx 20\mu m$ [84].

In order to track the speckles over time multiple images need to be taken at the same frame rate. For DDM, 1000 images were acquired at time intervals 10 and 200 ms(1.6). By taking the average of 1000 frames gives the static contribution (figure 1.6 a) which can then be subtracted from each frame enhancing the speckle pattern seen in figure 1.6 b and c. This step also eliminates any static contribution, 'dirt' observed in the original sample as seen from figure 1.6 a, as black dots. This process is discussed in more detail in the Methods section (2.2.3).

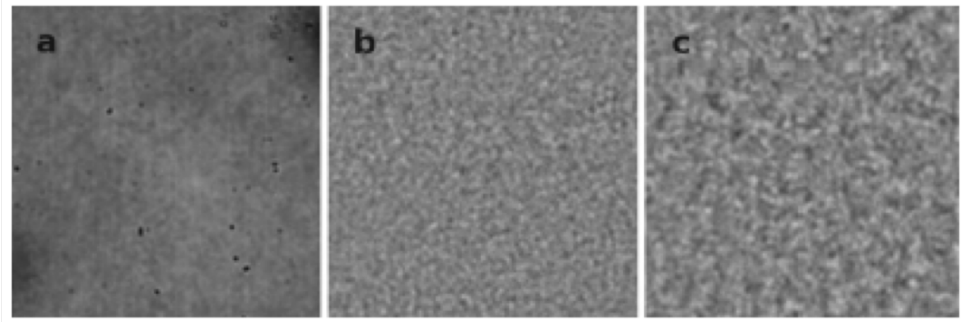

Figure 1.6: An example of the imaging process carried out for DDM. Starting with a) the static contribution, b) speckle enhancement image when the static contribution is subtracted from one of the 1000 frames at 10 ms and finally c) for frames which are 200 ms apart [3]

GPV tracks flow within microfluidic channels meaning that the speckle pattern undergoes a spatial translation $v\Delta t$, meaning that as long as the velocity is greater than the influence of Brownian motion, it can be neglected as the time correlation function becomes a product of the displacement vector $\Delta\mathbf{x}$ along the flow direction[84]. This then produces a peak at $\Delta x = v\Delta t$ which can be cross-correlated from frame to frame in the same way PIV and μPIV works in equation 1.5. Thus, highlighting the lower limit of GPV as a velocimetry technique.

Capturing the speckle pattern is also dependent on frames per second, fps of the camera, which is also its biggest limitation [100]. Riccomi et al concluded that GPV is limited by camera performance and carried out numerous validations of the consistency of the cross correlative velocity magnitude over 500 frames as well as comparing results with μPIV [100]. It was subsequently found that GPV is an excellent reliable technique for measuring flow with relatively low velocities [100]. However, these experiments were also carried out within a larger device (channel depths of 1 and 2 mm) meaning the signal to noise ratio will also be greater as the interference from different planes will also affect the results. For this reason, it is the detection technique of choice for the following experiments as not only are the experiments within range of the *Re* number, the majority of the channels used are no deeper than 150 μm. This means there is a significantly higher signal to noise ratio and field of view

is less of an issue because the devices are notably smaller.

Another advantage of GPV over other particle velocimetry techniques is that the particles are small enough that they do not interfere with the fluid properties. This is advantageous for wanting to detect complex flow patterns with in small devices [101, 102]. It has proven a very useful technique for detecting vortexes in droplets and for investigating the efficiency of mixing in microfluidic droplet formation [101], therefore making GPV an appropriate technique for investigating fluid flow around micro-structures both solid [103] and flexible (proved within this thesis).

1.4 Computational Fluid Dynamics

As technology is advancing the ability to match the dynamic complexity of living systems is becoming more feasible making computational fluid dynamics, CFD a more attractive tool in biomedical research. Simulations that used to take days to compute are now only taking hours, and sometimes even minutes (depending on the complexity of the model). CFD is used throughout engineering to aid the design of industrial plants, improving the efficiency of production and maintenance. The cardiovascular system is a complex network of pumps, valves and pipes, as discussed earlier, however the complexity arises from the varying material properties, the constituents of blood, position in the body and surrounding tissues (to name a few). Essentially there is large variability from person-to-person, however using CFD enables a multitude of parameters to be investigated in order to determine a pathological outcome. CFD models can be split into two methods, meshed and mesh free simulations.

1.4.1 Mesh Simulations

Finite element methods (FEM) are very popular when trying to understand fluid flow [104]. The mesh is an important aspect when carrying out FEM simulations. It subdivides the total volume in to smaller volumes called elements. Elements can be 1D, 2D or 3D, this thesis uses gmsh for mesh development, which uses a 2D triangular and 3D tetrahedral meshing

geometry. This has been used widely in previous FEM simulations of blood flow [105, 106, 107]. It has been noted that tetrahedral geometries are common for modelling fluids [106, 108, 107]. The nodes are the vertices of the shape (highlighted in figure 1.7).

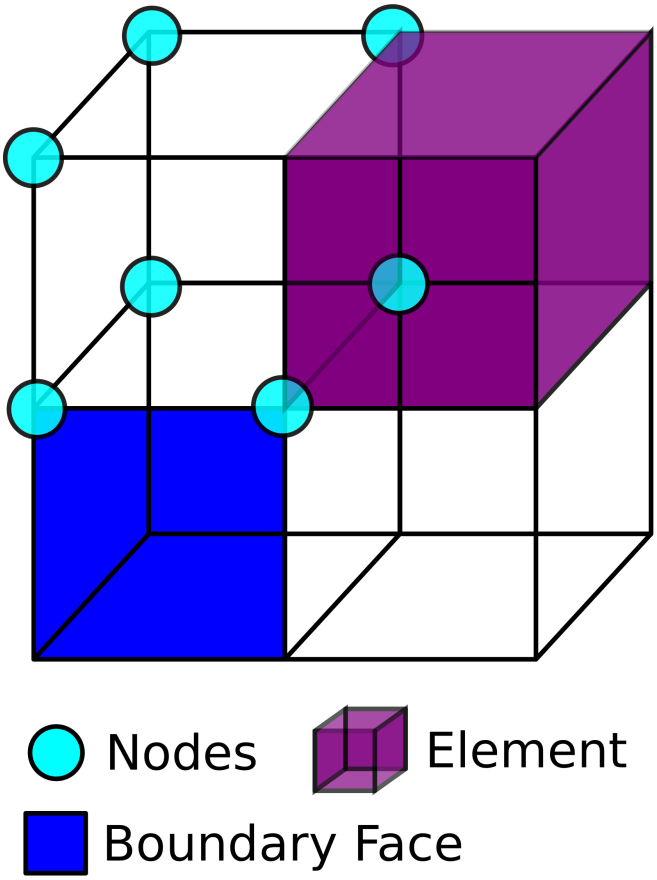

Figure 1.7: A visual representation of elements, nodes and boundaries typically used in FEM simulations

The optimisation of a mesh is highly important when running FEM simulations. It can be optimised with localised refinement across the geometry. When using FEM for modelling biological valves there are two main things to consider: 1) solid structure and its material properties, 2) the surrounding fluid and its viscosity and density bring rise to a highly complex fluid structure interaction problem. In order to simulate blood flow in a vein there are two main algorithms to consider: conforming mesh (figure 1.8a) methods and non conforming mesh methods (figure 1.8b).

- **Conforming mesh methods** divide the mesh into two parts: one for the solid valve where the deformation equations are solved and the other for the fluid where the Navier-Stokes equations are solved. This means that the mesh will move with the boundary [109].

- **Non-conforming mesh methods** is an Immersed Boundary Method where the mesh does not move with the boundary and the movement of the interface between the solid and liquid is accounted for using forcing terms to the governing equations of the fluid motion [109].

A major disadvantage to a conforming mesh is that it can become computationally expensive due to the constant need for re-meshing at the solid-fluid interface. This being said, as the majority of simulations within this thesis are 2D, it is possible to use the conforming mesh approach.

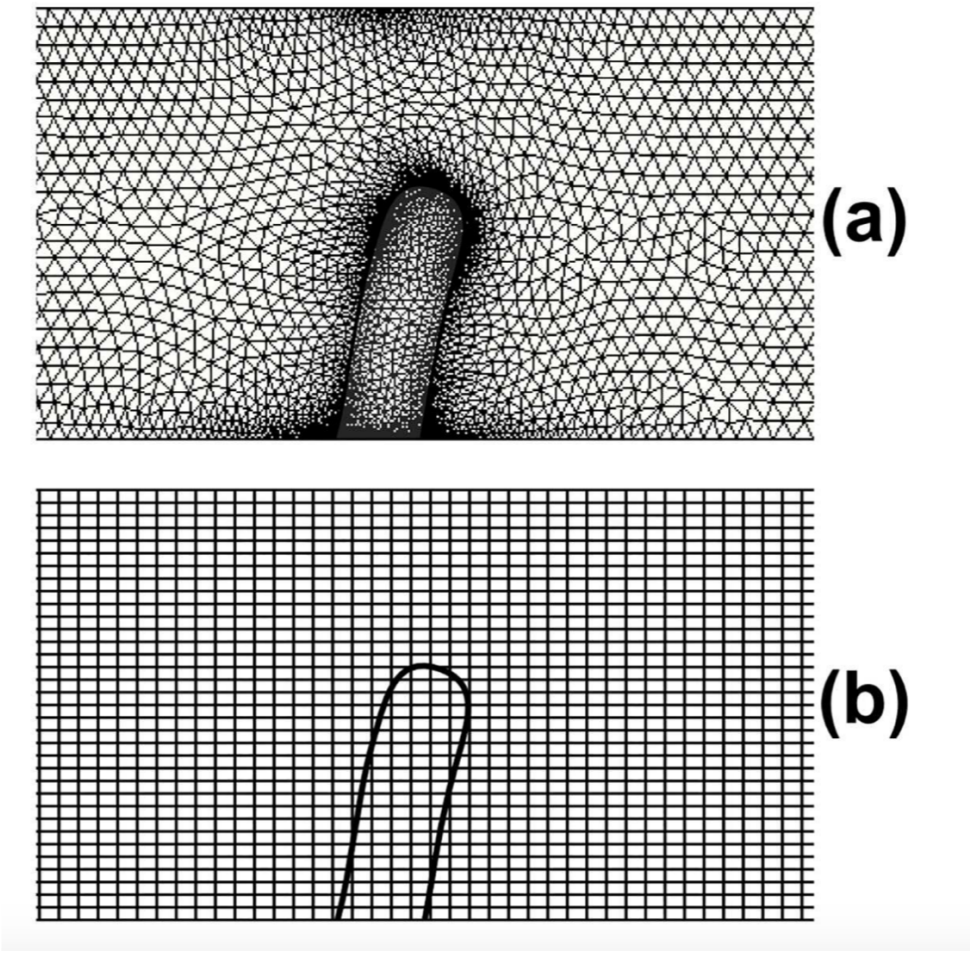

Figure 1.8: A mesh representation showing the differences between a conforming mesh approach (a) and a non-conforming mesh approach (b). Figure taken from Ariane et al 2017 [4]

Both conforming and non-conforming simulations have been used for modelling the cardiovascular system. It would seem that the most advanced models are for the heart [110, 109] and arteries and similarly to *in vitro* research there is a distinct lack of research into the venous system. There are some rather elegant finite element simulations for understanding blood flow around and out of the heart. This has been useful to determine how stiffness of valves and vessel play an important role at pumping blood around the heart and through the aorta to the rest of the body [110, 111]. This has lead to an extensive understanding to many cardiac diseases, including for the investigation of the efficiency of artificial valves [109, 112]. It is now possible to use magnetic resonance image, MRI to obtain specific ge-

ometries of the heart for CFD modelling, aiding in the preparation of surgical procedures [113]. The progression in technology and understanding of *in silco* research is a powerful tool for the optimisation of surgical procedures and determination of suitable implantation materials from person-to-person.

Thrombus formation within arteries is becoming increasing more popular within modelling and simulation as CFD technologies are advancing [114]. Papadopoulos et al has developed a model of thrombus formation and growth simultaneously within veins alongside blood flow, and concentrations of various substances [115]. This model assumes that thrombin generation occurs on vessel walls and the platelet surface, however does not account moveable boundaries, such as venous valves. As the vessel is more complicated a more advanced modelling system is required to account for all the factors within veins, such as: flexible valves, muscle pump, slow flow rate, various sized blood cells, activation of platelets, etc.

1.4.2 Mesh Free Simulations

Mesh free simulations are relatively new to CFD bringing many advantages of the conventional finite element simulations. Instead of using elements and nodes this technique utilises a 'particle based' approach. Discrete multi-hybrid system, DMHS is a novel "model-by-models" simulation technique to link multiple parameters to achieve a complete representation of complex systems – like veins and blood flow [116]. This model-by-models approach overcomes many limitations with current numerical models as it is mesh free. DMHS allows for the simulation of solid-liquid suspensions-like blood as well as adding movable boundaries for the flexible valve flaps. There is high demand for these systems to further understand flow around the heart, and perfect surgical techniques. DMHS also allows for certain particles to become 'sticky' with in the model, which can simulate the thrombus forming [4]. Ariane et al has carried out multiple DMHS simulations looking at both valve length and stiffness and its effect on thrombus formation [4, 117]. They found that leaflet stiffness and length play a crucial role in the initiation of thrombus formation.

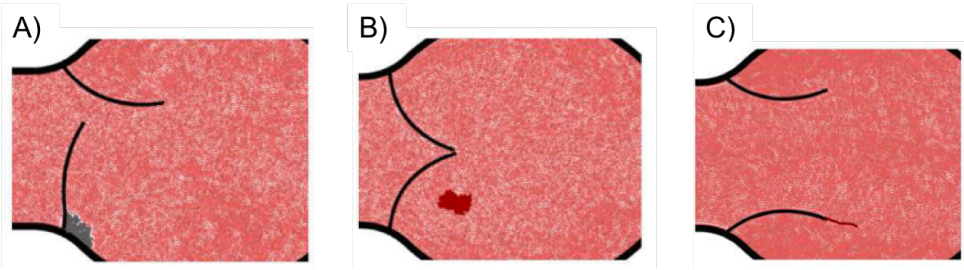

Figure 1.9: A figure showing different algorithms used to investigate clot formation. A) Uses a 'calcification' approach, B) is a free clot and C) is a 'filiform clot' Figure taken from [4]

Unfortunately mesh-free methods are relatively new meaning there is less available information, expertise and software. However it is a highly attractive tool for the modelling of biological processes, especially at fluid structure interfaces as it overcomes the major limitations in mesh based simulations [116]. Due to the lack of information and software available for mesh free simulations and the nature of this thesis (experimental and computational) the focus will be on mesh based simulations to validate and extend from the experimental findings.

It is safe to say that computational multi-physic simulations are leading the way in understanding flow around valves in venous flow conditions. They have been carried out using various finite element and mesh free approaches. An advantage to using simulations is the ease at altering minor changes to physical parameters or boundaries (e.g. geometries, elasticity, friction, etc). The major drawback behind simulations is that they generally use ideal situations to collect high quality data, this is not true to life therefore experimental validations are always desirable. Within this thesis it is used to validate the experimental results as well as extend the limitations of the experimental procedure to explore further into the *in vivo* case.

CHAPTER 2

MATERIALS AND METHODS

2.1 Geometry

2.1.1 Stenosis Model

All geometries were designed using AutoCAD (Autodesk Inc, US). Starting with the murine model, microfluidic channels were designed with the following parameters: width 200-500 μm and a stenosis of 50-80% of the channels. Geometries with side branches and anomalies (closed side branch) where also designed. The width of the channel was to match that of the IVC of a mouse as much as possible (D $\approx 200\mu m$). The reason for varying the degree of stenosis was to determine whether or not it influences flow patterns which would be indicative of thrombus formation, as reported in literature, the larger the stenosis the more likely a thrombus is going to form. And finally the addition of side branches was to explore the disruption of flow before the stenosis which is suggested to cause/prevent thrombus formation depending on the position of the side branch. By observing many possibilities it will be interesting to see if there is any disruption to flow and whether or not this could be linked to thrombosis. It will give an insight to development of thrombus formation with in a murine model.

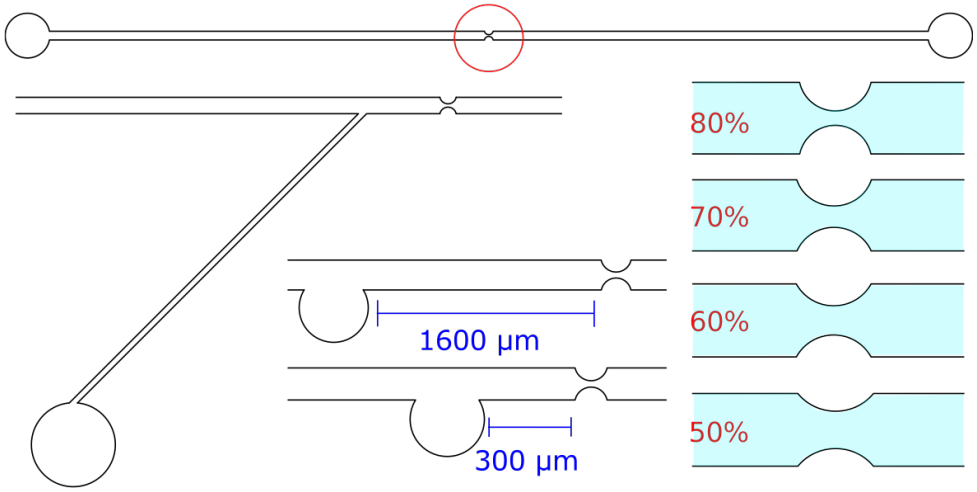

Figure 2.1: A diagram illustrating the different stenosis, closed side branch geometries and side branch geometries at the different positions.

Cylindrical Stenosis Device

Obviously, veins are not square so after the microfluidic devices were designed, 3D cylindrical geometries were also designed to look at the effects of the curvature on flow. It should also be noted that it is the aim to progress the model into a more 'human-like' device and for this reason 3D printing methods are going to be used. The geometries were designed using AutoCAD, as before, and saved as an .stl file (see figure 2.2). Illustrated in figure 2.2 is the dimensions of two half cylinders. This was to make the fabrication steps in 2.2.1 slightly easier.

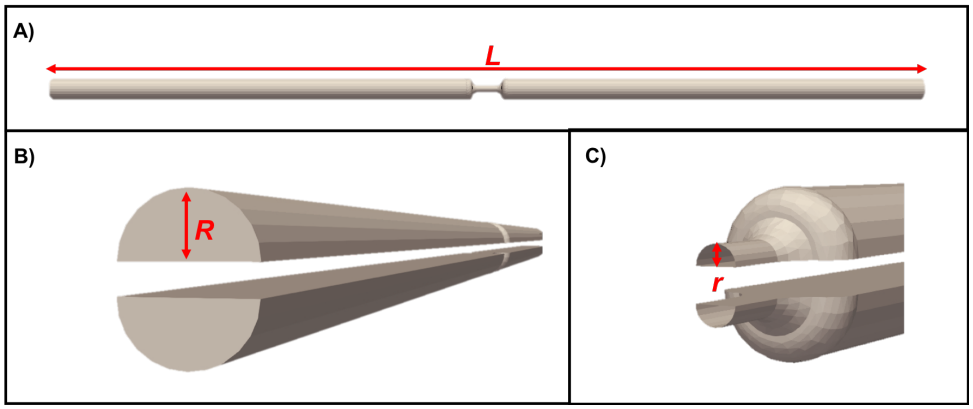

Figure 2.2: A 3D CAD drawing of the cylindrical device at different angles A) is the top view and B) illustrates the end of the channel where R = 0.5 mm and C) the stenosed region r = 0.15 mm

2.1.2 Bypass Model

To develop the device specifically for the bypass model, a bypass around the stenosis was added at 3 different positions along the channel (see figure 2.3 and 2.4).

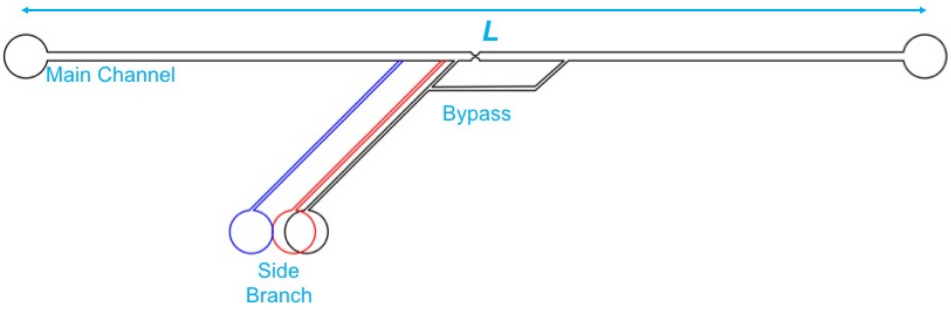

Figure 2.3: An example of a CAD drawing of the bypass geometry with the three different positions of the 100 μm side branch, black = 300 μm, red = 600 μm and green = 1600 μm away from the stenosis. Regions are labelled and L = 2.12 cm

Figure 2.3 is an example of the geometry used in the bypass experiments, however position was not the only parameter studied. The influence of side branch width (W_{SB}) was also investigated, in order to do this a $W_{SB} = 200\mu m$ and $W_{SB} = 100\mu m$ was designed. The example displayed above in figure 2.3 is the $W_{SB} = 100\mu m$. Finally the degree of stenosis was

also explored. In order to have control over the amount of stenosis over smaller increments than in the stenosis model, a valve was added to restrict the main channel like seen in figure 2.4. Three pump geometries were tried.

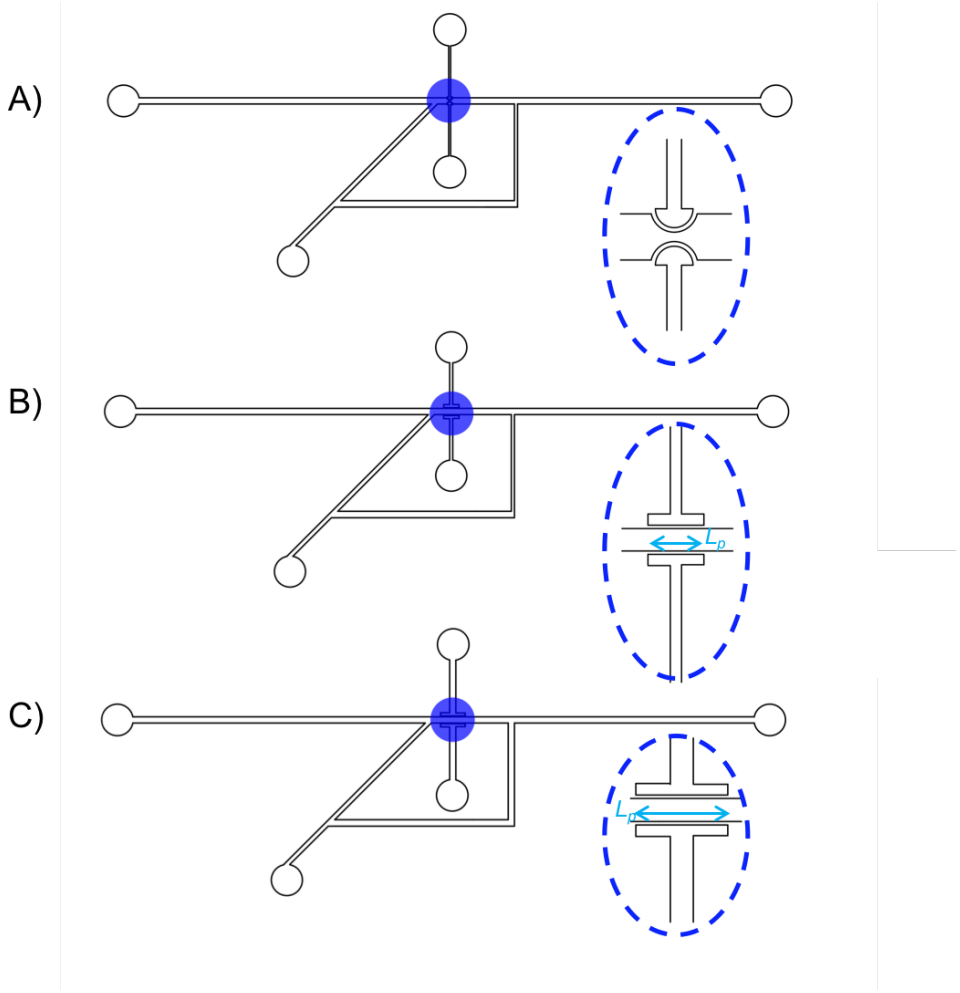

Figure 2.4: The CAD image of the pump devices, the A) showing a curved design, B) the short based pump (L_p= 500 μm) and the C) a long based pump (L_p= 800 μm) geometry

The three geometries were designed in order to determine the most efficient way to apply a stenosis to the main channel. The curved base (top geometry figure 2.4 A), was designed in the case that the PDMS was too stiff and did not close the main channel sufficiently to cause a pressure drop. The long and short and long valves were designed as according to literature geometrical designs [4].

2.1.3 Valve Model

Microfluidic Device

The straight channel where width, $w = 300\mu m$ had to be adapted to secure flexible valves in place. The initial design used pillars to secure the valves and the second used an anchor (fig 2.5). The reason for the anchor is that the polyethylene glycol-*di*acrylate, PEGDA does not cure in the presence of oxygen and as PDMS is permeable to oxygen there would be a small gap between the PEGDA valve and the PDMS channel walls.

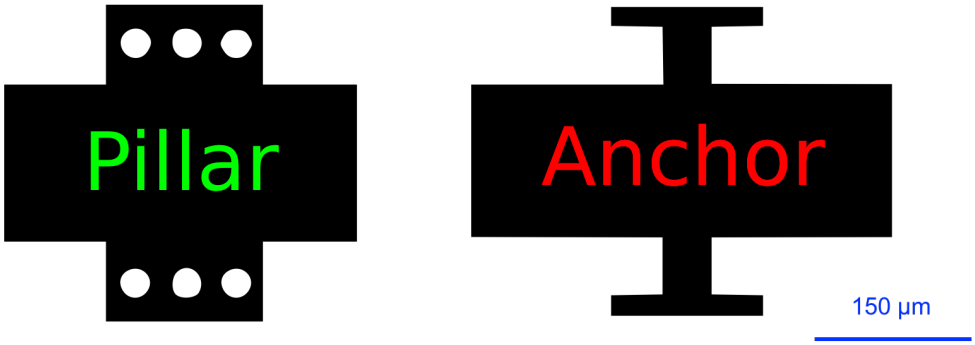

Figure 2.5: The CAD image of the geometries that were tested to secure the valves in place

The valves themselves were designed according to different scaling factors depending on the magnification (see table 2.1).

Table 2.1: A table to present the scaling factors for designing the masks depending on objective used

Magnification	Scaling factor (μm/Px)
x4	2.63
x10	6.71
x20	13.78

There were two valves used throughout this thesis: a simple valve and a leaflet valve (see figure 2.6)

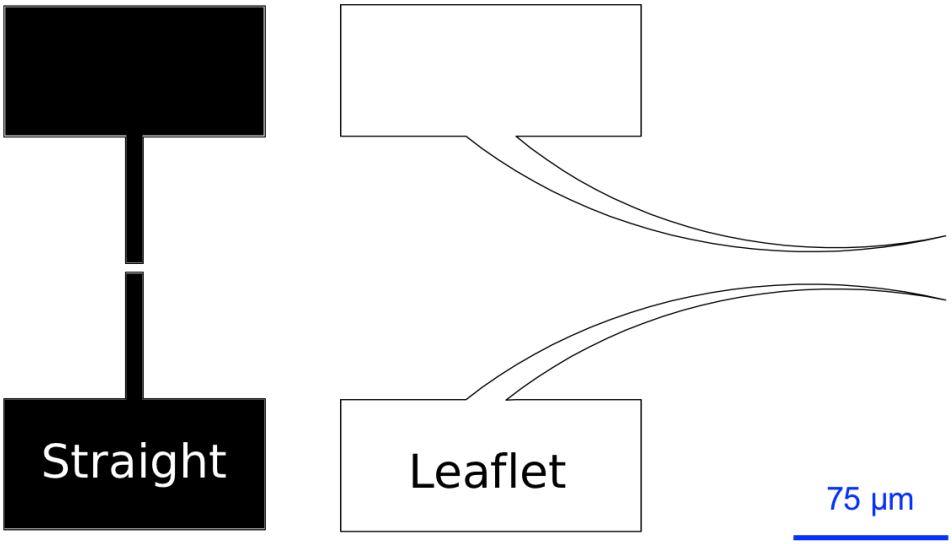

Figure 2.6: The CAD images of the valve geometries used for *in situ* material characterisation (straight valve) and flow studies (leaflet valve)

3D Printed Device

There were two 3D printed geometries, the first one aimed to print the whole geometry with valves cut out with dimensions 4x4 mm. However this geometry was fabricated unsuccessfully and the depth was too great to visualise flow patterns. This was overcome by designing two separate geometries for 3D printing. The first being a straight channel 2x4 mm with length 12 cm and the valves printed independently of each other with slightly deeper 0.5x3 mm as seen in figure 2.7.

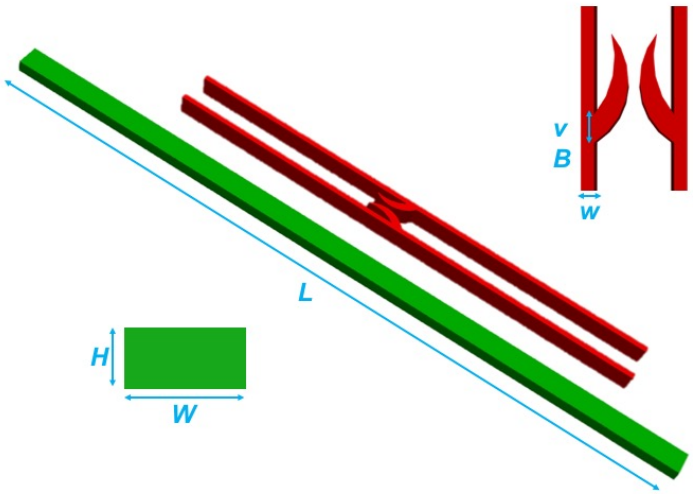

Figure 2.7: The 3D CAD drawing of the static valve structures which were printed on the 3D printer. $L = 12$ mm, $H = 2$ mm, $W = 4$ mm, w= 0.5 mm $vB = 1$ mm

The use of the microfluidic valve geometry for 3D printing is not possible due to the valves being too thin to print. Therefore thicker valves were designed to suit the resolution of the 3D printer ($\approx 25\mu m$)

2.1.4 Simulation Geometries

Geometries designed for the stenosis (microfluidic and 3D printed) model and valve model were also used in the simulations. It was considered so to better replicate experimental conditions extruded geometries were used at roughly the depth $\approx 100\mu$m. However, due to laminar nature of flow it was more time effective to run the majority of microfluidic simulations in 2D geometries(results discussed later in section 5.5) especially when valves were added. The valves used in the simulations were the geometries used to create the UV-masks. In addition to the masks the valves were also rounded at the tip, to better replicate the experimental conditions with the aim to duplicate results achieved in the microfluidic devices. The geometries were imported in to the meshing software as an .igs file allowing the allocation of points along the lines and add points for localised mesh refinement (figure 2.8 A1 and A2).

The results of the addition of the points will be seen later in the section 2.3. The geometry of the valves were slightly adapted to better replicate the experimental conditions. Instead of using the sharp point in the mask, the tip was rounded slightly with the aim to achieve more accurate results to validate the experimental assumptions (figure 2.8 B). Alongside the long valves used in the experimental results a second geometry was designed directly into gmsh. This was to look at the influence of shorter/thicker valves and the influence on flow (figure 2.8 C).

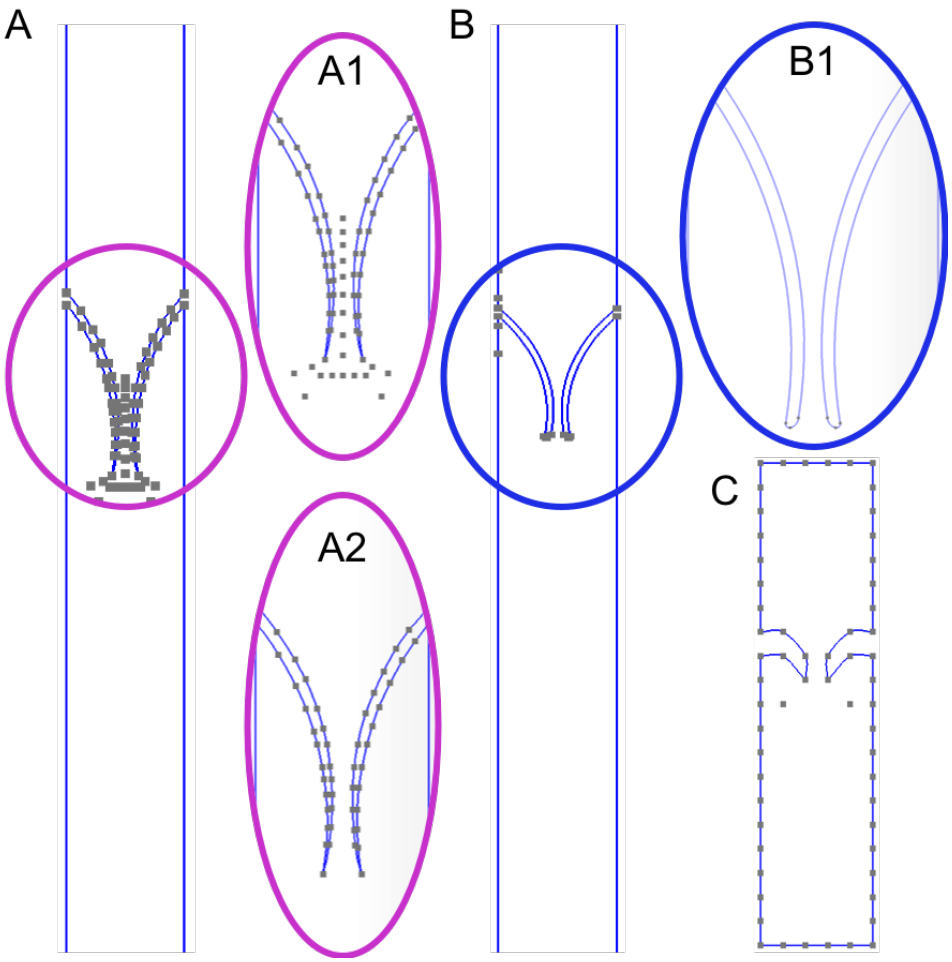

Figure 2.8: A Is the geometry with the valve geometry taken from the mask with A1 and A2 showing the points which have been added for mesh refinement. B is the curved valve and C is the geometry for the short thick valves

Once the geometrical entities are drawn the physical groups need to be defined before

a mesh can be created. These physical groups are the: valves, channel walls, inlet, outlet and the fluid. Each physical group is given a surface in which a mesh can be applied. The groupings then enable the setting of boundary conditions in the section 2.3. Points can also be made physical groups and mesh refinement can be set around them, these points have been added in order to increase the resolution of the calculations around the point where interesting flow patterns could occur.

2.2 Fabrication of the Device

2.2.1 Main Channel

Conventional soft lithography techniques (see figure 2.9) were used to fabricate polydimethylsiloxane (PDMS, Sylgard® 184 Silicon Elastomer Kit, Dow Corning, UK) devices. Firstly, 5 g of SU8-2075 (MicroChem, Westborough, USA) was added onto a silicone wafer (d=100 mm, Si-Mat, Germany) and spin coated at 1750 rpm. Microfluidic devices need to be fabricated using a clean room to reduce the risk of dust contamination, which consequently improves reproducibility of the channel depths as there is strict environmental control, temperature and humidity. Unfortunately the SU8-2075 degrades over time, meaning that even though there was strict environmental control there was slight variance in channel depth over time. Once there an even spread of photo-resist across the silicon wafer is achieved, it is soft baked for 5 mins 65 °C followed immediately after by 35 mins at 95 °C. Then the photo mask (Micro Lithography Services Ltd, UK) is aligned with the silicon wafer using a mask aligner (Canon PLA-501FA Mask Aligner) and exposed to ultra violet, UV, light for $2x40$ seconds. There was a break between each 40 second exposure to prevent cracking of the photoresist. The silicon wafer the underwent further baking (3 mins at 65 °C and 12 mins at 95 °C). Finally the channels can be developed using SU8 developer (MicroChem, Westborough, USA) and washed with isopropan-2-ol (Sigma Aldrich, UK). This creates a master mould, which can be reused for soft lithography microfluidic devices.

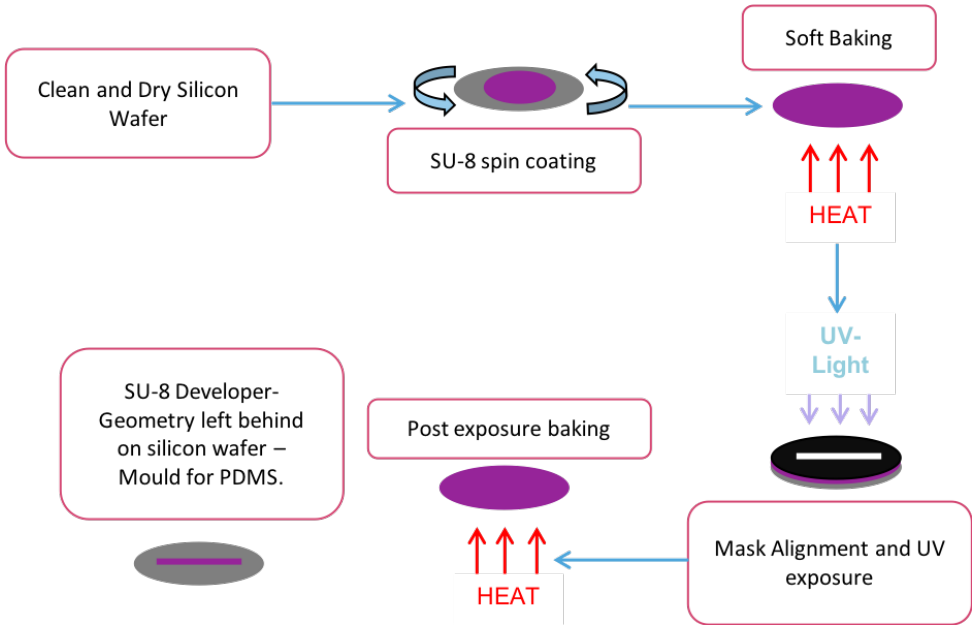

Figure 2.9: A flow diagram of the photolithography process carried out in the clean room

The PDMS and curing agent was mixed together (10:1 ratio) and poured onto the master mould. Degassing of the PDMS was carried out under vacuum. Once all the gas has been removed the coated master mould was baked for 1.5 hrs at 70 °C and left over night at room temperature to be used the following day. However, if the devices were required for use in the same day, the curing in the oven was increased to 3 hrs to ensure full curing of the device. The PDMS channel is then cut and pealed away from the master mould creating the top layer of the microfluidic device. Inlet and outlet holes are punched into the PDMS with a biopsy puncher (1.5 mm, Miltex by Kai) and plasma treated using a corona discharge (PZ2 Handheld Device, Relyon Plasma GmbH, Germany) before being bonded to the bottom layer of the device (glass slide or PDMS). To encourage this binding process the whole device is left on a hot plate at 80°C under a 50 g weight for ≈30 mins. Special care needs to be taken to ensure the curing temperature is constant throughout the fabrication of all devices but in particular the bypass geometries. It is reported that curing temperature affects the elastic properties of the PDMS [118]. The devices are now ready to use.

3D Printed Devices

Stenosis Cylindrical Design

The 3D device moulds were printed using a laser 3D printer (Form 2, Formlabs, England) with a laser spot size of 150μm and a layer height of 25 – 100μm which meant to achieve the best resolution for the stenosed region the geometry was aligned directly on top of the printing plate with the 3D printer scanning along the x, y plane illustrated in figure 2.10.

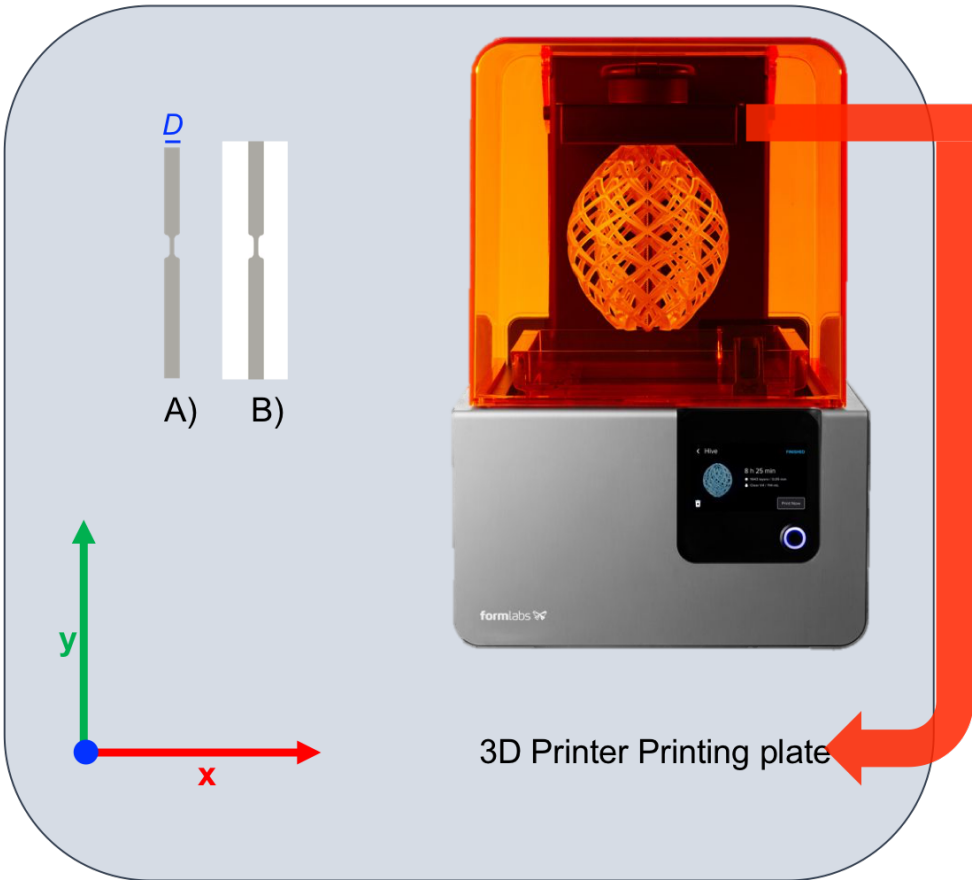

Figure 2.10: A not to scale picture showing the Form 2 3D laser printer used for the fabrication of the cylindrical devices, along with geometry orientation on the printing place A) without a base and B) with a base. The printing direction is a raster along the x, y plane. D = 1 mm

Once printed the mould is then washed using soap and water to remove excess monomers that prevent curing of the PDMS. Then PDMS is poured onto the mould as described in method 2.2.1. Firstly the half cylinder was adhered to a glass slide same as for the microfluidic channels, however the fabrication of a full cylinder is more complex. The mould with the base had the most accurate geometry as when printed directly onto the printing plate there was a slight angle during the printing process affecting the diameter of both the main channel and stenosis. For this reason the channel was printed onto a base which can be seen in figure 2.10 B. The half cylinder was printed twice in order to create the top and the bottom of the device as indicated in figure 2.2 previously. Due to the size of the stenosis region a microscope is required to enable a precise alignment of the top and bottom PDMS devices. Early attempts, although aligned, when left on the hot plate to secure the two channels were not adhering to one and other. Initially it was thought that when carrying out the corona discharge treatment of both sides of the device that the surface functionalisation was not lasting long enough during the alignment process. It is reported in literature that the hydrophobicity induced by the corona discharge treatment only lasts for a limited time [119]. In order to prolong the functionalisation of the PDMS surface from the corona discharge, water was added. Unfortunately, the adhesion did not occur with the addition of water to the surface, it was thought that this was due to the slow evaporation of water from the two channels. Ethanol was then tried and although slightly better the two channels could still be peeled away from each other easily. This lead to the final conclusion that the surface roughness of the base was the parameter preventing the adhesion of the two PDMS cylindrical channels. Therefore within this thesis, only half a cylinder is going to be investigated experimentally to observe the effects of a 3D stenosis on the fluid flow.

Valve Design

The straight channel mould was printed in the same orientation as seen in figure 2.10. There was no need for a base as this was a simple rectangular channel compared to the more complex stenosis geometry. The valves were slightly more intricate; they required support structures and printed at 45° angle. Various positions were tested in order to ensure that the valves

themselves were printed with precision and symmetrical on both sides. The device assembly was also complicated. The valve structures had to be adapted to ensure an exact fit with in the channel. If the valves were not a snug fit there would be excess flow around the valves which is not seen in the microfluidic devices making them incomparable. If the valves were excessively big they would prevent the adhesion of the channel to a glass slide and result in air bubbles occurring in the channel. Although corona treatment was used, it did not secure the channel to the glass slide and for this reason Araldite® Epoxy Adhesive (Araldite Professional Adhesives, Switzerland) was used along with a clamp to prevent bubbles forming within the channel.

In Situ Fabrication of Flexible Valves

Stop-flow lithography was used to fabricate flexible valves *in situ* to the microfluidic channel [120]. The channel was injected with polyethylene glycol-*di*acrylate (PEGDA; $Mw \approx 575$, Sigma Aldrich, UK) and photo-initiator, PI, 2-hydroxy-2-methyl propiophenone (Sigma Aldrich, UK). The PI enabled the polymerisation of PEGDA when exposed to UV light ($\lambda \approx$ 365 nm). To ensure there were no air-bubbles within the device a second syringe was added to the outlet to add a counter pressure, pushing the air out of the channel. The device was then left until the flow had settled (usually about 2 mins). Once the flow has stopped it is possible to align the mask with the channel (fig. 2.11). The mask is positioned at the conjugated plane in the epi-fluorescence light path of the optical microscope (Nikon Ti-U, Japan) and illuminated with an LED source containing a UV band (SOLA-SE-365, Lumencor, USA). To align the mask with the channel and prevent premature curing, a filter was used $\lambda = 545 \pm 25nm$ The filter was then switched to allow the selection of the UV wavelength $\lambda = 350 \pm 50nm$ to cure the PEGDA into the desired geometry. This whole process was carried out using x20 objective. PEGDA does not polymerise in the presence of oxygen [121]. As PDMS is oxygen-permeable, a thin layer of PEGDA (about 3 – 5 μm) remain liquid after UV exposure. This guarantee the possibility to fabricate valves that can move freely but also require a geometry (pillars or anchor) to keep them in place. The lowest ex-

posure time required to achieve the best resolution was adopted, in our case 300 ms. The exposure time is dependent on the concentration of PI and was found to have a linear relationship between concentration and exposure time [122]. In order to create asymmetrical valves each leaflet was fabricate separately. We used a mask for each leaflet and control the characteristic of each one independently by modifying PEGDA or PI concentration or UV exposure time.Finally, after valve fabrication, the channel was flushed with water and the whole device was submerged in water to preserve hydrogel properties until the experiment was performed, and in any case for no more than 24 hours.

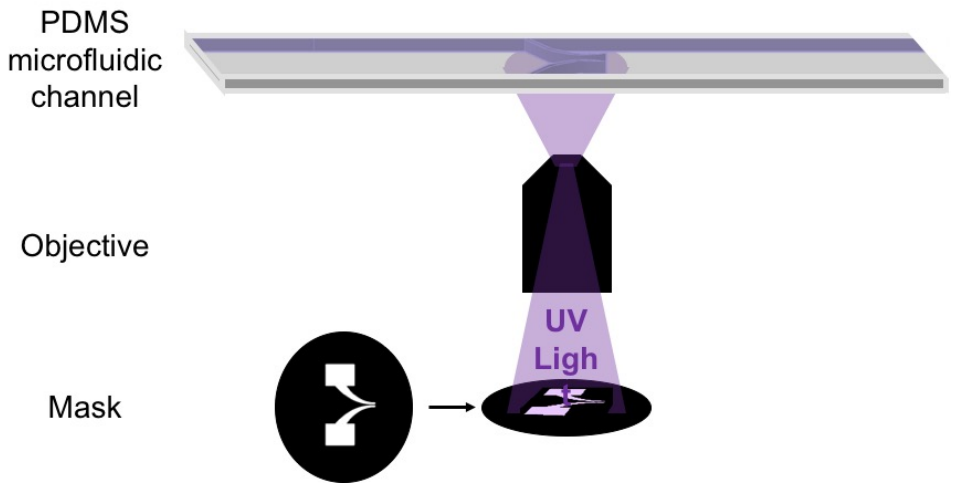

Figure 2.11: A schematic diagram illustrating the method behind the *in situ* fabrication of flexible PEGDA valves

Once valves had been fabricated it was important to characterise them *in situ*. With varying concentrations of both PEGDA and PI it then possible to determine the material properties of the valves. This was carried out similar to that by Wexler et al., [122]. It is possible to calculate the Young's modulus, E, from the deflection as a function of flow rate by the following equation:

$$E = \frac{u_1}{u/Q} * \left[\frac{6\mu(D+d)H^4}{(\frac{1}{12} d\, w^3) D^3} \right] \tag{2.1}$$

Where D is the depth of the channel, μ is the velocity, Q is the mass flow rate (m^3/s), H is channel width, d is the depth of the valve, w is the width of the valve (as seen in figure 2.12), $c = h/H$ and $u_{(c)} = \epsilon c^5(\frac{\pi}{16} - \frac{2}{45}) \approx 0.15\epsilon c^5$ therefore $u_1 = 0.15 * (0.4)^5 \cong 0.0015$ as it is linear contribution that is considered (small deflection). It is the small deflection that we can use to calculate E [122]. The reason for using small deflection is to allow for the measurement of deflection as a function of dimensionless fibre height $c = h/H$ using $u_1(c)$. [122].

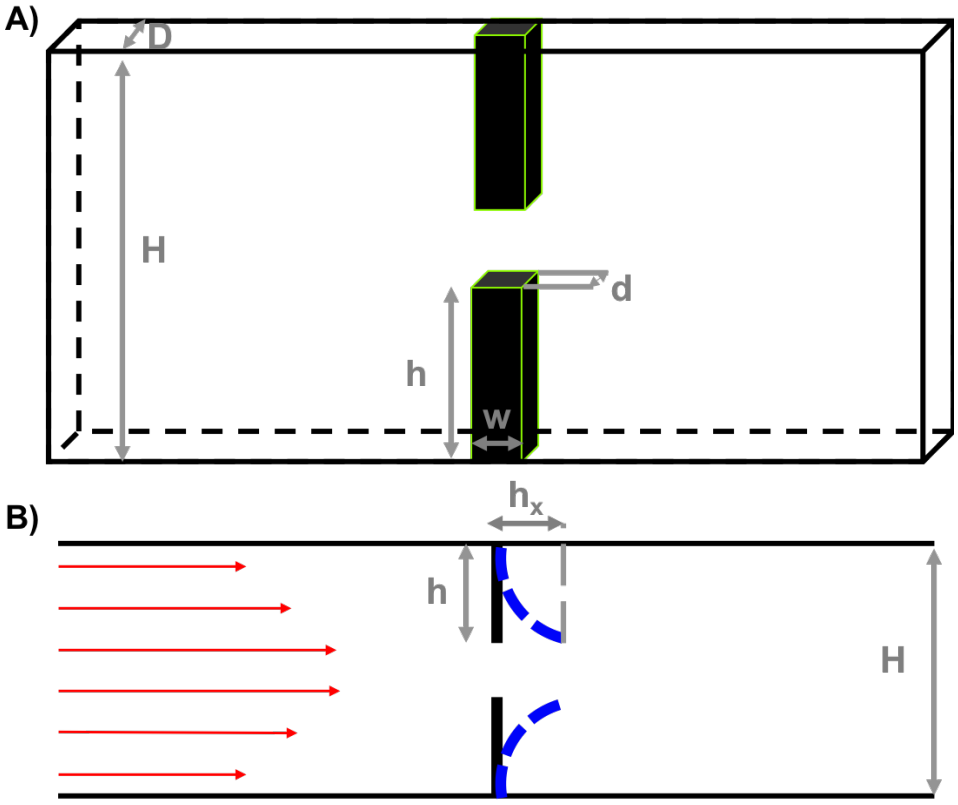

Figure 2.12: A 3D (A) and 2D (B) diagram illustrating the parameters used in equation 2.1.

2.2.2 Experimental Set up

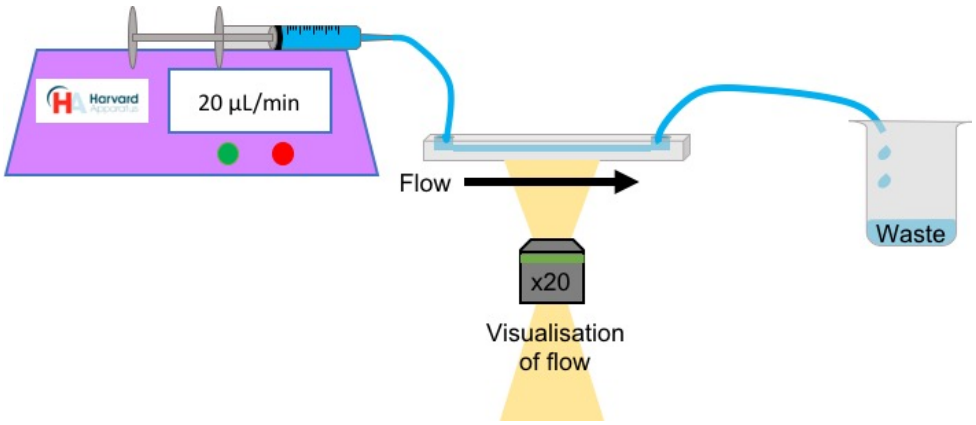

Figure 2.13: A schematic diagram demonstrating the experimental set up including syringe pump to control flow rates, microfluidic device and waste collection. Although fluid here is illustrated with blue, in actual experimental set up appear to be white PS particles due to the scattering of light off the nanoparticles making the solution translucent

Stenosis Model

Each inlet to the microfluidic device was connected to a 5 mL syringe (Becton Dickinson hypodermic syringes, polypropylene, Sigma Aldrich, UK) and tubing. The outlet's tubing was directed to a waste vial (figure 2.13). The syringes were placed into a syringe pump. For the branched devices two syringe pumps were used to control the flow rates independently to each other. Two cameras were used to optimise the experimental set up for the most efficient data collection process. The two cameras were the SA5 and SA3 photron CMOS cameras (Photron Europe Limitted, UK).

Whole Blood Preparation

Blood samples were taken from healthy volunteers approved by the Ethics Committee for research in to DVT. Under Alexander Brill (Institute of Cardiovascular Sciences, University of Birmingham) (ERN 11-0175)

In the branched geometries whole blood (5 mL from healthy volunteers) treated with

ethylenediamine tetra acetic acid, K_2EDTA (10 μL of 20 % (v/v) K_2EDTA solution for 1 mL) to prevent clotting and Dulbecco's phosphate-buffered saline (DPBS) with no calcium or magnesium. This is because the presence of calcium ions encourages clot formation [123]. DPBS and whole blood was pumped through the different inlets of the branched geometries.

Blood Plasma Isolation

Whole blood was collected and prepared as above in section 2.2.2. Then in order to isolate the blood plasma, whole blood was added to polypropylene tubes (10 mL per tube) and centrifuged at 200x g for 20 mins at room temperature. As platelets are smaller than other cells within whole blood they remain at the top after centrifuging. The top layer, which is the platelets and plasma before centrifuging again at 2000x g for a further 10 mins. Platelets will pellet at the bottom of the centrifuge tube allowing for the removal of the blood plasma supernatant. Care was taken not to disturb the pellet. Blood plasma was used the same day of collection and isolation.

Bypass Model

The syringe pumps and microfluidic channel was connected in the same way as in section 2.2.2 for the non-pump design. Flow rates 1-10 μL/min and 5-100 μL/min were investigated in the side branch whilst the main channel remained at 10 μL/min and 100 μL/min respectively. These conditions were then switched to investigate a variety of possibilities. The pump inlets were connected to a pressure controller (OB1 MK3, Elveflow, France) similar to that described above. The pumps were also filled with fluid (ink) to ensure there was no air which could be pushed through the PDMS into the main channel, creating bubbles. Ink was used to enable to visualisation of fluid.

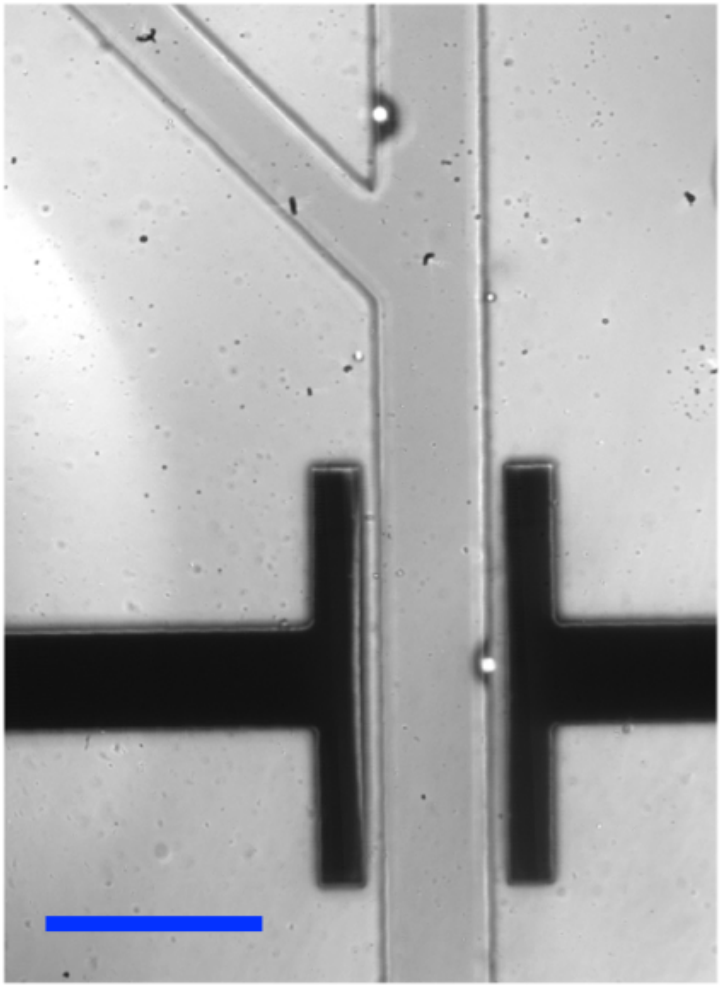

Figure 2.14: A microscope image of demonstrating the pump channels filled with ink. Scale bar = 75 μm

To induce a stenosis within the channel the microfluidic device was connected to the pressure controller the pressure was changed from 0-1900 mBar to constrict the main channel for the pumps and flow rate was controlled by applying 50 and 30 mBar to the main channel and by the side branch. Initially GPV was carried out to visualise the bypass occurring as a result of differing flow rates. However, when investigating the bypass as a product of stenosis, larger particles were used to observe the bypass more prominently (3 μm at 0.1

% w/v).

Valve Model

Two flow conditions were investigated within the valve model: continuous and pulsed flow. First, the continuous flow experimental set up used the syringe pumps which were connected via the method described in section 2.2.2. Flow rates 0-900 μL/min were investigated to characterise the stiffness of the simple valve. The range was then reduced to 20-400 μL/min for the visualisation of flow patterns through the valves. These two experiments lead to the investigation of pulsed flow on the flexible valves. Pulsed flow was used to investigate the flow patterns on opening and closing of valves as well as particle accumulation.

2.2.3 Flow Visualisation

Microscope set up

The microscope (Nikon Ti-U, Japan) was set up for GPV. In order to do this, first the device needs to be in focus with a x20 magnification objective before focusing and centring the light into Kohler Illumination. Then the numerical aperture of the condenser lens, NA_c was reduced to optimise the visualisation of the speckle pattern, as mentioned in section 1.3.2. The position was just under half-way closed, which was estimated to be around $NA_c = 0.15$ and 0.20 which equates to a speckle diameter of $\approx 3\mu m$ [124] for a height, $H \approx 100\mu m$. For the 3D printed milli-fluidic devices the aperture needs to be closed more due to the interference of scattered light from other planes. After the microscope is set up for speckle detection, it is then possible to capture the flow.

Image Processing

It is possible to enhance the speckle pattern using ImageJ [5]. In literature 1000-4000 frames were recorded [84], however the channels were quite a bit deeper than the channels used in these experiments (70-135 μm) therefore only 100 frames were captured and validated (see

section 3.1.1) to ensure that this was sufficient for measuring accurate velocity profiles. The static contribution can be obtained by subtracting the median from each of the frames. This process removes any dust on the camera lens/objectives (see figure 2.15) [84, 5].

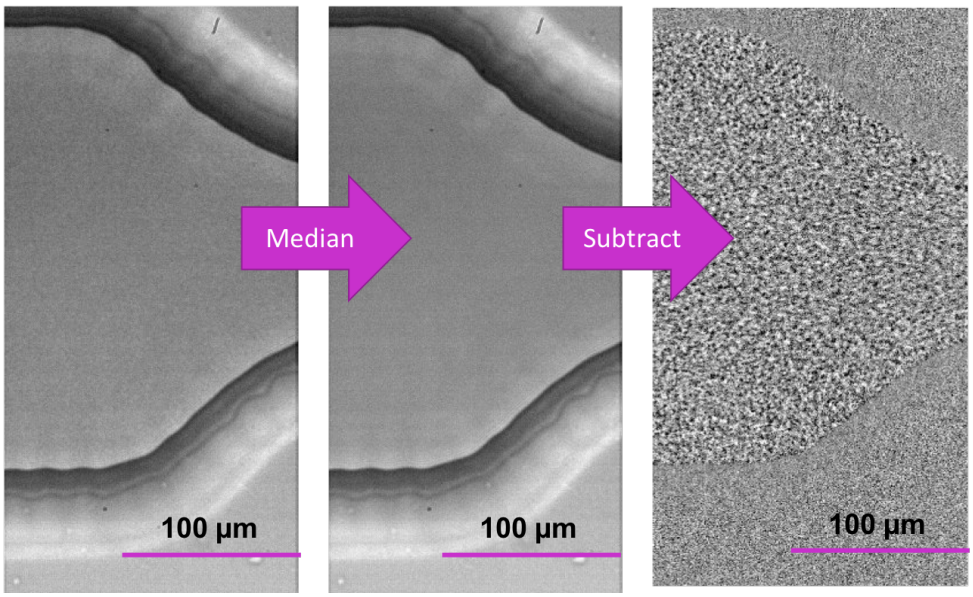

Figure 2.15: Flow diagram showing the image processing carried out using imageJ for GPV[5]

Data Analysis

It is then possible to track the speckle pattern from frame-to-frame, 1-2, 2-3, 3-4...etc using an open source matlab programme PIVlab [125]. PIVlab is commonly used as the title suggests for particle image velocimetry, as it uses the same cross-correlation calculations [126, 127, 84].

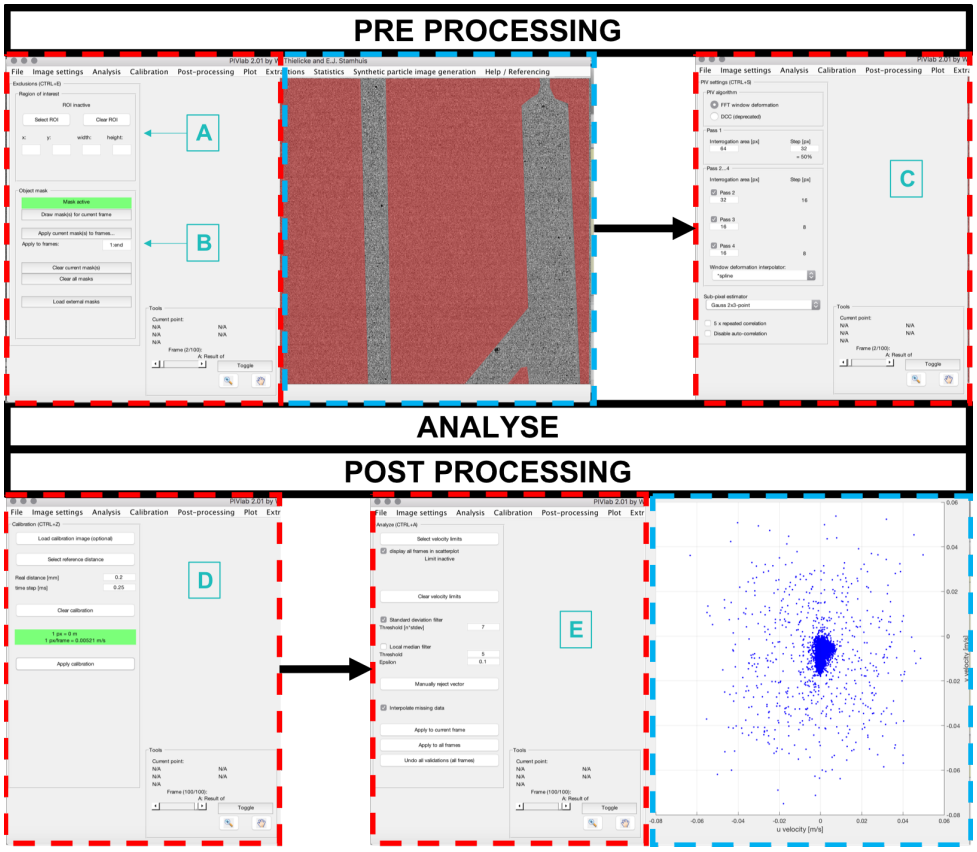

Figure 2.16: A visual of the standard procedure carried out using PIVlab. A) indicates where the ROI can be set and B) where the mask can be set. This can be drawn manually or imported. C) Is where it is possible to set the area at which an average of vectors can be considered. With this example a small area can be used as the GPV is of a high quality. After the analysis has occurred and vectors have been computed. Post processing can occur. Firstly, D) the calibration of the velocity to operate in m/s compared to pixels per second along with the setting the reference distance. Finally E) vector validation to remove anomalies

Firstly, a mask is applied to each of the images to exclude regions without flow (figure 2.16 A). The mask is applied to every frame. A ROI can also be isolated in order to investigate a specific region. Secondly the cross-correlation calculations are computed between each frame and then data processing can occur. PIVlab plots vectors by taking an average of surround pixels. The area at which the mean vector is taken was dictated by the parameters inputted into PIVlab. This parameter is specified within as 'interrogation area' and depend-

ing on the quality of the data can be manipulated. The smaller the region the lower number of pixels are averaged and therefore more accurate the data. In most of this thesis the interrogation area is usually set to 16 pixels. Vector validation is carried out to keep the vectors which are corresponding to flow figure 2.16 E). In order to calibrate the vectors channel dimensions need to be imputed as well as frames per second instead of frames per pixel using the following equation:

$$pixelspersecond = \frac{1}{fps} \tag{2.2}$$

One validation approach is to ensure that the experimental velocity is matching the theoretical velocity with equation 2.3:

$$u = \frac{Q}{A} \tag{2.3}$$

Where u is the velocity, Q is the volumetric flow rate (m^3/s) calculated from the flow rate set by the syringe pump and A is the cross sectional area of the microfluidic channel ($W * H$). Obviously there was an increase velocity through the stenosis compared to the rest of the channel, this resulted in two data sets having to be taken per device in order to capture the flow through the restriction and the main channel. One frame rate was used to acquire flow through the main channel and a higher frame rate was used for through the stenosis. The second way to validate the GPV results is to ensure there is little difference from frame to frame and velocity measurement [100]. Finally the third validation is the use FEM to back up the experimental findings.

2.3 Simulation

Various open source software was used to carry out finite element, FE, multiphysics simulations. For the stenosis model 2D and 3D simulations were carried out and the valve model, only 2D simulations. Once the geometry is drawn as seen in sections 2.1.1 and 2.1.3 they can be exported from AutoCAD as a .iges file into to an open source meshing software Gmsh [128]. Gmsh is used for tetrahedral meshing and is recommended by the multiphysics soft-

ware Elmer [129]. Elmer is a finite element software meaning it requires a mesh to carry out the simulations. Once the mesh has been optimised in gmsh it is exported as a .msh file and can be opened in Elmer to start a new project. The use of a mesh-based simulation meant that simulations were relatively quick due compared to more complex particle based methods. It was also easy to set boundary and body (i.e. fluid and solid) conditions. The equations and material properties can be directly applied to bodies (fluid and valves).

Murine Model

For the stenosis model a steady state model was solved using the Navier-Stokes equation. The Navier-Stokes equation is based on fundamental principles: conservation of mass, momentum and energy. In brief, it comprises of momentum and continuity equations as well as taking into consideration stress tensors for Newtonian fluids. Within this thesis it is recognised that blood is a non-Newtonian fluid, however to act as validation for the experimental model Newtonian flow conditions where used. Constants are set as prerequisites of the model and are stated in table 2.2.

Table 2.2: Necessary values to remain constant throughout all simulations

Prerequisite	Value
Stefan Boltzmann	$5.67e^{-08}$
Permittivity of Vacuum	$8.8542e^{-12}$
Boltzmann Constant	$1.3807e^{-23}$
Unit Charge	$1.602e^{-19}$

The flow within the device is also assumed to be non compressible. Therefore the programme Elmer computes the following equation: [130]:

$$\rho\frac{\partial\vec{u}}{\partial t}+(\vec{u}\cdot\nabla)\vec{u}-\nabla\cdot(2\mu\bar{\bar{\varepsilon}})+\nabla P=\rho\vec{f},\nabla\cdot\vec{u}=0 \tag{2.4}$$

where ρ is the density, $\vec{u}$ is the velocity, $\bar{\bar{\varepsilon}}$ is the strain tensor, p is pressure, t is time the term $\rho\vec{f}$ is the force due to gravity and μ is the viscosity combined with example boundary

conditions:

$$v_x = 0.1$$

$$v_x = 0$$

$$v_z = 0$$

In ElmerFem it is suggested that the flow in the x direction (v_x) is where to set the desired velocity, and as this is laminar flow flows within the y and z direction (v_y and v_z) can be set to 0 as it is assumed that there is no gravitational affects effecting v_z on the flow and due to laminar flow conditions there should be no other forces pushing the flow in the y direction. A parabolic flow regime can be set from the very start of the channel with the following equation:

$$v_x = 6 * (tx - 1) * (2 - tx) \tag{2.5}$$

Where tx is the inputted velocity. All boundaries were given a no-slip condition. At the outlet only the v_y condition is defined and is also set to 0.0 m/s.

The number of iterations was increased to 500 allowing more time for the simulation to converge. The main body is given the material properties of water at room temperature (298 K) meaning that the density was set to $1000 kg/m^3$ and dynamic viscosity to $8.9 * 10^{-4}$ Pa.s. The fluid is stated to be non-compressible. Due to the length of the channel before the stenosis is long enough the inlet velocity does not have to be set to have a parabolic profile. This was planned to replicate the conditions of the experiment. The parabolic profile occurs over in the channel (see section 3.1.6). The boundary conditions were set as follows:

- Inlet = x velocity was set to the flow rate (m/s), y velocity was set to 0 as the flow is laminar. The side branch geometry was given a second inlet parameter in order to control the inlet velocities independently of each other.
- Outlet = setting the y velocity to 0. Although in the majority of simulations the pressure is usually set to 1 atm, this is not necessary for these simulations
- Walls = No slip boundary conditions

The number of nodes for each geometry is presented in table 2.3 and an example of the mesh used throughout the simulations can be seen from figure 2.17. In the following mesh's there is no refinement factor throughout the main channels, however there is the same refinement applied to the stenosis region. The refinement is a progression throughout the stenosis lines by a factor of 10.

Table 2.3: A table to present number of numerical elements and nodes within each mesh of the stenosis model

Geometry	Solver	Number of Nodes on line	Number of Surface Nodes	Number of Nodes in Volume	Number of Tetrahedra	Number of Triangles
2D-Stenosis	Navier-Stokes	244	95	NA	NA	436
2D-Side Branch	Navier-Stokes	281	115	NA	NA	532
2D-Closed Side Branch	Navier-Stokes	233	95	NA	NA	441
3D-Stenosis A	Navier-Stokes	484	3330	1556	20064	NA
3D-Stenosis B	Navier-Stokes	616	5162	2850	33384	NA

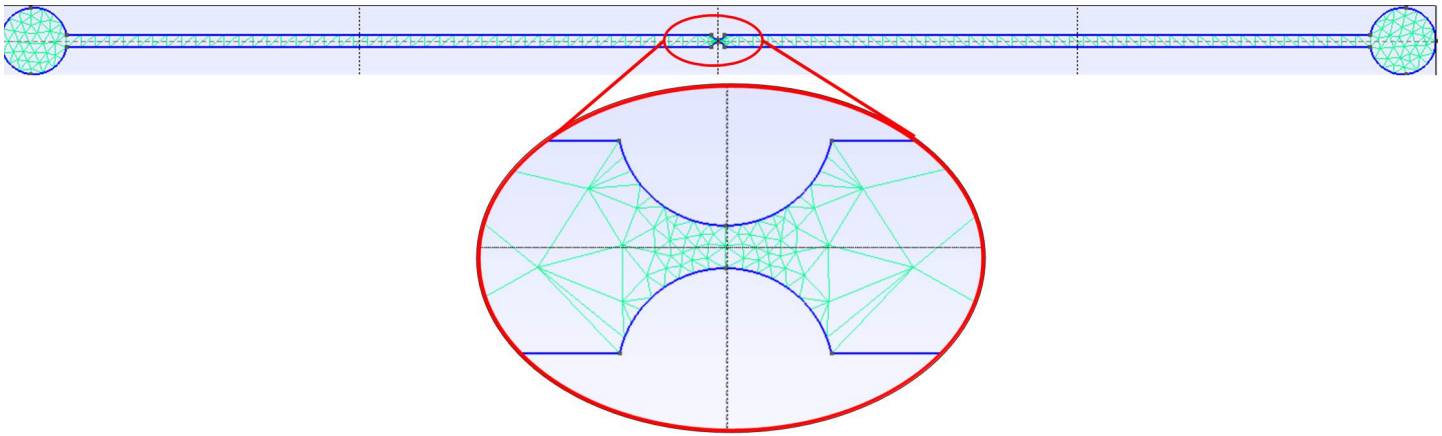

Figure 2.17: Figure showing the standard mesh used for the 2D simulations, there is slight refinement around the stenosis to account for faster velocities

Valve Simulations

The valve model was slightly more complex as the deformation of the valves was added to the simulation to replicate the experimental conditions. In order to add deformation, the fluid body had to under go mesh deformations, while the valves underwent a non-linear elasticity solver. An example of the .sif files will be added to the appendix (A.1). However, for completeness, the boundary conditions are same as above, along with the added boundary:

- Valves = Given an non slip boundary condition for the Navier-Stokes equation, Elasticity was varied to observe how elasticity may influence flow.

The quality of the mesh is crucial for FE simulations. For this reason various mesh's were tested and optimised. For the deformation studies the mesh was partitioned to attempt to alter the two bodies (2.18 C), solid (valve) and fluid (main body). This partition would be highly useful for understanding fluid-structure interactions. In order to ensure the solvers are run in the correct order: flow solver, elasticity solver and finally the mesh deformation solver. This will make sure that the 'solid' bodies are responding to the force acting on them (velocity) and then the fluid responds to the moving valve.

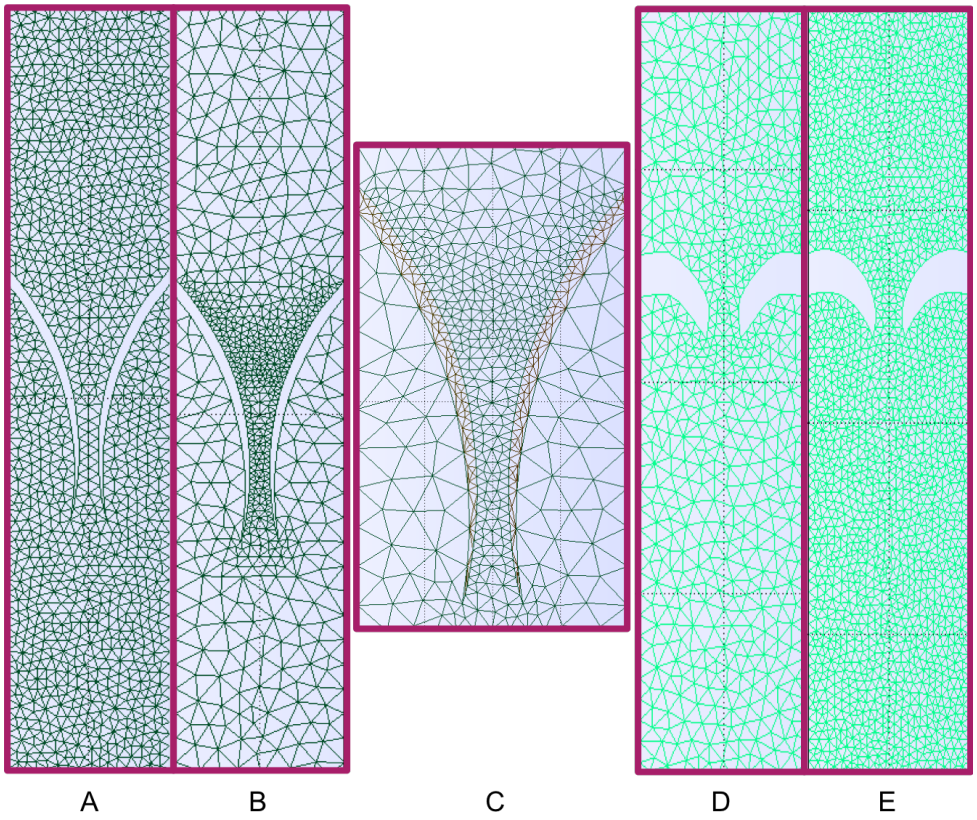

Figure 2.18: Images showing the different mesh refinements for each geometry. A and B show the valve which is taken from the CAD file for the photo-masks, C shows the mesh partitions for the vavles and the fluid and D and E show the short thick valves to look at an extreme geometrical change on the fluid flow

Table 2.4: A table to present number of numerical elements and nodes within each mesh A-E, along with equations applied

Geometry	Solver	Number of Nodes on line	Number of Surface Nodes	Number of Elements	Refinement
A	Navier-Stokes	516	3449	7412	0.1
B	Navier-Stokes	322	1080	2468	1 for majority of mesh and 0.1 though valves
C	Navier-Stokes Non-Linear Elasticity Mesh Deformation	334	1148	2746	0.1 with refinement factor of a further 0.1 on valve boundaries
D	Navier-Stokes	140	597	1332	0.1
E	Navier-Stokes	242	1891	4022	0.01

The number of iterations was also kept the same as previous simulations, however a re-

laxation factor was implemented on the primary solvers (elasticity and fluid flow), of 0.5 and the number of non-linear iterations to 1. This does not apply to the mesh deformation solver as it just determines the displacement of the elasticity solver in response to the fluid solver. The methodology for following both the murine and valve simulations was carried out similar to that in the Elmer GUI tutorials [130] with parameters altered to match experimental conditions.

Finally the analysis of the FE simulations was carried out using another open source software, Paraview. Therefore, the output file was set to .vtu. Using paraview it is possible to extract the pressure and velocity magnitude maps and are presented in the results sections 3.1.6 and 5.19.

CHAPTER 3

STENOSIS MODEL

The stenosis model is a popular choice for *in vivo* studies of DVT, in particular the murine model (discussed in detail 1.2.1). For this reason it seems an appropriate place to start developing an *in vitro* model. The purpose of this chapter is to 1) optimise the GPV set up to capture 2D and 3D flow profiles, 2) use GPV to explore flow patterns before the stenosis to investigate why thrombus formation occurs and 3) add complexity by investigating how the presences of closed and open side branches may influence flow around the stenosis region of interest.

3.1 Results and Discussion

3.1.1 Optimisation of GPV set up

The ability to detect the speckle pattern for GPV is dependent on the camera specifications. Generally there is a trade off between fps and field of view meaning that as the fps increases the field of view decreases. The camera has to reduce the resolution in order to raster in the x-direction quick enough to achieve the higher fps. In this case two cameras were used to determine which set up would be optimal for the future experiments. The two cameras were the SA3 and SA5 mentioned previously in materials and methods section 2.2.2. It became evident early on that the SA3 did not have the resolution at high fps required to capture the

speckle pattern, even for the large devices (500μm), see table 3.1.

Table 3.1: A table presenting to performance of the CMOS cameras used for capturing GPV

	SA3	SA5
Max fps	60, 000	1, 000, 000
Max Resoltution (px)	128 x 16	64 x 16
Required fps *	30, 000	30, 000
Resolution	256 x 48	768 x 320

The * seen in table 3.1 is to indicate the maximum fps used in the GPV experiments. As seen in 3.1 the major limitation for both cameras is when the fps is at its highest the resolution drops drastically. For the SA3 this happens a lot sooner than the SA5. Capturing GPV through the stenosis region of interest, ROI, means that the ROI is relatively large. Therefore, it is necessary to determine which fps is required to capture the whole ROI. The restriction causes the velocity to increases therefore, fps needs to be greater than in the channel. For this reason, in some cases, multiple captures at different fps were needed to ensure a reliable measurement of the velocity through the whole stenosis area. With a greater stenosis there is a greater difference in velocity from the main channel and in the middle of the stenosis. It was established that the SA5 camera was the most suitable in order to capture the GPV speckle pattern over a relatively larger area in comparison to the SA3. Both fps and shutter speed were investigated to optimise the visualisation of the speckle pattern through the microfluidic device. Once all parameters were established it is possible to take accurate measurements using GPV within one plane (figure 3.1).

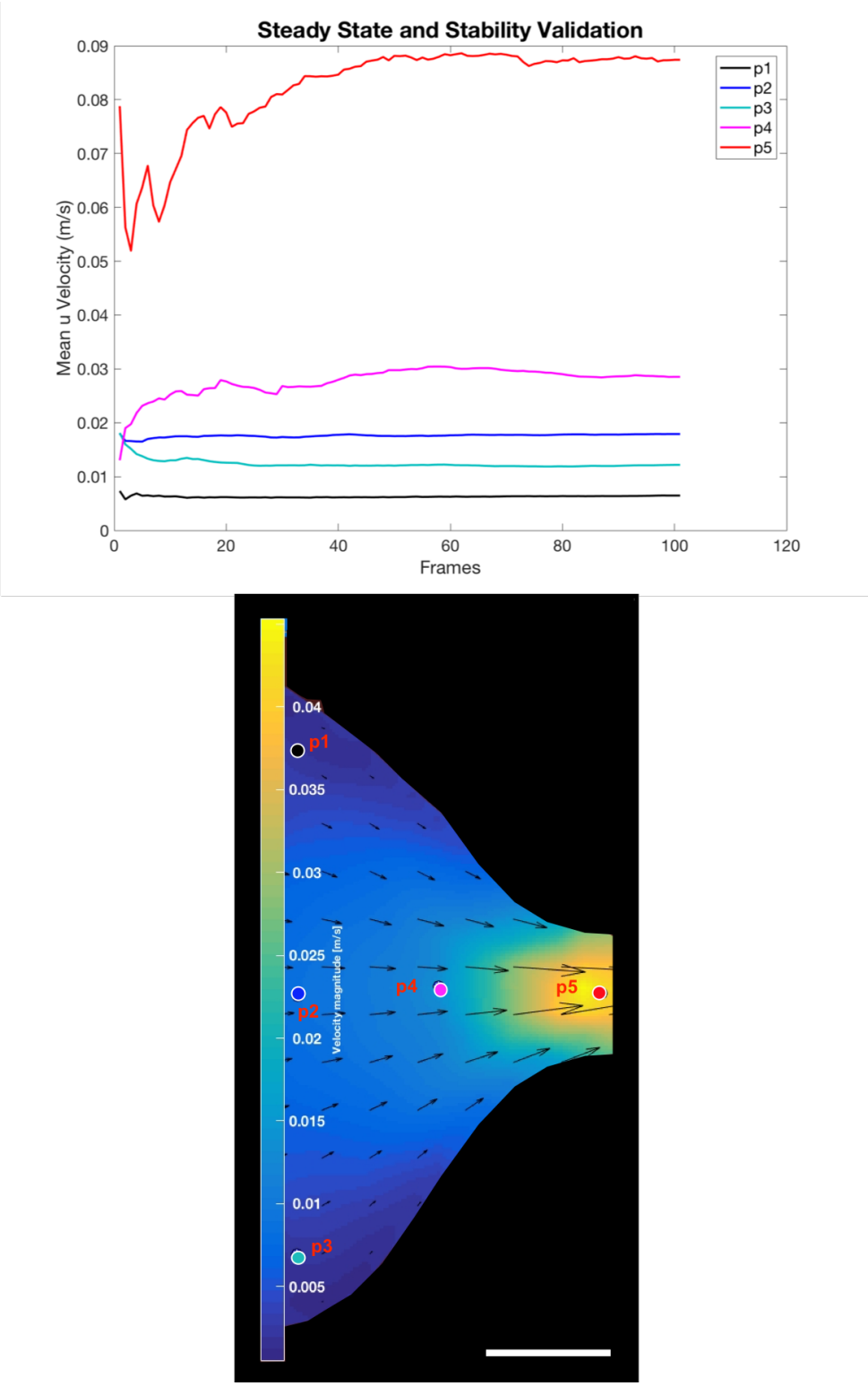

Figure 3.1: A graph showing that the flow is in steady state within the 100 frames recorded. This particular graph is for flow rate 20 μL/min and a fps of 20 000. Scale bar = 40 μm

In order to validate the selection of 100 frames, it is possible to use the approach used

by Riccomi et al. [100]. The positions represented as p in figure 3.1 are indicated in the velocity map plot with complimentary colours. It should also be noticed that in figure 3.1 the first 20 frames are not very steady for position 5 (P5) which is the stenosis region. This is due to the frames per second not being high enough to capture the displacement of the speckle pattern. As seen previously by figure 3.1. For this reason a minimum 100 frames were used in all microfluidic experiments throughout this thesis. The reliability of the GPV set up is displaced below in figure 3.2 the data points are taken from before the stenosis and therefore are slightly higher than the theoretical velocity of the main channel if $W = 200\mu m$. However, the theoretical velocity through the stenosed region has a much greater gradient because due to the smaller channel width ($w = 40\mu m$) the velocity is more susceptible to change considering that the velocity is proportional to the cross-sectional area of the device according to equation 2.3.

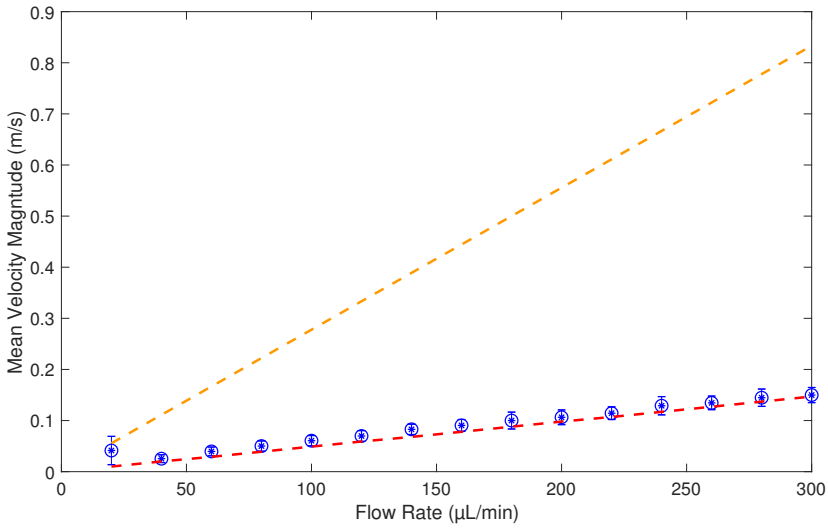

Figure 3.2: This is a graph to show the reliability of the GPV set up including: syringe pump and image capture. The theoretical velocity through a $W = 200\mu m$ channel is displayed by a red dashed line and the orange dashed line is the stenosed region of 80 % with a $w = 40\mu m$. The experimental result is presented by the circular data points.

To progress the experiment further, plasma was used to try and observe GPV. Plasma is optically transparent and contains a high proportion of blood proteins (albumin, globulins

and fibrinogen). It was thought that perhaps the concentration of proteins would be high enough to refract the light similar to that seen previously in the GPV experiments. As you can see from table 3.2, the concentration of proteins is substantially higher than that used for GPV ($0.1-0.2\,w/v\%$).

Table 3.2: A table to present proteins in blood plasma and their corresponding sizes

Protein	M_w(kDa)	Size (nm)	Concentration(w/v %)	Ref
Albumin	66.5	9 x 6 x 5 nm	3.5-5.5	[131, 132]
Globulins	93- 1193	> 10 nm	0.15-0.4	[133, 134]
Fibrinogen	≈340	rod shaped 9 x 47.5 x 6 nm	2.6-3.5	[135, 136]

Clearly another important parameter to consider is the refractive index, *n*. For a healthy human the refractive index of blood plasma is $n = 1.35$ [137] where as the refractive index of PS nanoparticles in suspension is $n = 1.59$. These parameters should have been suitable for the capture of a speckle pattern in a microfluidic channel, however the proteins in blood plasma are too small and the refractive index of the proteins is too similar to plasma. This stops the speckle pattern occurring. However, if blood plasma was to be diluted it could be a suitable alternative for GPV analysis. This would be a useful alternative for if/when cells are added to the stenosis devices as nanoparticles are toxic to endothelial cells [138].

3.1.2 Flow through Symmetrical Channel

The symmetrical channel was used to optimise the microscope set up, various fps and shutter speeds were investigated. For this 80% stenosis with $w = 200\mu m$ devices was used. The establishment of optimum conditions for the different flow rates ($20-200\mu L/min$) the investigation of flow around the stenosis can be carried out. The theoretical values of velocity (calculated via equation 2.3) closely match the experimental results in the microfluidic channels. A thrombus occurs before the stenosis in murine models [139], however in arterial clot formation it initiates after the stenosis [73]. Arterial models and venous models are not comparable for thrombus formation. Therefore, due to thrombosis occurring before the stenosis

in the murine model the ROI within the microfluidic channels will be before the stenosis. An example of a typical velocity profile map can be seen in figure 3.3 and should be noted, what can be seen is the smallest channel (200 μm) with the largest stenosis (80 %) which is mimicking the murine model idyllically. The diameter of a mouse IVC is 200-300 μm and within the stenosis they restrict the vein by 80-90 %, the conditions is mimicked within the x-y plane below in figure 3.3. *In vivo* the stenosis is 3D and the percentage is defined by the diameter in which it is smaller than original diameter of the blood vessel. In the microfluidic case, the restriction can only be applied in the x-y direction, meaning it is a 2D restriction.

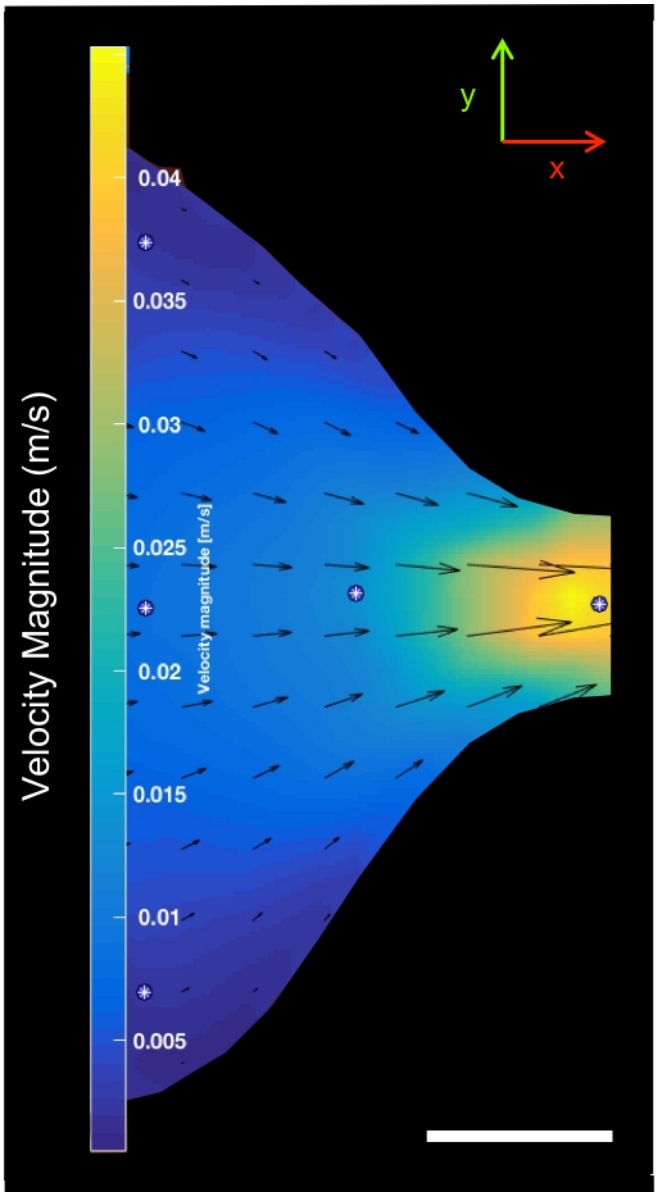

Figure 3.3: A velocity magnitude map of the 200 μm microfluidic channel with 80 % stenosis. The flow rate here is 20 μL/min and the capture rate is 20 000 fps with 50 μsec shutter speed. The markers seen on this velocity plot are to determine the steady state of flow over a 100 frames and the results can be seen in figure 3.1. Scale bar = 40 μm

It was determined that the optimum shutter speed was 50 μseconds to achieve the most reliable GPV. This can be confirmed using the same steady state validation plots as seen by 100 frames. The respective graph can be seen from figure.

Obviously at these flow rates the Reynolds number, Re =0.0005 - 0.005 (using equation

1.1 and flow rates $20-200\mu L/min$) which is a laminar flow regime. Although these values would appear low, they are well within the Re numbers for a mouse IVC [140]. According to literature the mean velocity of blood flow through a mouse superior and inferior aorta is 18 *cm/s* with the hydraulic diameter, D_H, of $1.09mm$ [140]. The dynamic viscosity of mouse blood at sheer rate $94s^{-1}$ is 4.9 *mPa s* [141] and the density is 1.057 g/cm^3 [142]. Using equation 1.1 the *Re* = 66, however when the velocity is reduced to 3 *cm/s* and the viscosity is $13.4mPas$ at $0.7s^{-1}$ the density would remain the same and the D_H would be 0.2 mm [32] the Re number would be as low as 0.0005. Meaning that it is possible to mimic the venous system of a mouse relatively accurately and therefore flow patterns will be relatively the same as *in vivo*. The only parameter not taken into consideration which may affect the flow patterns around the stenosis are the non-Newtonian properties of blood flow.

Before the stenosis there was no indication of any complex flow patterns occurring (e.g. vortexes) indicating that perhaps fluid flow is not the parameter inducing thrombus formation. In fact, a strong possibility for a thrombus forming before the stenosed region is the 'bottle-neck' effect. As the red blood cells and platelets flow through the IVC of the mouse, when they approach the stenosis area there is a back up of blood cells and in effect will have more cell-cell interactions which increases the likelihood of clot formation [143]. This would not happen in arterial models as the flow has a much higher velocity resulting in the re-circulation after the stenosis activating the platelets and causing thrombus formation[73]. This could explain why there is different thrombus compositions in the murine and *in vitro* models[73].

3.1.3 Flow with the presence of a Closed Side Branch

The closed side branch aimed to represent those side branches that were ligated, therefore mimicking a deformity in the IVC. It is also discussed in literature that even when the side branch is ligated, thrombus formation is affected [53]. The presence of the closed side branch did not disrupt flow around the stenosis or the main channel itself. In larger devices it is possible to increase the flow rate (as seen in figure 3.4). It can be seen that even with

higher flow rates that there is no disruption to the laminar flow regime. Even at the maximum velocities at the centre of the channel equalling ≈0.08 m/s meaning that the $Re = 0.013$ when following equation 1.1.

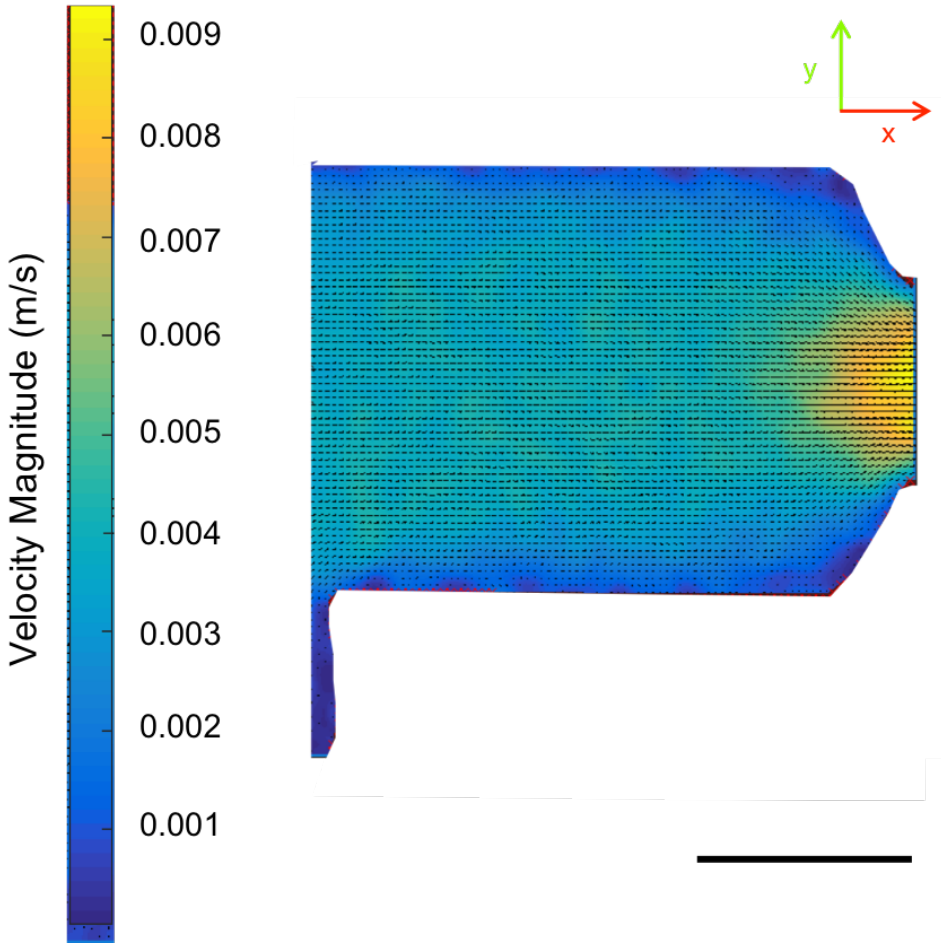

Figure 3.4: A velocity magnitude map of the 500 μm microfluidic channel with 80 % stenosis. The flow rate here is 40 μL/min and the capture rate is 10 000 fps with 50 μsec shutter speed. Scale bar = 250 μm

3.1.4 Flow with the presence of a Side Branch

The presence of a side branch did not seem to affect the flow regime through the device. It was suggested in literature that the presence of a side branch would modify thrombus formation. However, there is a distinct lack of understanding of fluid dynamics within mouse veins. For this reason both the usual polystyrene, PS, suspension and whole blood studies

were investigated. It is of general opinion that the side branch interferes with flow and can therefore initiate or alter thrombus growth, from these findings it was hypothesised that this was due to a recirculation at the top of the side branch, just before the stenosis. From a chemical engineering perspective of fluid flow, this would not be the case as the *Re* number of blood flow through the IVC of a mouse would be less than 2000 and therefore within the laminar regime. This is what was witnessed within the experiments carried out.

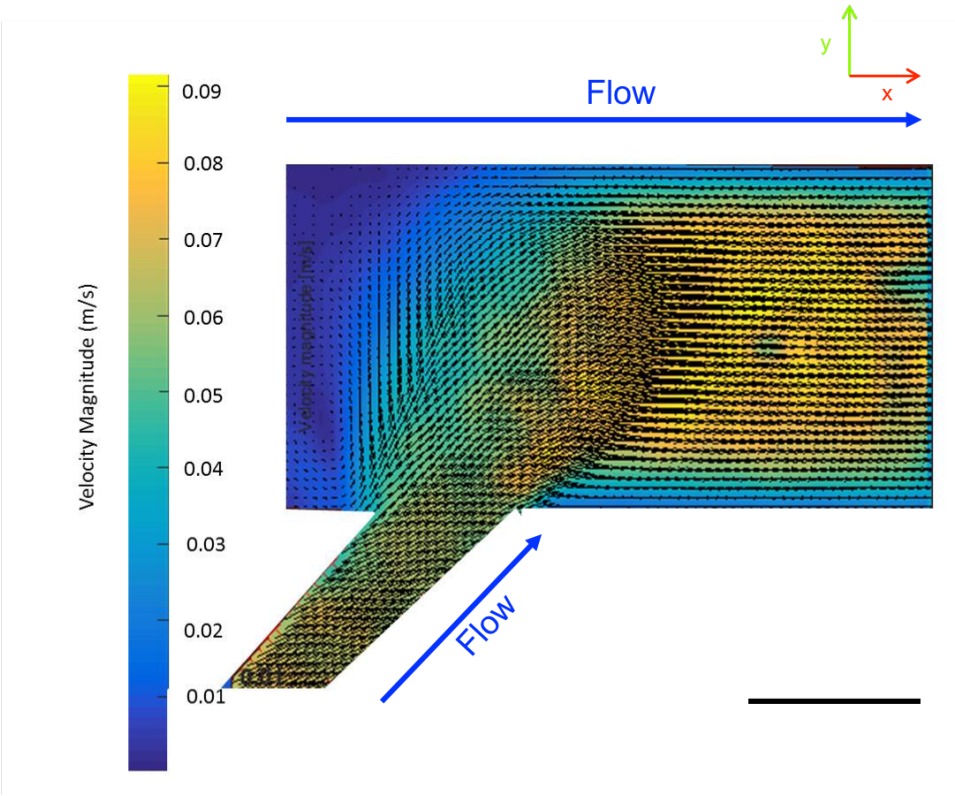

Figure 3.5: A velocity magnitude map of the 500 μm microfluidic channel with 80 % stenosis. The flow rates in the side branch and main channel are equal of 100 μL/min. Scale bar = 250 μm

This geometry has been explored in greater detail in the next chapter. To further prove the laminar conditions in the microfluidic devices whole blood was used.

Whole Blood Work

Using the side branch geometries, whole blood was investigated to determine how the location of the side branch with maximum stenosis (80%) would effect the blood flow. The aim was to better mimic the *in vivo* condition using whole blood. The blood was collected and used within 3 hours and was treated with EDTA to prevent it from clotting within the eppendorf. In order to visualise flow whole blood from a healthy subject was taken and pumped through the main channel along with PBS buffer. From figure 3.6 it is possible to see that even with independent flow rates of the side branch and the main channel there is no mixing of any kind when the side branch has a lower flow rate than the main channel. When the side branch is 10 times greater than the flow rate in the main channel there is recirculation and back flow within the channel. However, it should be noted and can be seen that the use of whole blood makes it very difficult to visualise specific flow patterns as mentioned previously in the introduction.

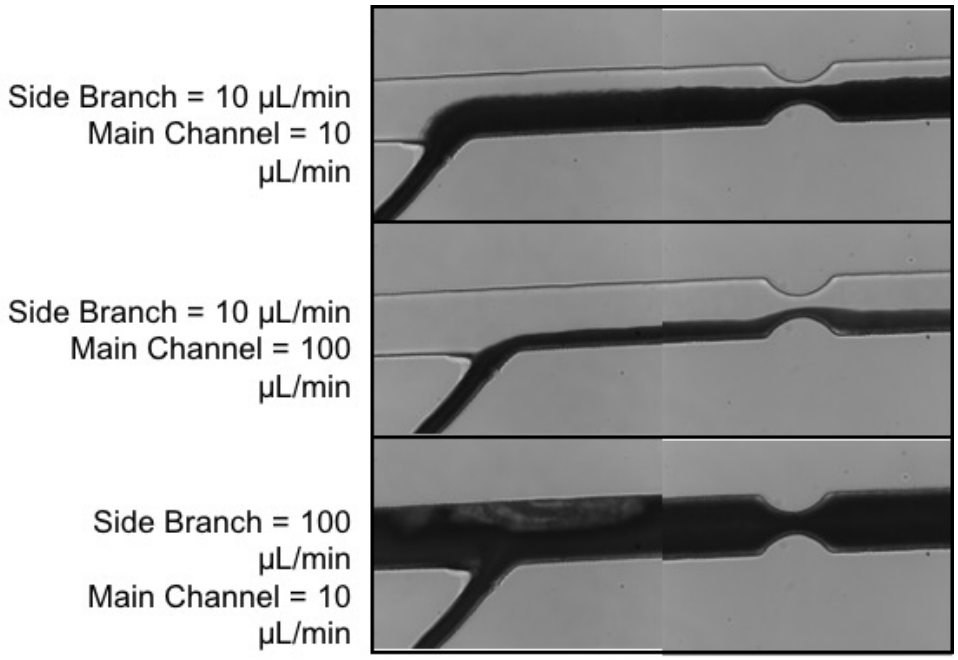

Figure 3.6: Bright-field microscopy images of blood flow through the 200 μm microfluidic channel with 70 % stenosis with side branch positioned 600 μm away from the stenosis.

After multiple parameters were explored, it was concluded that perhaps mimicking the

murine model is not the most efficient way to investigate how geometrical parameters will influence the flow patterns and in turn the initiation of thrombus formation. To visualise the video's capturing laminar flow through the side branch geometries proving the reproducibility and validity of these findings, please refer to video tape which is available upon request. The Re number of the whole blood in the side branch at 100 μL/min is 57 assuming that the density of blood is 1060 kg/m^3 and the dynamic viscosity is 3 times that of water [144]. Of course, this is variable depending on person-to-person.

3.1.5 3D Cylindrical Design

As mentioned previously in section 2.2.1 there were complications when it came to fabricating a full cylindrical device and for this reason the 3D flow analysis was carried out on half-cylindrical device (figure 3.7). Consequently advancing from the simple square cross sectional devices allowing for the investigate the influence of curvature with in the z-plane (as well as the x-direction) has on flow.

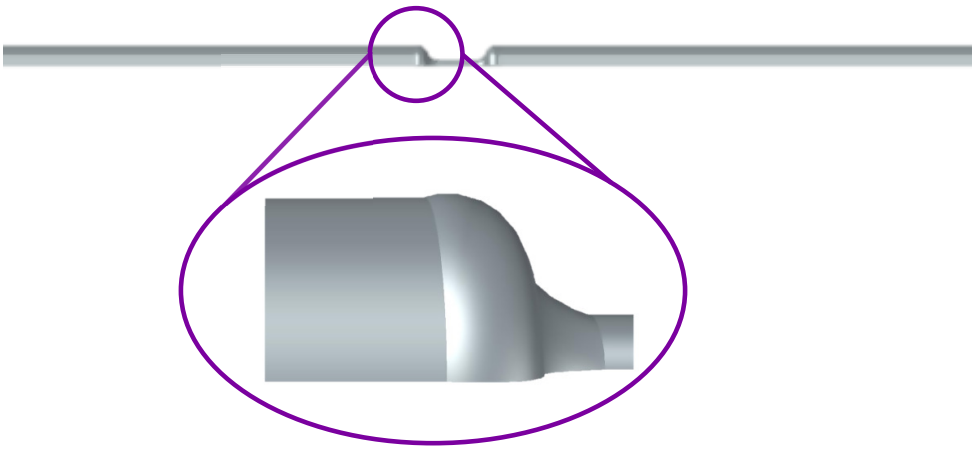

Figure 3.7: A CAD image showing final geometry for the 3D printed stenosis device highlighting a particular region of interest for the investigation of flow around the stenosed region

The 3D devices with cylindrical geometry present intrinsic optical aberration when observed using the microscope as the refractive index, n, of the water solution of polystyrene nanoparticles ($n = 1.33$) is different from the one of PDMS ($n = 1.41$). There are many ways to

match the refractive index of PDMS, one was to add sucrose solution to the water (48% w/v), when the refractive index matched that of PDMS. The nanoparticles have an electrostatic charge of which is slightly negative due to the carboxyl groups on the surface. However, due to the electrostatic shielding induced by the sucrose the nanoparticles severely aggregated even with the addition of surfactants (tween80, tween40 and sodium dodecyl sulphate (SDS)). The presence of large aggregates was problematic for GPV as they are within the diffraction limit of the microscope and will be resolved in a larger volume compared to the speckle pattern which is confined to a specific plane [84]. After exhausting this approach an alternative was found; by using a mixture of water and glycerol (58% v/v), and index match was achieved. As the mixture water/glycerol does not add electrolytes, aggregation will not happen, however the viscosity of solution will be altered to six times that of water. This also has a secondary advantage as it is closer to the viscosity of blood and consequently increases the Re number more representative of the human condition.

Once the refractive index is matched it was then possible to analyse the velocity profile at various points across the z-plane [84]. This is because $\delta_z \approx \lambda/(NA_c)^2$ where δ_z is the longitudinal speckle characteristic size μm and λ is the wave length of light (nm). By altering the aperture it is possible to see the 'speckle' pattern within tens of microns resolution [84]. The results show a parabolic profile across the z-plane as well as well as the x-plane indicating that the addition of a curved surface to the stenosis geometry has no effect. Thus indicating that flow through the micro and milli - fluidic devices is purely laminar within the experimental conditions of this thesis (velocity, viscostiy of fluid, etc.).

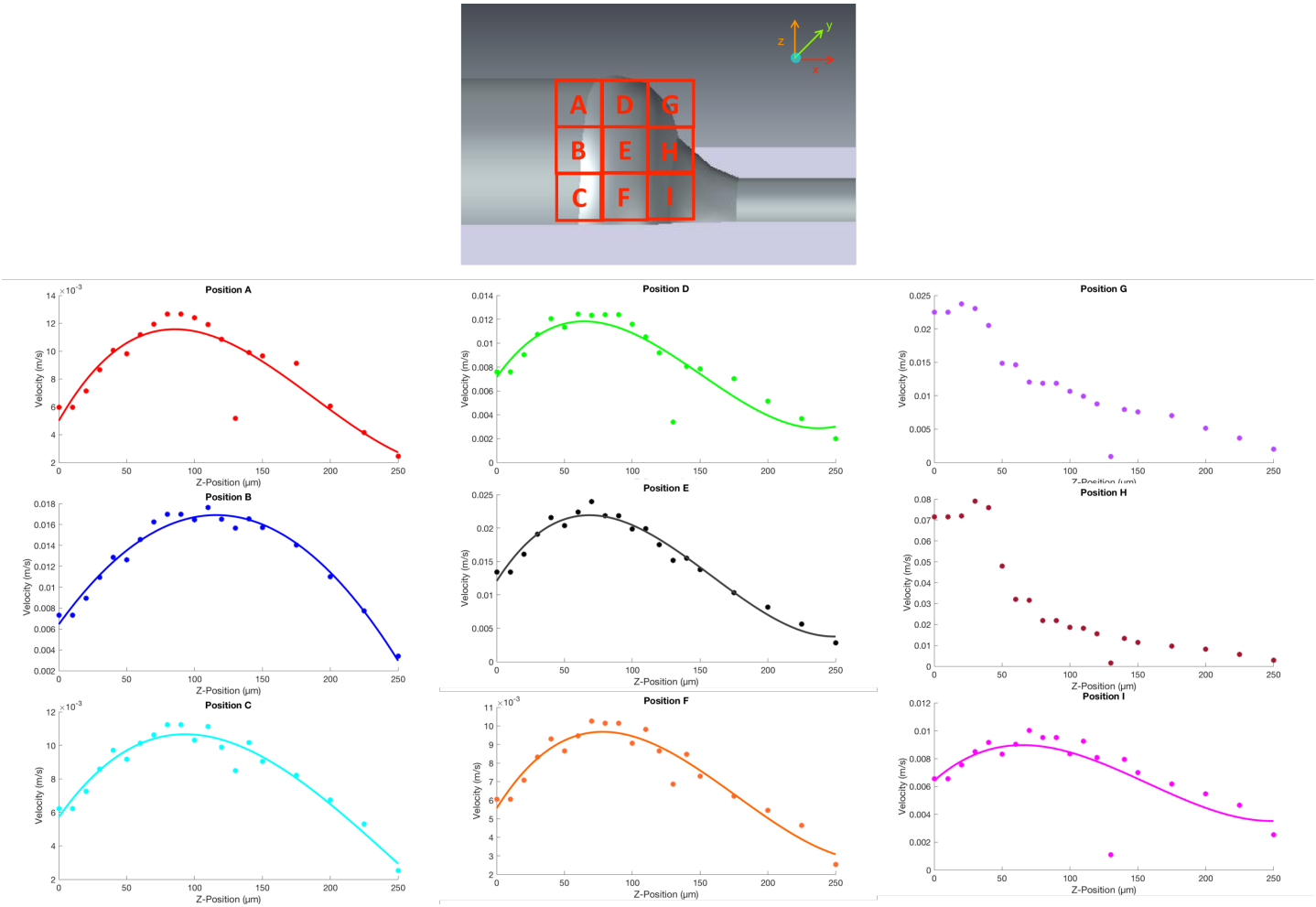

Figure 3.8: The velocity profiles of the z plane for the cylindrical device. The positions A-I are highlighted above the graphs

The velocity profiles in the z direction show that the flow is laminar. This is a half-cylindrical device so the tapering off of the velocity in plots A, C, D-E make sense as the slower velocities are closer to the channel wall. In particular velocity profiles D-E are entering the stenosis region meaning again that the z-position is closer to the vessel wall in comparison to previous z-positions. As for positions G-I, the velocity profiles are not at a high enough resolution to capture the velocity profile. Remember the stenosed region is 0.15 mm and this is not accounted for within this figure. This could be over come by using smaller step sizes to enable quantification of the parabolic flow in the z-direction through the stenosis region. However, this is not possible within the set up available. The stage control on the microscope is able to estimate the position within the z-direction, however this is not as accurate to be able to account for reliable smaller step sizes. However, it can be seen from position B, that parabolic flow is occurring in the z-direction as well as the x direction which is to be expected with laminar flow conditions. For this reason it can be assumed that even with the lack of whole blood experiments, that the flow patterns prior the stenosis would be translational according to Re number. It would also be apparent that the Newtonian influence of the fluid would be most prominent after the stenosis due to the differences in shear, the region not of interest within this model.

In addition to investigating the influence of curvature on flow patterns around the stenosis, the use of platelet rich plasma was also explored. It would be safe to state that there was no flow patterns prior the stenosis which would be of interest when trying to understand how thrombus formation occurs within murine stenosis model. For this reason, it would be relevant but bold to state that perhaps the induced stenosis model may not be a relevant for modelling DVT. There is a clear lack of acknowledgement of 'bottle neck effect' and how this could encourage clot formation within the stenosis model. Yet it is well known that increased cell-to-cell interactions would increase clot formation. The lack of coupling between these acclaimed statements suggests a severe underestimation between the connection of physics and biology when it comes to investigating DVT.

3.1.6 Simulation

The simulations were used to confirm the experimental findings, including that there is no 'turbulent' flow at the neck of the stenosis as is suggested in literature [33].

2D Simulations

. The use of open source software enhances capabilities of the user as well as being able to control the conditions of the FE simulation. This was certainly the case when it came to acquiring the following simulations. It is to be expected the flow through all devices is to be laminar, there for a parabolic regime is to occur. This can be seen in all of the following simulations. These 2D simulations were calculated using COMSOL multiphysics software. As you can see from figure 3.9 the experimental and computation results are complimentary to one and other. This was the same for the other simulations, which can be found in the appendix A.

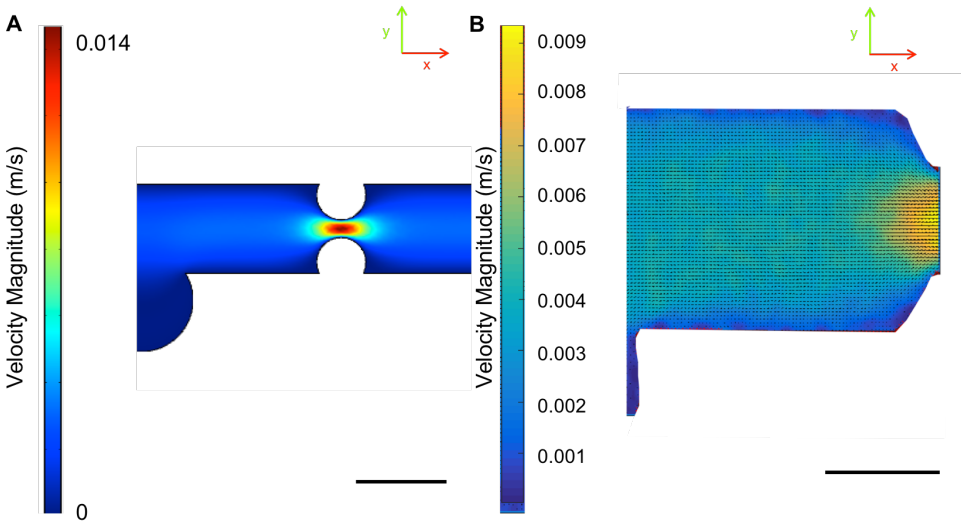

Figure 3.9: A is the simulation result calculated using COMSOL compared with B which is the experimental result of the closed side branch 500 μm channel with 80% stenosis. Scale bar A = 500 μm. Scale bar B = 250 μm

3D Simulations

The simulation results of the half-cylinder, were problematic. The first attempt used a relatively fine mesh with no refinement throughout the geometry. The velocity for this initial geometry was set to 0.1 m/s, which is on the higher end of the experimental velocities. It can be seen from figure 3.10 that there is an obvious mistake within the simulation. This is because we expect to see a higher velocity through the stenosed region, however this is not the case. It was suspected that the reason for this irregularity was due to an insufficient mesh density through the stenosed region. In order to over come this issue without increasing the converging time localised mesh refinement was carried out in order to achieve a more realistic parabolic flow condition, as experienced in the experimental results. The scale bar presented here is wrong, as the stenosed region of the geometry has not got an accurate velocity profile. Even after mesh refinement around the stenosed region there was still this error occurring which is not seen in the 2D COMSOL simulations carried out early on.

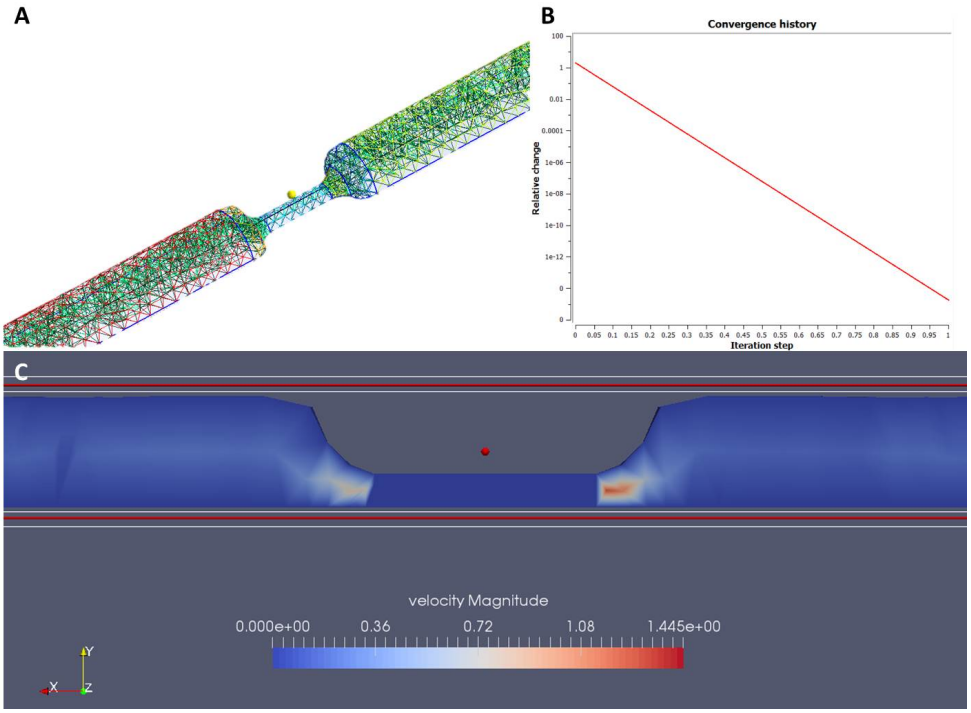

Figure 3.10: This was the first converging result using Elmer FEM software. Firstly A shows the mesh created in gmsh followed by the convergence history in plot which took 8.39 seconds B) and C) is the velocity profile result presented using ParaView

For reasons aforementioned the results in figure 3.10 are therefore deemed unreliable and not sufficient enough to validate experimental findings. The main reason for this error, is the need to investigate further mesh refinement around the stenosis region, especially within the volume. However, with the use of a full cylinder it was possible to run simulations which replicated the parabolic flow seen in previous experiments (see figure 3.11.

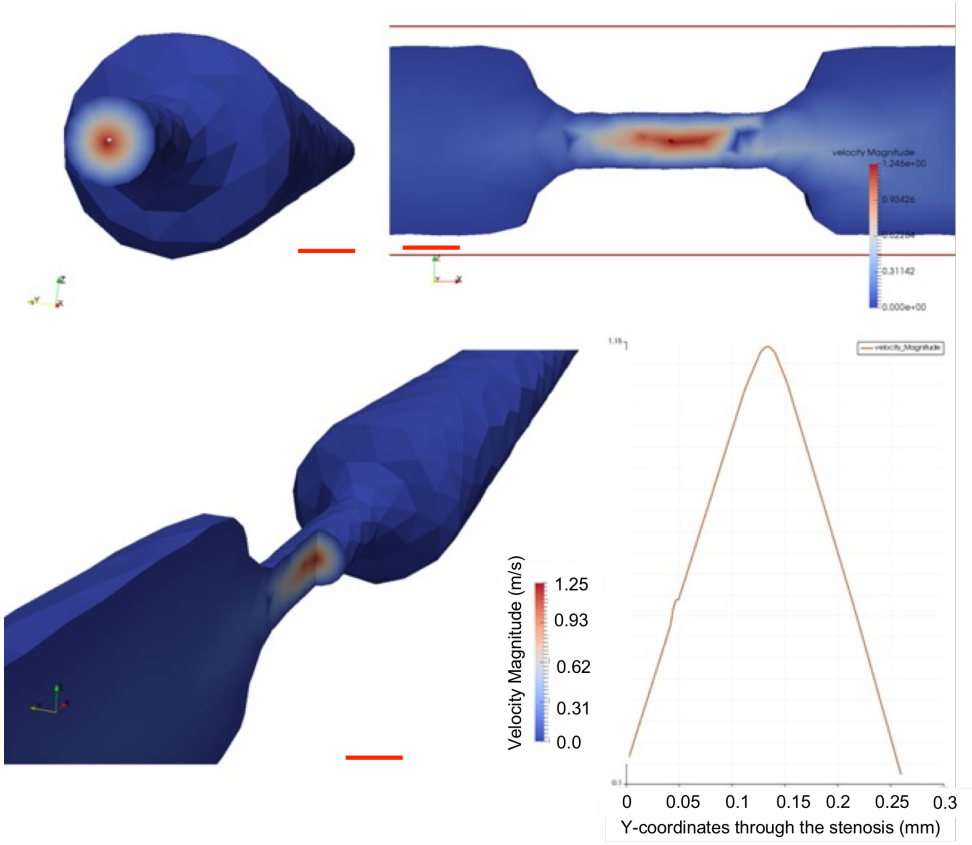

Figure 3.11: The velocity magnitude profiles of the cylindrical device with inlet velocity set to 0.13 m/s (near the maximum seen in microfluidic devices previously). The plot indicates the strong parabolic flow through the D=300 μm stenosis of the full cylindrical device.

The fact that the parabolic flow is occurring even at high velocities indicates that flow within a murine model is definitely going to be laminar and not exceed Re >2000 (see figure 3.11. The mesh for this particular result was created using Elmer automatically by importing the 3D structure via .iges file. This did not work for the 2D structures in previous simulations. There is no evidence of regions where recirculation would occur prior to stenosis and therefore must be due to the accumulation of platelets and red blood cells creating a 'plug', i.e. thrombus. A theory to why thrombosis occurs in this way could also be explained using fluid dynamics. It is known that larger particles are pushed toward the boundary in parabolic flow conditions. In this case it would be red blood cells. If the red blood cells were are at a greater concentration at the boundary when they reach the stenosis they are going to be pushed to-

gether forming a nucleation point. This nucleation point would instigate to accumulation of platelets, which are travelling faster within the centre of the vessel and result in coming to a drastic slow down/halt. This would then initiate the formation of a thrombus and explain why the venous thrombosis has an alternate physiology to arterial thrombosis and why the thrombus does not form on a vessel wall. The parabolic flow forces larger particles (red blood cells) to the vessel walls. This would cause a nucleation point for the platelets encouraging aggregations.

Sub sections 3.1.2 to 3.1.4 have been successful at determining:

- The optimum optical set up in order to capture GPV for accurate velocity profiling
- Determining that it is possible to use 200 μm microfluidic channels with 80 % stenosis and still be able to track velocity profiles through the stenosed region
- Proof, although already know, all flow is laminar within these dimensions which is similar to *in vivo* murine conditions [32].
- The side branch does not disrupt flow around the stenosis meaning further investigation is needed to understand how side branches influence thrombus formation and growth.

It should also be noted that these results can be advanced further, with more advanced blood investigations including using fluorescently labelled platelets to determine where they aggregate/adhere to the channel wall.

CHAPTER 4

BYPASS MODEL

After presenting the fact that stenosis does not seem to alter flow patterns or cause stagnant regions the questions arises, "what about the rest of the mouse?". The cardiovascular network is a complex pipework system with multiple routes to and from the heart. If a mouse has the IVC ligated (100% restriction), it will continue to live normally, therefore there must be an alternate route back to the heart. With this in mind it is possible that when the stenosis is within a certain distance from a side branch it will cause a pressure drop which will induce the blood to bypass the stenosis preventing thrombosis to occur. This is what happens in industrial pipe lines if there is a blockage, an alternative route is found or the plant stops all together due to a pressure increase/drop in a particular section. Valves are put in place in order to prevent blockages or encourage a diverted route [145]. It is reported that the position of side branches and back branches correlate with the size and occurrence of a thrombus within the IVC of a mouse [33]. A simplistic approach has been used to study a bypass design of micro-vasculature. A similar approach has been used to investigate a pressure drop in microvasculature [146]. It was found that red blood cells travel through the main channel and stenosis in laminar flow conditions, as to be expected with microfluidic dimensions. They compared water, diluted red blood cell suspension and a artificial blood solution (10% glycerine) and found that there was a linear relationship between pressure drop and the velocity of side branch through a 40% stenosed channel [146]. Within this chapter a wide range of controlled conditions are investigated, including: position of side branch, flow rates and

degree of stenosis.

The following results provide evidence that a bypass can occur depending on a pressure drop. Evidence will also be presented indicating how the position and width of the side branch can influence stagnant regions within the channel. These stagnant regions highlight regions where thrombosis is likely to occur. As emphasised in the introduction both these geometrical parameters are pivotal for thrombus formation and growth *in vivo* [33, 10]. There are no reports of valves in the murine model, suggesting a bypass is more plausible. This chapter therefore aims to provide evidence that: 1) a bypass is possible and 2) which parameters are most important to consider.

4.1 Results and Discussion

The complexity of the device meant there was a wide range of velocities through the different regions. As mentioned previously in the introduction, one of limitations of the camera is the ability to track the velocity. It is important to get the frame rate right in order to measure the speckle pattern displacement. Therefore, when the flow appeared stagnant, a lower frame rate was selected to ensure this was an accurate result. Throughout this chapter 4 regions of the bypass device will be referred to: the **main channel, bypass** and **side branch**, all of which are labelled in figure 4.1. In the plots there will be reference to main channel before the side branch (MCB4), main channel after side branch (MC Aft SB), main channel after the stenosis (MC AftSten), side branch (SB) and bypass (BP). To reiterate the three positions of the side branch: **position A** = 1600 μm, **position B** = 600 μm and **position C** = 300 μm away from the side branch (as stated in section 2.1.2).

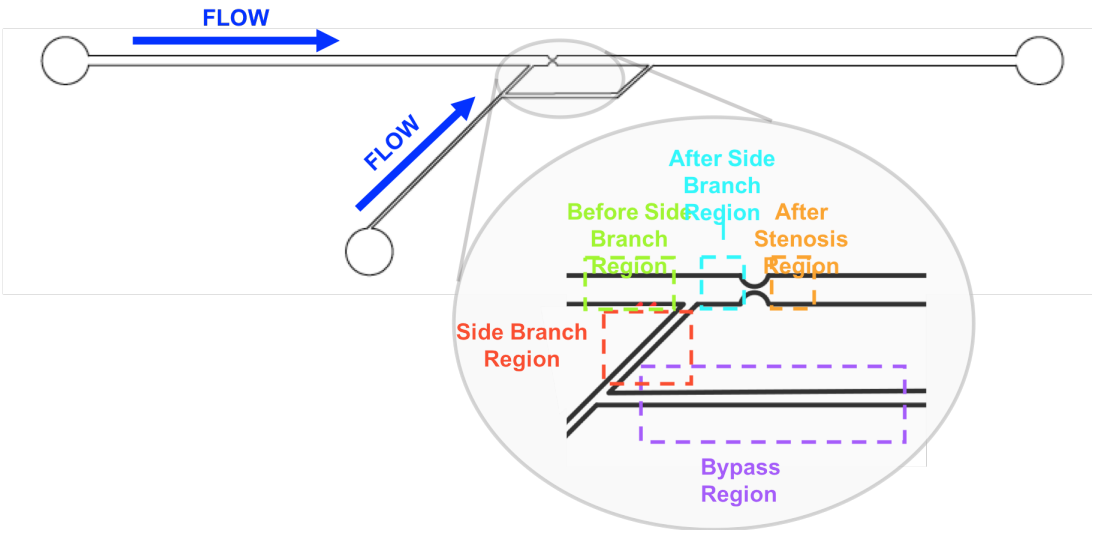

Figure 4.1: A CAD drawing of the bypass geometry with the three different positions of the W = 100 μm side branch. Blue arrows indicate flow from the syringe pumps

The first experiments are conducted using a syringe pump to control the velocities within the two channels. If the velocity in the side branch is lower than the main channel it is hypothesised that a bypass will occur. Depending on whether there is a full or partial bypass will dictate the velocity after the side branch (but before the stenosis). The use of a syringe pump will mean that the velocity in the side branch will be influenced by the width, the smaller the channel the higher the velocity. This is basic fluid dynamics. The pressure with in the channel is also linked to the velocity and width, therefore by altering the width of the channel will influence the pressure within the system. For the latter experiments, a pressure controller is used to control the pressure drop directly.

4.1.1 Influence of Position of Side Branch

As fore mentioned in the methods section 2.1.2, three positions were explored: 1600 μm, 600 μm and 300 μm away from the 80 % stenosis. The reason for focusing on 80 % stenosis is because this is the closest to *in vivo* case [32]. With increased stenosis there is an increased likelihood of a thrombus forming [10], however the presence of a side branch close to the stenosis reduces the occurrence of a thrombus [33]. By exploring different flow conditions

in both the side branch and the main channel it will be possible to discover which position of side branch is most probable of causing a bypass. In order to determine which flow rate is the most influential on causing a bypass to occur the flow rate (controlled by the syringe pump) in the side branch are altered 1-10 μL/min whilst the flow rate through the main channel is maintained at 10 μL/min as seen in figure 4.2 A and B. This is then switched in figure 4.2 so that the main channel is changing flow rates from 1-10 μL/min and the side branch is kept at a constant flow rate of 10 μL/min. The velocities can then be measured using GPV throughout the different regions highlighted in both figure 4.1 and 4.2. It should be noted that despite one of the channels having a constant flow rate at the inlet, all regions are effected by the changing flow rate at the other inlet. A greater overall influence on all regions seems to be more prevalent when the main channel flow rate is changing.

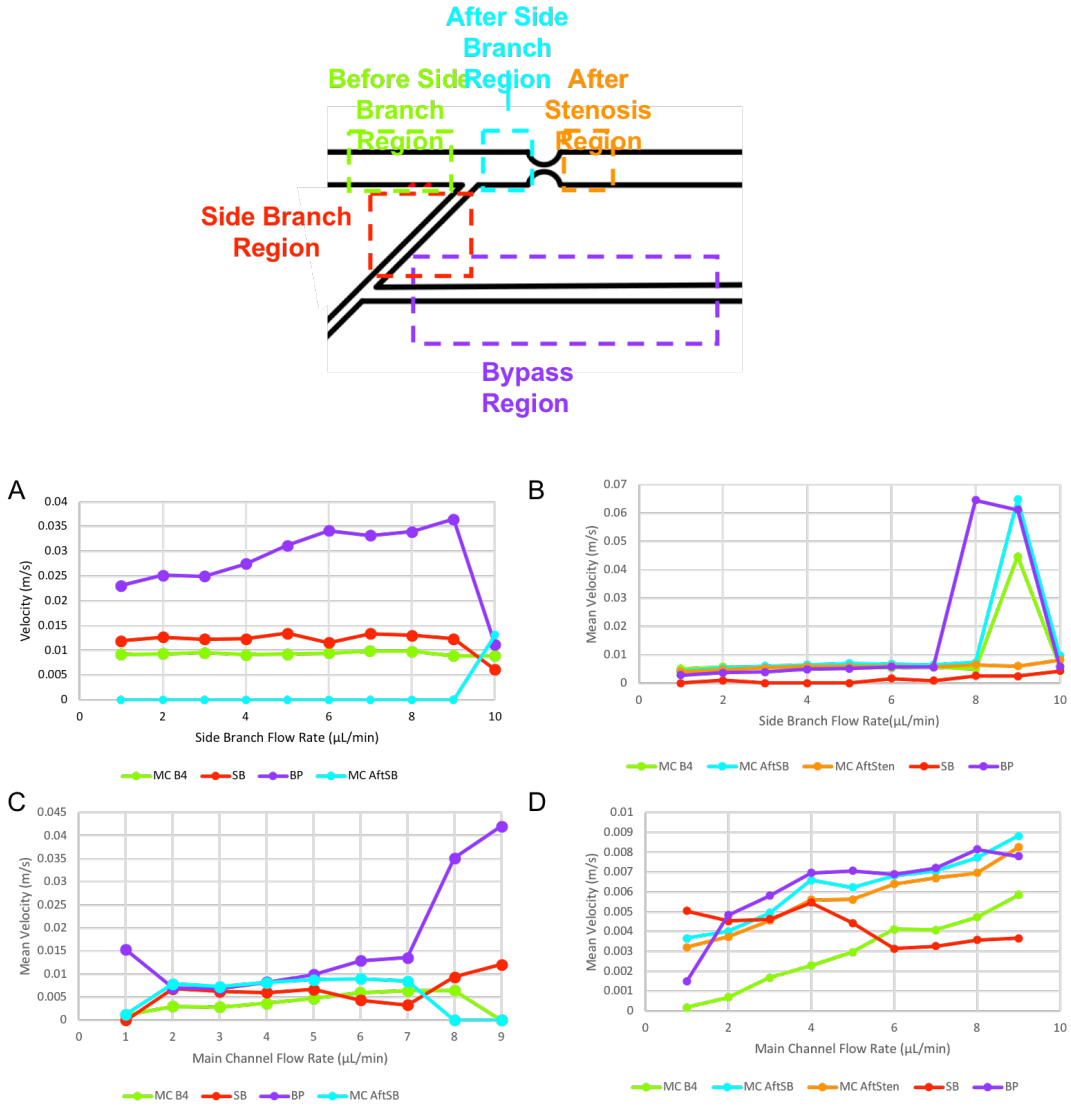

Figure 4.2: Four graphs demonstrating how the difference in side branch position directs flow through the bypass geometry. Regions highlighted about the graphs are selected and the mean velocity has been plotted. A and B shows the velocities in the different regions when the side branch flow rate is changed from 1-10 μL/min (x axis) and the main channel flow rate is set to 10 μL/min. C and D show the alternate condition, the main channel changes flow rate from 1-10 μL/min and the side branch flow rate is maintained at 10 μL/min. A and C are plots for side branch positioned 600 μm away from the stenosis and plots B and D show velocity plots for side branch positioned 300 μm away from the stenosis. Both side branches have a $W_{SB} = 200\mu m$.

Figure 4.2 A indicates that there is a full bypass occurring as the fluid is stagnant up until 9 μL/min. The main channel is maintaining a constant flow rate of 10 μL/min the velocity of the side branch is gradually increasing up until the flow rate in the side branch is 9 μL/min. At this point it seems like there is an equilibrium of pressure as the velocities all balanced out at a constant. By increasing the flow rate in the main channel the behaviour of the flow is the inverse. Instead of the bypass rapidly decreasing, the velocity rapidly increases when flow rate 7 μL/min and a full bypass is initiated as flow is 0 m/s at 8 μL/min. Flow has been redirected from the main channel before the side branch down through the bypass. The pressure through the bypass ($w = 100\mu m$) region is greater than in the main channel which will redirect the flow. As for position C (figure 4.2, B and C), there appears to be no bypass across all conditions. There is a constant stagnant region in the side branch when the side branch flow rate is changing, indicating that the velocities in the main channel and bypass regions are roughly the same, which can be seen in figure 4.2 B.

It should be noted that even if a full bypass does not always occur, there would be less fluid going towards the stenosis. In these cases 200 nm particles were used, which are stable in suspension. When there is a partial bypass, there is less particle suspension flowing towards the stenosis. Less particles means a reduced particle-particle interaction. Although no accumulation would be witnessed due to the size and concentration of the 200 μm particles, in an *in vivo* case, blood cells are much larger at a higher concentration. This means that if a full bypass is occuring there is a stagnant region before the stenosis. Stasis *in vivo* means there is an increased cell-cell interaction and blood is more likely to clot [15]. Alternatively if there is a partial bypass *in vivo* a thrombus is less likely to occur due to the reduced blood flow towards the stenosis. This would mean a reduced accumulation of cells at the stenosis. There would be constant flow through all the blood vessels. If the side branch is stagnant there is still fluid flowing around the stenosis in the smaller channels. If the main channel velocity is slower, then there is a stagnant region between the side branch and the stenosis. Stasis encourages clot formation which could be the reason why large, reproducible clots form when the main channel has a lowered velocity.

Finally, with the side branch least expected to have a bypass, position A, the results were as predicted [33]. Due to the stenosis being so far away, two videos had to be captured in order obtain the velocity profile throughout all the specified regions. In previous examples a bypass full/partial was observed when the flow rate in the side branch was 1 μL/min and 10 μL/min in the main channel. For position A this is not the case. The side branch, however was stagnant in these conditions. This is the first instance where the side branch remains stagnant whilst the bypass and main channel has flow. Raising the idea that, although it was originally thought that the thrombus initiates and propagates in the IVC, main channel in our case, it could start in the side branch and detach to move into the main channel. There are no studies to suggest this is not a possibility therefore more research would need to be carried. Inversely, when the flow rates are switched the all the regions have flow as seen in figure 4.3.

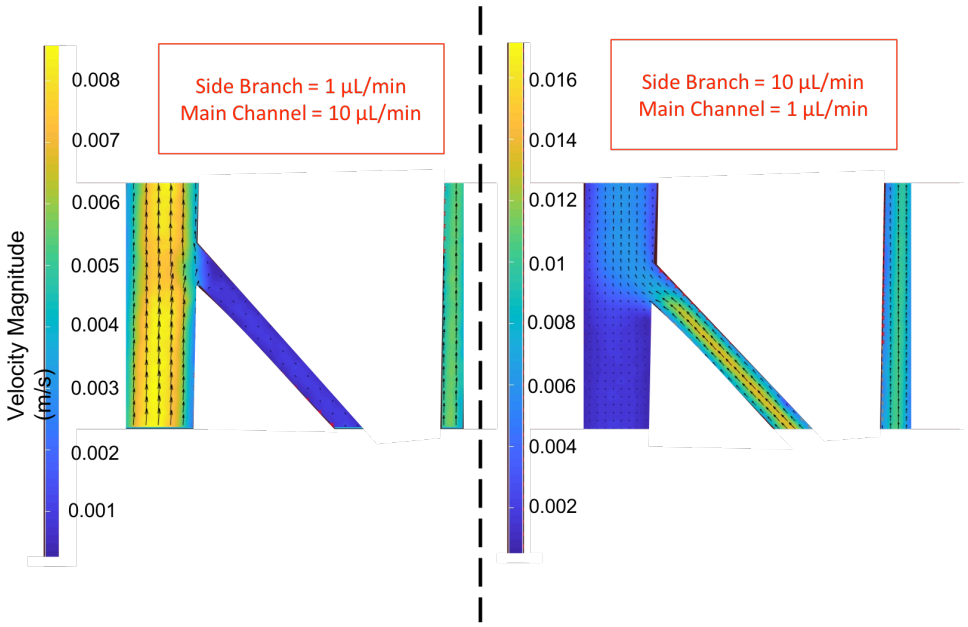

Figure 4.3: Velocity magnitude map of bypass design, positioned 1600 μm away from the stenosis with $W_{SB} = 100\mu L/min$

To conclude whether position of a side branch encourages the presence of a stagnant region, the answer is yes. Stasis before the stenosis is probably the region for a thrombus forming, not a recirculation of flow as suspected in literature [33]. Stagnant regions have

been proven to cause thrombosis within venous conditions [25]. It should be emphasised that 300 μm is a very short distance and when carrying out the operative procedure on the mouse would be very difficult to avoid damaging the vessel wall, where as 600 and 1600 μm are a lot more manageable. If damage did occur to the IVC of the mouse, the clot formation would occur similarly to that seen in arterial clot formation, exposure of the extracellular matrix [147].

4.1.2 Influence of Side Branch Width

The width of a side branch is important to whether a bypass with occur as although the flow rates applied from the syringe pump are the same the velocity is determined by the channel dimensions (equation 2.3). Previously, the results for side branch width 200 μm has been presented in figure 4.2. Throughout this section multiple plots and velocity profiles will be compared to aid in the determination of which factors are most important in creating a stagnant region within the channel. The data shown in figure 4.4 is particularly interesting because, when the side branch flow rate is lower than 9 μL/min there is no flow through the main channel and a complete bypass is occurring. In comparison to figure 4.2 B, the bypass does not transpire, the reason for this is the fact that the side branch is the same width of the main channel. When the side branch is 100 μm there is a full bypass, meaning that there is a stagnant region after the side branch but before the stenosis is where the thrombus is formed in the murine model [148]. The flow in the main channel before stenosis has the same behaviour as seen in figure 4.2 A and the bypass region is gradually increasing in velocity up until a rapid drop at the same point where the bypass stops.

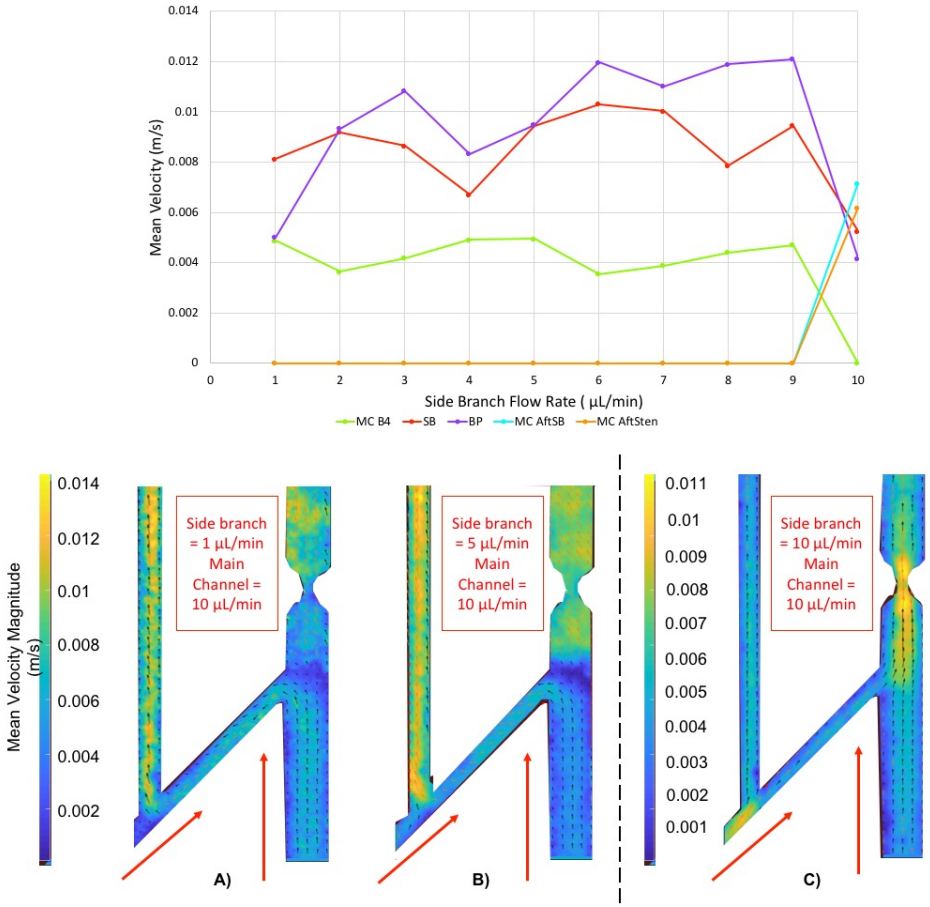

Figure 4.4: Data showing how the width of the side branch means that there is a stagnant region up until 9 μL/min. Degree of stenosis = 80 %, width of channel = 100 μm position C. Red arrows indicates the direction of flow.

The velocity profiles seen in figure 4.4 are the mean velocity profiles of the standard 100 frames. The orange arrows should be ignored as they are not representative of the true data seen in figure 4.4 A and B after the side branch. Even when using lower flow rates the disorder in this region suggests that there is no flow within this region after the side branch, before and after the stenosis. The flow is being redirected down the side branch into the bypass region. Furthermore, when the main channel is changing, the graph looks similar to the plot seen in figure 4.2 D. The side branch suddenly tails off at 5 μL/min when the side branch is 100 μm in figure 4.5 where as in figure 4.2 drops off at 4 μL/min before plateauing at 6 μL/min. Even when the side branch velocity starts to reduce the bypass region maintains a

steady increase in velocity. The similarity between these plots is probably due to the position of the side branch being the same.

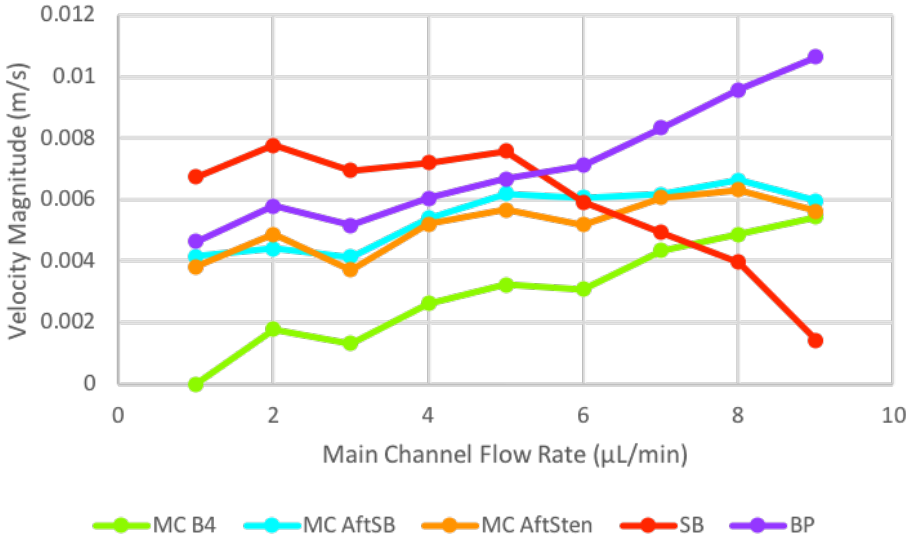

Figure 4.5: Data showing the how the velocity in the four regions changes as the side branch is kept at 10 μL/min and main channel increases, as seen by the red line. The width of the side branch is 100 μm

4.1.3 Influence of Degree of Stenosis

With a greater stenosis there is an increased pressure drop which would redirect the flow around the bypass instead of through the stenosis.

There are two ways to measure how the amount of stenosis influences the direction of flow within the bypass device. By using 80-50 % static stenosis it is possible to investigate the influence of flow as seen before in the previous sections. The second is by using a dynamic pump device as described in methods section 2.2.2. There are two channels with no outlet which were filled with ink (as seen previously in figure 2.14). A liquid need to be added into the pump geometries because if they are filled with air gas is pushed through the PDMS gap between the channel and the pump forcing air bubbles into the channel. Using the pressure controller to apply pressures from 0 - 2000 mBar it is possible to control the restriction in

the y direction by pushing the channel walls from either side causing a restriction. With increased pressure there is an increased restriction to the channel, similar to that seen in the stenosis model. Three devices were tried, the best for applying a stenosis was the geometry with the smaller pump design (L=500 μm). Therefore all the results collected from the pressure induced bypass is collected using this geometry, figure 4.6

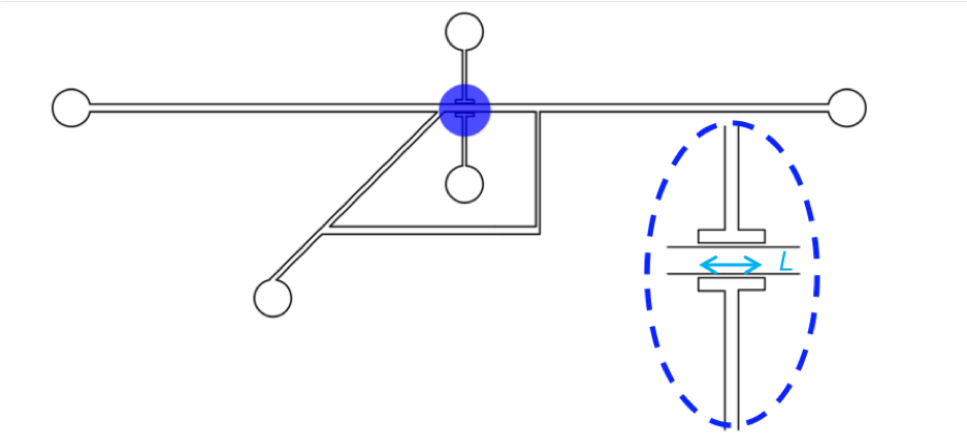

Figure 4.6: The CAD drawing of the devices used to apply a controlled stenosis in the main channel.

Flow rate Induced Bypass

All the data presented previously has an 80 % stenosis and will therefore not be presented again but will be discussed in this section. The 50 % stenosis has flow characteristics are more predictable than the previous results with the largest restriction of 80 %. In the case of 50 % stenosis the region before the side branch the velocity remains relatively stable, along with a slight increase in the velocity after the side branch and a rapid increase in side branch and bypass velocities (seen in figure 4.7). Most importantly, no bypass occurred in this scenario indicating that the amount of stenosis is crucial for a bypass. This is to be expected as it was also determined in the pig model that with a greater restriction there was a larger thrombus formed [10]. It is quite likely this is the same as for the murine model as the restriction applied is 80-90 % [32]. As for when the main channel is changing flow rate, the situation

is very different. There is a sudden change in flow in the side branch at 5 μL/min, half the flow rate in the side branch (10 μL/min). As mentioned previously the flow rate applied to the side branch has been constant throughout all the experiments, the degree of stenosis will induce an increased pressure through the stenosed region. This increase pressure in the stenosis will effect the velocity in the main channel, especially between the side branch and stenosis. This effect would be more prominent when the side branch is closer to the stenosis. In this case the side branch is also half the width of the main channel. Immediately after 5 μL/min the flow returns back to the side branch region of the device. It would seem that actually if the stenosis is at 50 % it has no effect on the flow regardless of the different flow rates through the side branch and main channel.

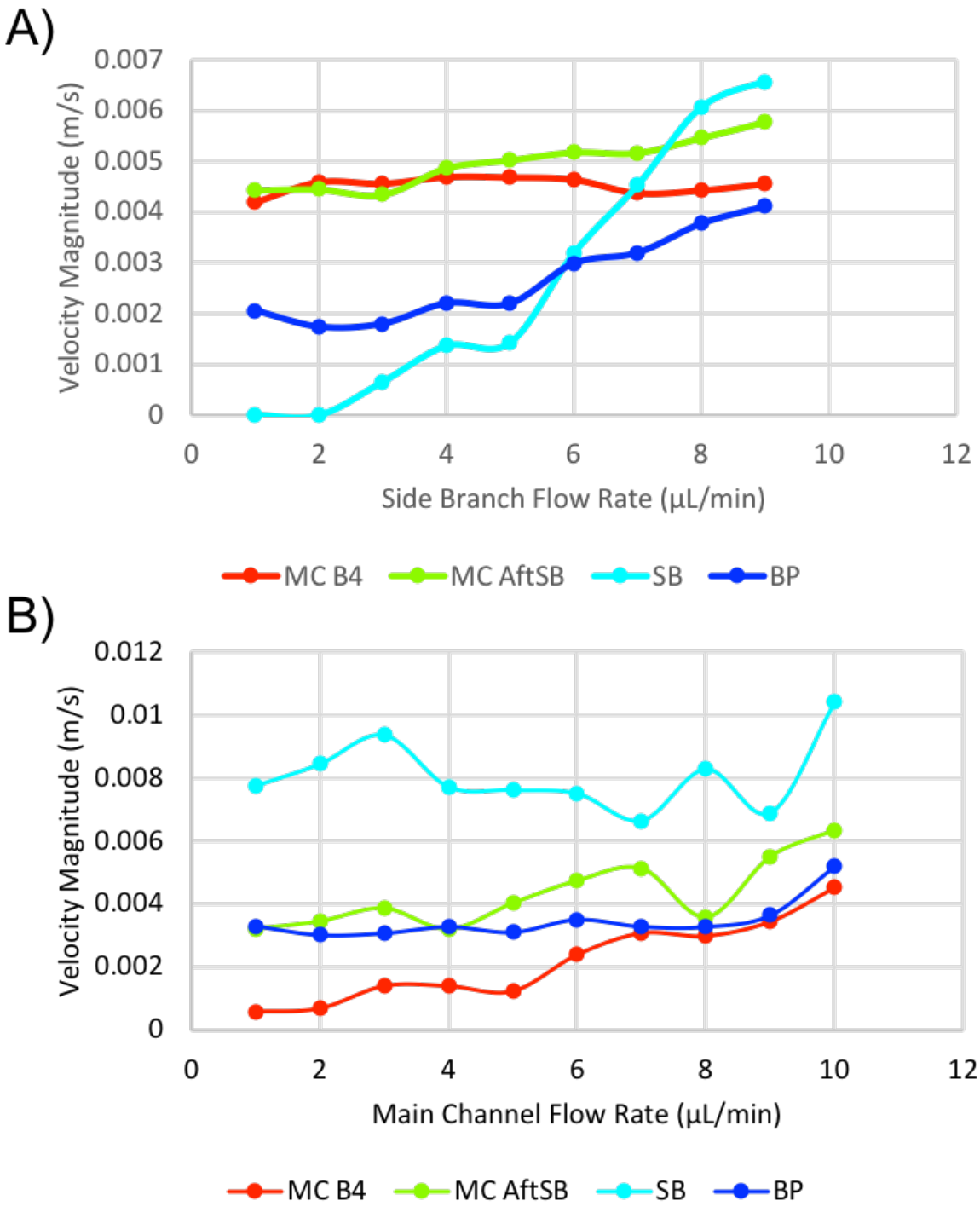

Figure 4.7: Plots for 50% stenosis and 100 μm side branch. A) plots the velocity for increasing side branch flow rate, and B) is for increasing main channel flow rate

With a 50% stenosis it was expected that a bypass would occur according to literature [146]. In the study from Hu et al., it was found that a pressure drop occurred with a stenosis

of 40 % and only from one side making it more of a step geometry. The edges where also 90° which is not typical of venous networks and the velocity was considerably lower than would be expected *in vivo*. In this model the edges are rounded as they would be *in vivo*, as well as having a less harsh angle of 45 °. Again, it is not known to where the thrombus is initiated *in vivo*.

At this point it would be right to assume that the greatest influence on whether a full bypass will occur is the flow rate of the side branch and the 80 % stenosis. In two cases:

1. Side branch position B, side branch width = 200 μm, **side branch flow rate changing, stenosis = 80**%
2. Side branch position C, side branch width = 100 μm, **side branch flow rate changing, stenosis = 80**%
3. Side branch position B, side branch width = 200 μm, main channel flow rate changing, **stenosis = 80** %

Pressure Induced Bypass

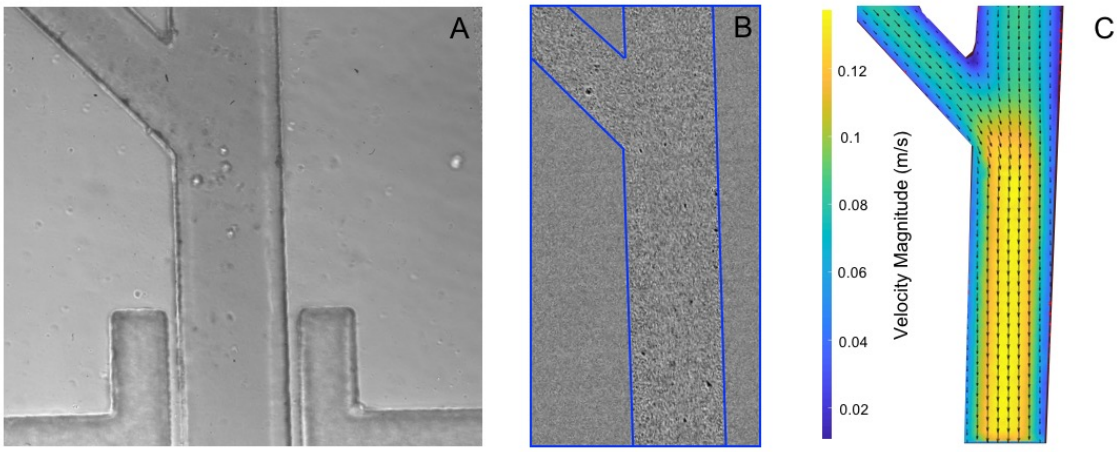

Figure 4.8: An indication of how the velocity was measured using GPV, with A) showing the bright field image of the device including the pump mechanisms, B) the GPV indicating the lack of signal within the pump systems and finally C) showing the velocity magnitude through the main channel and side branch.

As aforementioned the degree of stenosis influences the pressure drop within a vessel. The following results explore how the influence of a stenosis and velocity of the fluid impact the redirection of flow. It was established that the primary driving force that encourages a bypass to occur is a combination of the two parameters: stenosis and velocity. Therefore, in these next results smaller increments of stenosis are going to be investigated. Instead of using 50 and 80 %, it is possible to implement pumps on either side of the channel as described in methods section 2.2.2 to employ ≈ 10 μm increments of stenosis as seen in figure 4.9. Using smaller increments will allow for the determination of how restricted a murine blood vessel has to be in order to cause a bypass to occur. Figure 4.9 was collected by applying pressure to the pump geometries (which were filled with ink) from 0-2000 mBar. As the pressure is increased it causes the pump geometry to squash the main channel, thus causing a restriction. The degree of stenosis can be measured by considering the width of the main channel as be-

ing 100 % (W = 300 μm). Then at the different pressure the restricted part of the channel can be measured and divided by the original width and multiplied by 100 to get the percentage at which the restriction has implemented.

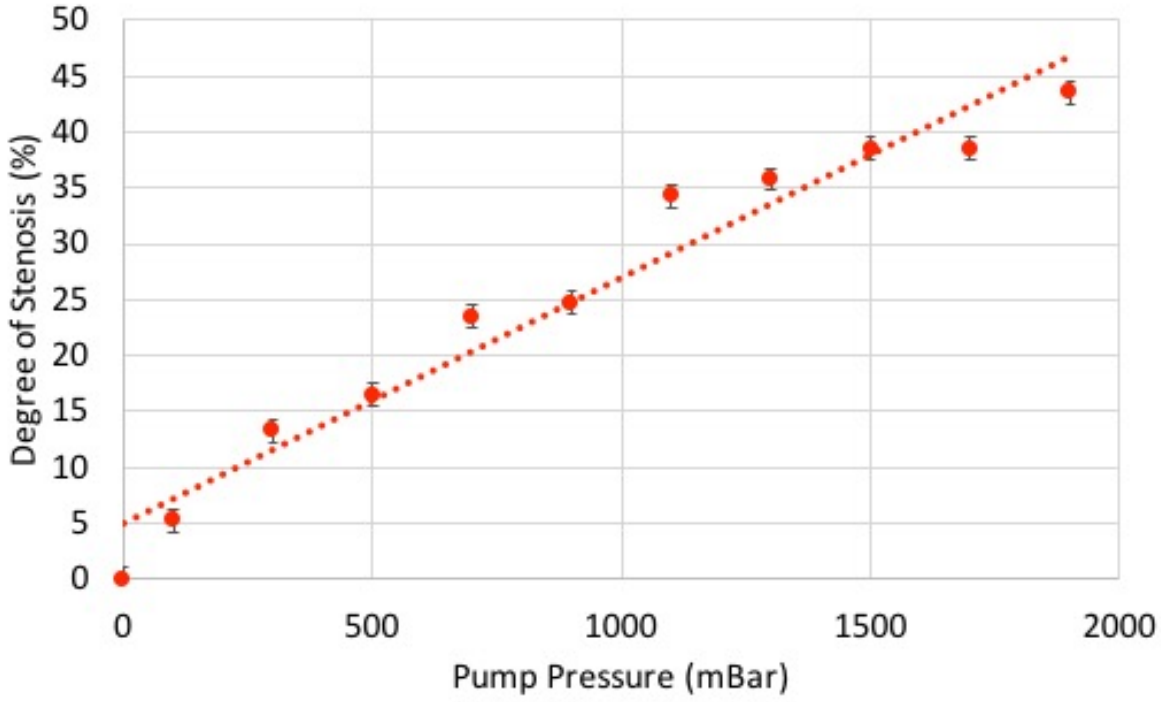

Figure 4.9: Linear correlation between increased pressure in the pump system and the degree of stenosis. Degree of stenosis is the percentage at change between the straight channel (300 μ) and the restriction induced by the external pumps. Error bars are the mean standard deviation of three different experiments using the pumps to restrict the channel. R^2 value = 0.95.

At maximum mBar the pressure controller could operate at (2 Bar) the amount of stenosis was only ≈50% (figure 4.9). As you can see from figure 4.10 the flow is not influenced with the increased stenosis. This is probably due to the stiffness of the PDMS. The stiffness of the PDMS can be altered by changing the ratio of the PDMS and curing agent [118]. The material properties of the PDMS changes drastically when the PDMS component is increased and the curing agent is kept the same, this is due to the reduced crosslinking between the polymers meaning the material is more flexible [118].

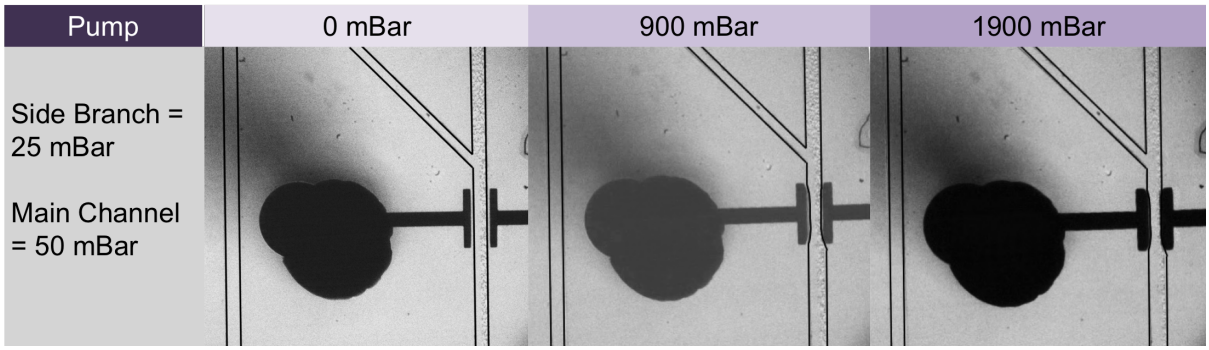

Figure 4.10: Three images indicating that even with 50 % stenosis no bypass occurs.

Two different sized particles were used through out the pressure controlled experiments 200 nm for GPV analysis and 3 μm particles to aid with visualisation of a potential full/partial bypass. The particles used to characterise the flow within the experimental parameters: main channel 70 mBar and side branch 40 mBar were 200 nm. However, with the use of larger particles it is possible to visualise a bypass more prominently (see figure 4.10). The bypass in 40/70 mBar case is partial and occurs at the maximum stenosis capable within this device, ≈50 %. Increased flexibility of the PDMS will allow for a larger stenosis. It would also aid in giving a higher resolution of data as it would be possible to use smaller increments. The large particles were generally added into the main channel only so it would be clear that a bypass would occur. When there is no stenosis, there is no bypass and the side branch is stagnant. Seen from previous experiments, the degree of stenosis is crucial for a bypass to happen. Therefore, if the stenosis was closer to the desired 80% a bypass would be more likely to occur according to previous results. This could also be more representative of the murine case *in vivo*.

As it was found that when the side branch flow uses lower flow rates, in order to recreate this situation and to encourage a bypass to occur the following parameters were used: the side branch pressure is 10 mBar and the main channel is 80 mBar. Large particles were used and it was found that the fluid flows backwards down the side branch. There was no difference in flow even when a stenosis was applied. Likewise if the pressure in the main channel is 10 mBar and the side branch is increased to 50 mBar there is back flow down the main

channel.

Another interesting occurrence is the build up of nanoparticles seen on the corner between the side branch and the main channel. In literature this has been highlighted to be a phenomenon of shear [149]. It has been suggested that the angle of the side branch can encourage/discourage platelet activation and ultimately aggregation. The fact accumulation still occurs without the presence of biological factors (proteins, cell signalling) suggests that the aggregation is driven by the physics of the fluid flow. This suggests that the thrombus could form in the side branch and get trapped and propagate in the main channel, or IVC *in vivo*.

All scenario's demonstrated that although the different geometric influences flow the main contribution to a full bypass arising was having a lower flow rate in the side branch. However, it is definitely a contribution of flow conditions and geometric parameters cause the full bypass as it does not occur in all instances. Another region which appears to cause particle accumulation and can be stagnant is the side branch. The potential of the thrombus being initiated somewhere else and getting trapped at the stenosis does not seem to have been considered. Yet this model has highlighted that it could be a possibility.

CHAPTER 5

VALVE MODEL

The valve model allows for a more *in vivo* relevant understanding of deep vein thrombosis. By advancing from the stenosis model it is possible to observe complex flow patterns around flexible valves. As highlighted previously there are many drawbacks with the stenosis model ia that enforcing a restriction forces thrombosis to occur. The restriction increases the number of cell-to-cell interactions increasing the likelihood of thrombus formation, thus making it a less desirable approach for investigating the physical mechanisms behind DVT. By introducing passive valves which open and close as a result of flow does not force thrombosis to occur, as this is the mechanism at which venous valves function *in vivo*. Therefore, this novel combination of micro-fabrication methods and flow visualisation allow for the investigation of how flow patterns can change around passive valves depending on the stiffness and geometry [122]. Stiffness of valves could be an initiator for thrombus formation and is thoroughly investigated through out this chapter.

5.1 Results and Discussion

5.1.1 Successful fabrication of flexible Valves

The *in situ* fabrication of valves had to be standardised to ensure the reproducibility of physical and geometric properties. Initially there were minor complications following the method

stated in literature[120], this was because in order to get the flexible valve the base of the microfluidic device had to be spin coated with PDMS. This is because PEGDA does not cure in the presence of oxygen. By spin coating the glass slide with PEGDA it allows oxygen to permeate into the channel, thus allowing for a small gap between the top and bottom of the valve in order to allow it to move when flow is added. However, the spin coating process was consistent, there was slight variability with the PDMS layer on the glass slide. This was probably caused by the varying temperature in the laboratory altering the viscosity of the PDMS as increased heat will decrease the viscosity resulting in a thinner layer of PDMS on the glass slide. It was found that in order to remain constant throughout the methodology, the projection of the valve needed to be aligned with the bottom of the channel. This approach worked for all devices.

It was evident early on that the anchor geometry was substantially better than the pillared device at securing the PEGDA hydrogel in place (geometries are shown in section 2.1.3, figure 2.5). For this reason the anchor geometry will be used for future experiments. Another way to increase the stability of the anchored valve is to double expose the anchor section of the valve to increase the stiffness of the hydrogel thus increasing the stability of the valve. Even with low concentrations of PEGDA and PI the valves rarely detached from their anchored positions. The use of PEGDA is important as it is biocompatible, it has been used in many tissue engineering and biomedical applications [150, 151] including specifically tissue engineered heart valves [152]. Biocompatibility is important for the prospective future *in vitro* developments.

Once the valves are fabricated it was then possible to characterise them *in situ*. In order to do this water was pumped through the device at a constant flow rate causing the valves to open. With increased flow rate there is increased deflection of the valve. Using small deflection it is then possible to calculate the Young's modulus using equation 2.1. It was hypothesised the valve properties will influence the flow and could lead to a better understanding of how thrombus formation occurs within the deep veins. In order to investigate this thoroughly two flow conditions were carried out:

1. Continuous Flow = To characterise the simple valve and look at flow patterns through and around the leaflet valves

2. Pulsed Flow = To look at complex flow patterns (forward and back flow) as well as particle accumulation

Both these conditions are discussed in great detail within this chapter. Obviously pulsed flow is more comparable with DVT as the skeletal muscle pumps push blood back to the heart in a pulsed manner. The pulse is not going to be as regular as the cardiac muscle and is dependent on the mobility of the person. However, it should be highlighted that DVT is more likely to occur in immobile patients. Immobility means that the muscle pumps may not be working as well as they should to pump the blood back to the heart and that the valves will not be opening and closing in the same way as they should. In fact the valves could be partially open thus causing a slow but continuous flow through the valves. Therefore, a continuous flow regime is also explored.

5.2 Characterisation of Valve Stiffness

In order to characterise the valve stiffness, the straight valve, may also be referred to as simple geometry, was used and the deflection was measured as in figure 5.1, similar to Wexler et al. In this case, however, there are two structures within the channel compared to the solitary hydrogel valve in Wexler's methodology. However, due to laminar flow the effect of two valves within in the microfluidic channel should have little effect on the calculation of the Young's modulus due to the Poiseuille flow giving a symmetric force on each of the valves. For this calculation to be reliable, h needs to be greater than the width of the base of the valve as stated in the Wexler et al., [122]. The dimensions of the straight valve has a base of 25.5 $\pm 1.6 \mu m$ and a general height of 121.75 $\pm 3.6 \mu m$, which is roughly the same as Wexler et al as there are two valves within the channel h is slightly shorter.

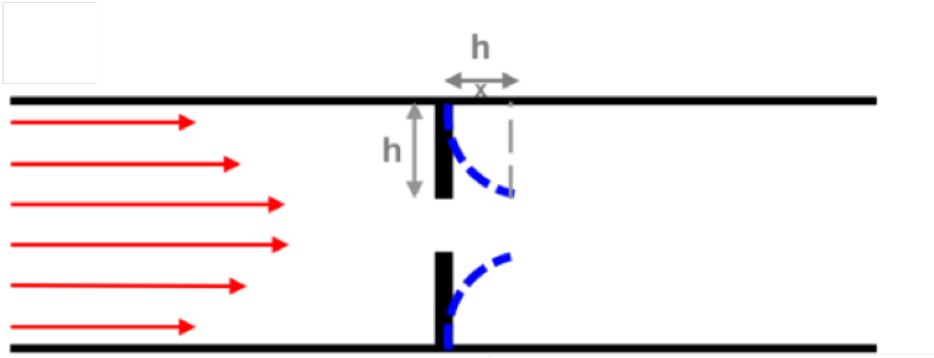

Figure 5.1: A simple schematic illustrating how the deflection was measured in the simple valves. The red arrows represent flow.

5.2.1 Varying concentration of Photo-initiator

It was found that with concentrations of PI (2, 4, 6, 8 % v/v/) the minimum exposure time varied. Exposure time is to be expected to vary as the PI will degrade over time and because only a small amount was being used (2-8 μL) at a time the volume of PI remains high yet the quality decreases. The stiffness also increased with increasing concentration of PI, again, this is to be expected as with increased concentration of PI there will be an increased number of cross links between the PEGDA and PI [153].

It has already been established in previous research that concentrations of PI alter the stiffness of valves in confinement. For this reason the changing of PI was used as a proof of principle and does not require extensive research experimentally as this has been carried out by Wexler et al. The increased concentration of PI will increase the amount of cross-linking between the PEGDA polymers making the structure, in this case a valve, stiffer and ultimately giving it a higher Young's Modulus, *E*. *E* can be calculated from the deflection of the simple valve using equation 1.2 and is shown in section 5.2.3.

In figure 5.2 the concentration of PI influences the amount of deflection. With greater deflection, there is more flexibility within the valve, thus indicating a less stiff material. The amount of deflection can then aid in the calculation of the Young's modulus, *E*, as seen in equation 2.1. To apply a curve of best fit to the graphs Matlab Curve Fitting Toolbox was

used to employ a power 2 curve with the equation $f(x) = a * x^b + c$ for each concentration of PI the following coefficients were used (5.1).

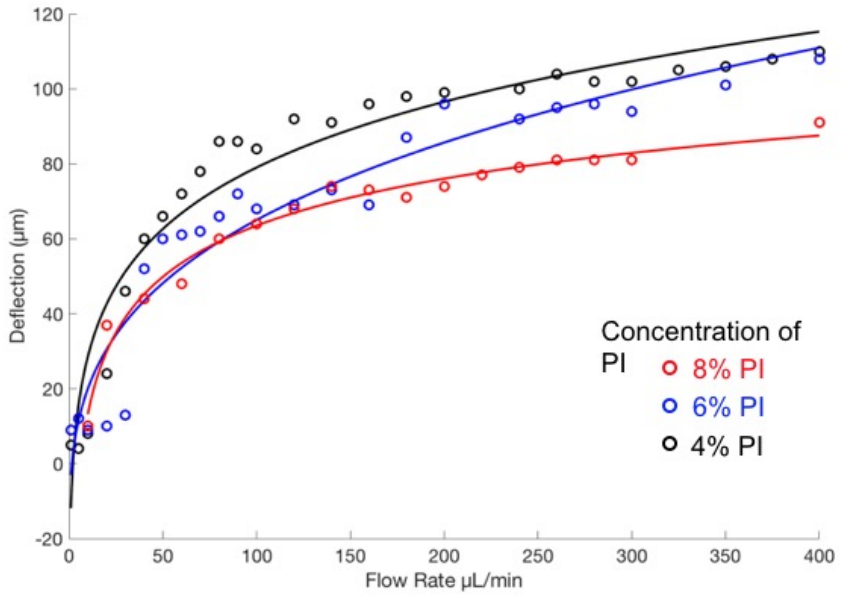

Figure 5.2: A graph to present how the concentration of PI alters the amount of deflection depending on concentration of PI. The lines are fitted via the following equation $f(x) = a * x^b + c$.

Table 5.1: Coefficients used in the power 2 fitting in 5.2

PI (% v/v)	a	b	c
8	-269.1	-0.1245	215.2
6	23.95	0.2922	-26.95
4	162.4	0.09651	-174.3

5.2.2 Varying exposure time

The minimum exposure time required to cross link the hydrogel structures is independent to the concentration of PEGDA and PI. It is possible to use 300 ms for 4 % PI with all the concentrations of PEGDA (30-100 %), which is also consistent with literature findings[122]. During the fabrication process it was clear to determine when over exposure had occurred.

Due to the nature of the experimental set up and use of acetate sheet photo-mask, there is the possibility that light can 'bleed' through the mask causing a skirt-like polymerisation to occur around the geometry (see figure 5.3).

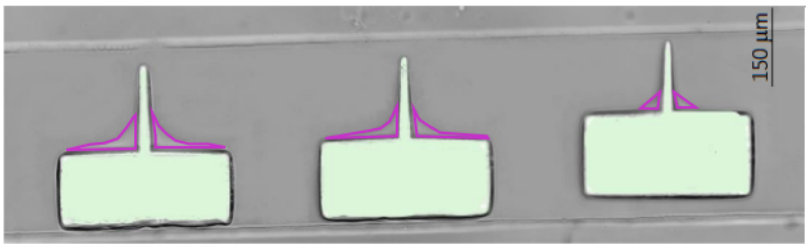

Figure 5.3: A bright field image of the simple valve with the 'skirt' highlighted in pink reducing with shorter exposure times.

In order to prevent over exposure it is possible to manipulate the light intensity and exposure time. In all cases minimum exposure time was used, and to establish this multiple exposures was systematically worked through until the valve geometry was not polymerised. Another factor to consider is that during storage the PI degrades over time which may mean that a higher exposure time is required in order to polymerise the PEGDA. Once valves were fabricated it is possible to briefly investigate how exposure time influenced deflection of the valve and in turn, *E*. It should also be noted that valves were fabricated and used the following day.

It was found that the exposure time increased the stiffness of the valve, which is supported by that seen in the study by Wexler et al., confirming that the procedure is consistent with literature. The graph shows at concentration 40 % (v/v) PEGDA and PI 4 % v/v at and different exposure times, 300 and 325 ms (figure 5.4 and coefficients for the fitting are presented in table 5.2).

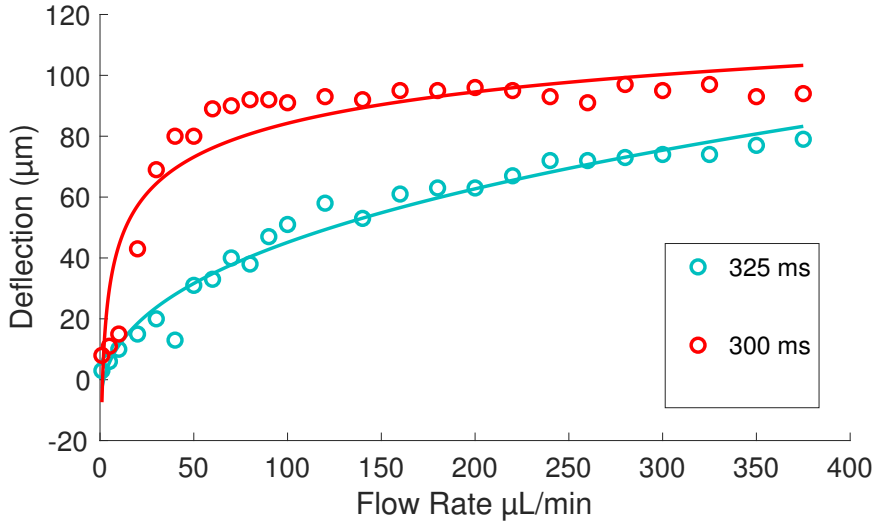

Figure 5.4: A graph showing how exposure time influences the degree of deflection within the microfluidic device. Red points are for 300 ms exposure and blue is for 325 ms exposure

Table 5.2: Coefficients used in power 2 fitting for figure 5.4

Exposure (ms)	a	b	c
300	-237.3	-0.106	229.9
325	9.927	0.3829	-12.78

As exposure time has been sufficiently researched in literature and the results were consistent with previous studies, it seemed appropriate to move onto varying concentrations of PEGDA, an area of research that is not yet been explored in a microfluidic environment.

5.2.3 Varying concentration of PEGDA

Exposure time and PI have been investigated previously by Wexler et al. [122]. It would seem that no one has used this technique to determine how concentrations of PEGDA influence the Young's modulus. It has previously been found in macro environments that PEGDA concentration influences the mechanical properties [154, 155]. However, for completeness of this model and in order to ensure the same relationship is observed, this microfluidic system is the same as that witnessed in the macro-scale experiments. The following results

show that with increasing concentrations of PEGDA there is a reduced deflection (figure 5.5 - coefficients for these graphs are presented in table 5.3), corresponding to literature.

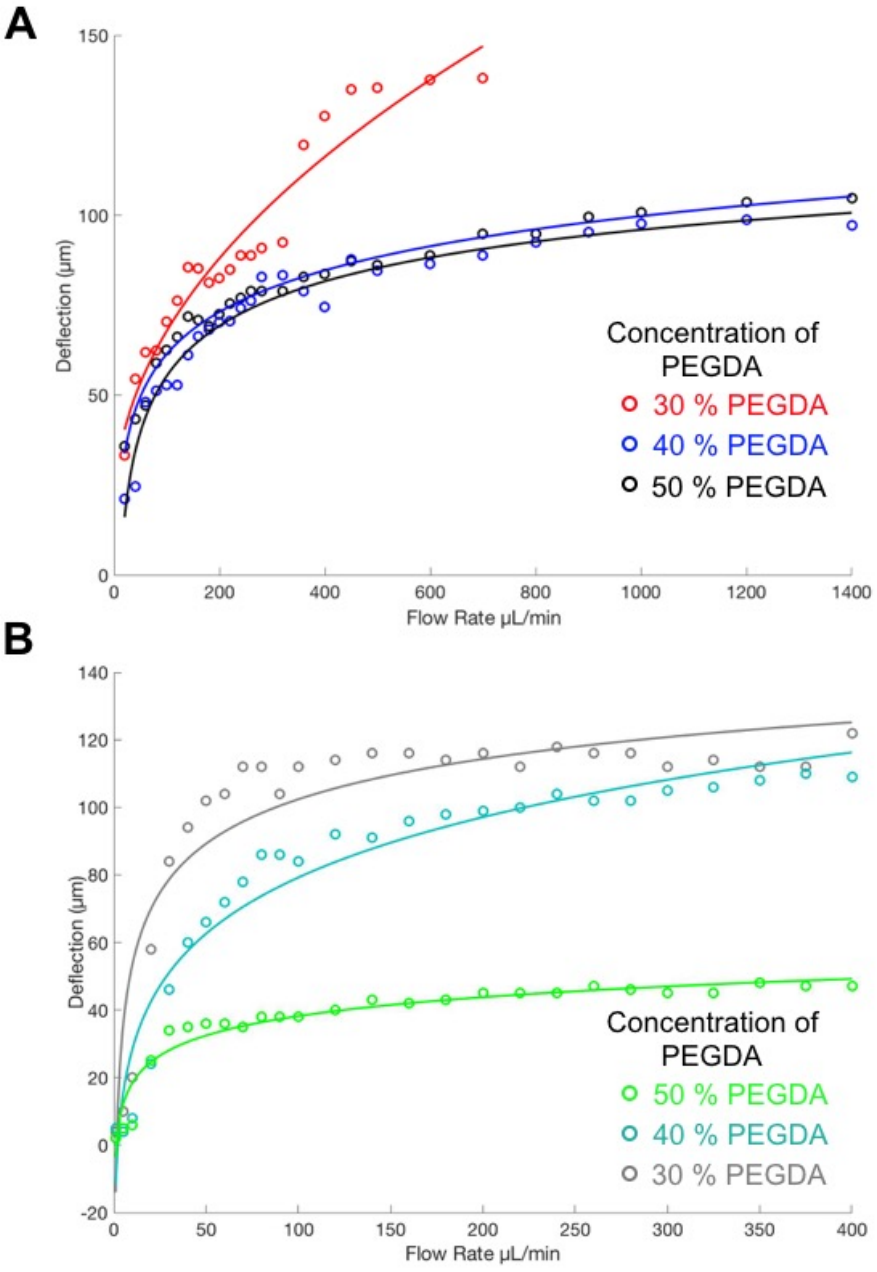

Figure 5.5: Both graphs show the deflection in response to flow rate with different concentrations of PEGDA. A) is the deflection for 8 % PI and B) is the defection for 4 % PI.

Table 5.3: Coefficients used in power 2 fitting for figure 5.5

PI (%) v/v	PEGDA (%) v/v	a	b	c	Plot
8	30	5.558	0.4813	16.89	A
8	40	-1072	-0.01713	1053	A
8	50	-274.4	-0.1679	182	A
4	30	-246.8	-0.1386	232.8	B
4	40	-120.7	-0.2217	125.8	B
4	50	-228	-0.04393	224	B

What is interesting about these results is that there is a larger range of deflection with 4 % PI, this is probably because of the amount of cross-linking between the PI and PEGDA. It is suggested in literature that with increased concentration of PEGDA and PI there is reduced pore size[151]. The reduction in pore size will also increase the stiffness of the valve. Another point to be made about all the above graphs is the trend is always the same, with a sharp change in deflection at the lower flow rates and then plateauing off when the simple valve is reaching it's maximum deflection. The shape of the deflection is to be expected as when the material approaches its maximum strain the valve will resist deflection irrelevant of the addition of force, hence the plateau. It is the first linear section that is used for the calculation of the Young's Modulus as this is referred to as small deflection.

5.2.4 Young Modulus Results

As mentioned previously the deflection can be used to calculate the Young's Modulus, E. The next graph illustrates the region of the graph used, linear section, referred to as small deflection, u. Tunable stiffness of the valves is a desirable quality within this model as the stiffness of valves *in vivo* increases with age [29]. It has not yet been thoroughly investigated how valve stiffness and DVT could be linked, however with this model it is possible to determine how the flexibility of valves influences flow; an important parameter when understanding thrombus formation. The higher E is the more stiff the material, which is represented in graph 5.6.

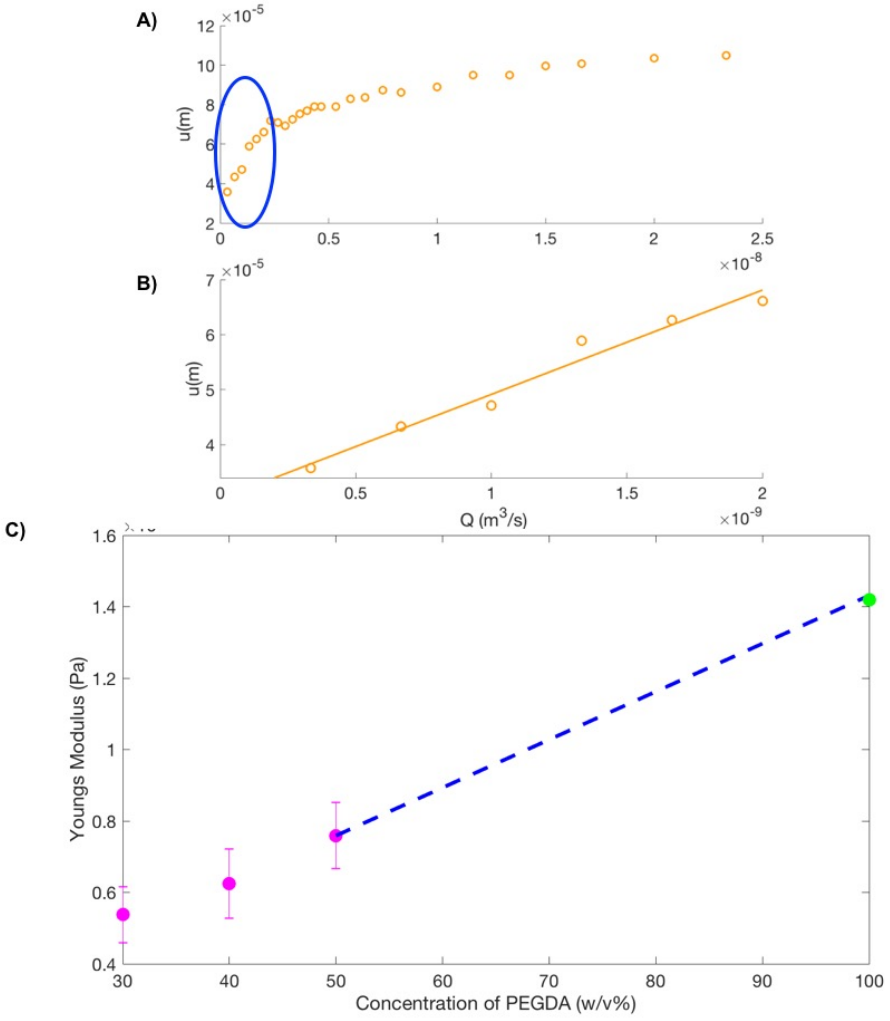

Figure 5.6: The above figure represents data collected from 8% v/v PI A) shows a typical graph of deflection against volumetric flow rate with B) highlighting the linear region, small deflection region used for the calculation of E shown in graph C). The green data point represents the maximum E for PEGDA 575

Note that there is a linear extrapolation (light blue dashed line) to 100% (v/v) PEGDA giving the maximum reading of 142 kPa which is the maximum Young's modulus for PEGDA 575 (one monomer chain between two cross-links) according to equation 2.1 [122].

$$E = \frac{3\rho RT}{M_w} \tag{5.1}$$

Where R is the ideal gas constant, T is the temperature, ρ is the density and M_w is the molec-

ular weight of 575 g/mol. This result (figure 5.6) suggests that optimum amount of PI is 8 % to obtain maximum amount of cross linking between the polymer chains and would make sense according to the deflection data seen in figure 5.5. To further investigate whether the trend is true across concentrations of PEGDA and PI, table 5.4 highlights and re-iterates that what has already been seen in literature [122]. Table 5.4 highlights the general increase in E depending on concentration of PEGDA and PI, represented by the colours green (low) - red (high). The standard error is also presented within this table. This indicates the ability to tune valve stiffness by varying concentration of PEGDA and PI as exposure time is relatively unreliable due to the denaturing of the PI over time. For these valves the lowest possible exposure time was used in order to ensure reproducibility of the material properties.

Table 5.4: Table displaying E for various concentrations of PI and PEGDA. The varying colour of the E column symbolises maximum E (red) and minimum E (green)

PI Concentration (% v/v)	PEGDA Concentration (% v/v)	E (Pa)
4	30	22203 ± 7021
	40	28361 ± 8969
	50	63352± 20034
6	40	53100 ± 16800
	50	83700 ± 26500
8	30	71100 ± 20500
	40	82100 ± 23600
	50	92600 ± 26700

The stiffness of valves could be a key parameter for developing DVT and for this reason it would be important to be able to quantify this *in situ* by ultra sound images. As is, this model uses straight valves to characterise E, however this could be developed numerically to take into account the curvature of the valve and would be something to consider for future work. It is also possible to visualise flow using ultra sound doppler, flow in the veins will be influenced by the skeletal muscles pumping blood as well as the efficiency of the valves to prevent back flow. Therefore characterisation of the flow patterns around valves according to the stiffness of the valves was carried out.

5.3 Flow Patterns Around the Valves

The efficiency of a valve can be depicted by its ability to empty the stagnant region behind the valve as well as close sufficiently to prevent back flow [156, 157]. Parameters affecting valve efficiency would be geometry and material properties, e.g. stiffness. The valves within veins are often referred to as leaflet valves, as they open like a leaflet towards the wall of the vessel [158]. For this reason, to better mimic the *in vivo* conditions, a leaflet valve is fabricated as mentioned in the materials and method chapter (sections 2.1.3 and 2.2.1). First of all, it should be noted that the change in geometry meant that there was a difference in flow around the valves (see figure 5.7). It can be seen that there is a much larger stagnant region behind the leaflet valve, which is more representative to the *in vivo* case. Flow between the valves is greater than that before, after and behind the valve, therefore multiple fps need to be used to capture accurate GPV, similarly to what was seen in the stenosis model, this can be seen from figure 5.7 and figure A.2, 60 μL/min (Re= 5). A higher fps is needed to record the flow through the centre of the valve in comparison to a lower fps for the rest of the device. Also to double check the stagnant region behind the valve slower fps were used to establish whether or not the valve pocket was stagnant (figure A.2).

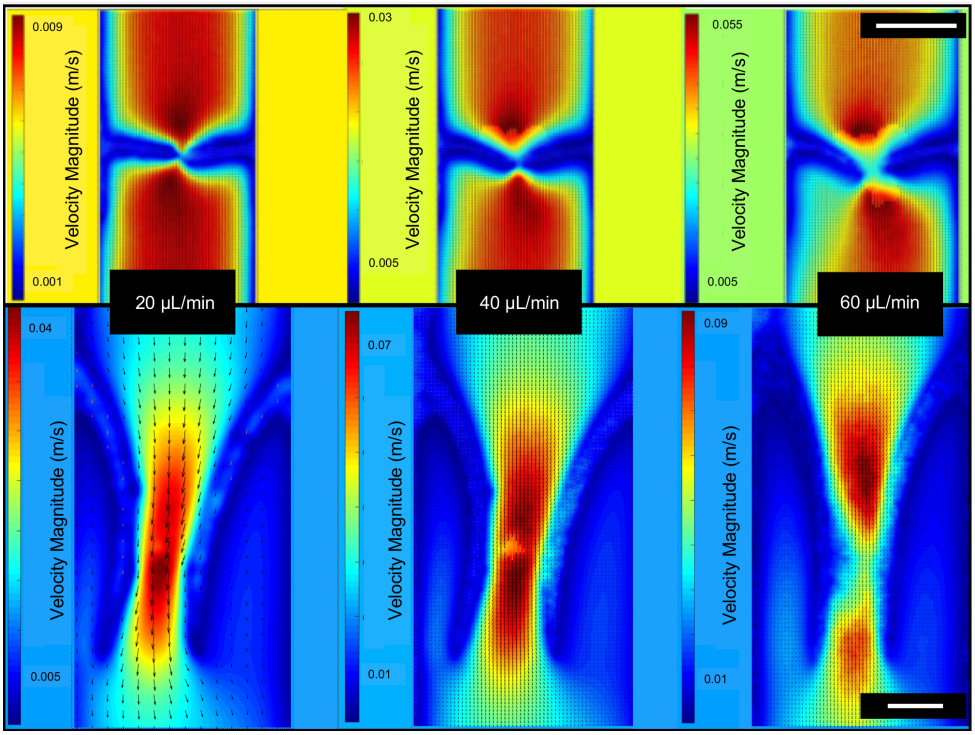

Figure 5.7: Velocity profile maps showing the difference in flow fields around the valves. No masking was used, yet valves are still visible as no flow regions. Straight valve scale bar = 150 μm (top three images) and the leaflet valve scale bar = 75 μm (bottom three images). *Re* = 2, 3, 5 respectively.

At higher flow rates vortices occur at the valve tips and the geometry of the stagnant region behind leaflet valve is considerably bigger compared to the simple geometry. Using GPV it was possible to obtain detailed flow profiles. Venous flow is highly variable hence a range of flow rates (1-900 μL/min) and elasticity of valves (see table 5.1) have been explored.

It was already known that with increased velocity the valve becomes more open, however using GPV it also revealed complex flow patterns occurring around the valves at higher flow rates. Vortices occurred at the valve tips. It can be seen in figure 5.8 that as *Re* number increases so does the size of the vortex. It is further demonstrated in figure 5.9 the linear relationship between *Re* and vortex area. It is evident that re-circulation zones initiate thrombus formation and the greater the re-circulation zone, the larger the thrombus [159].

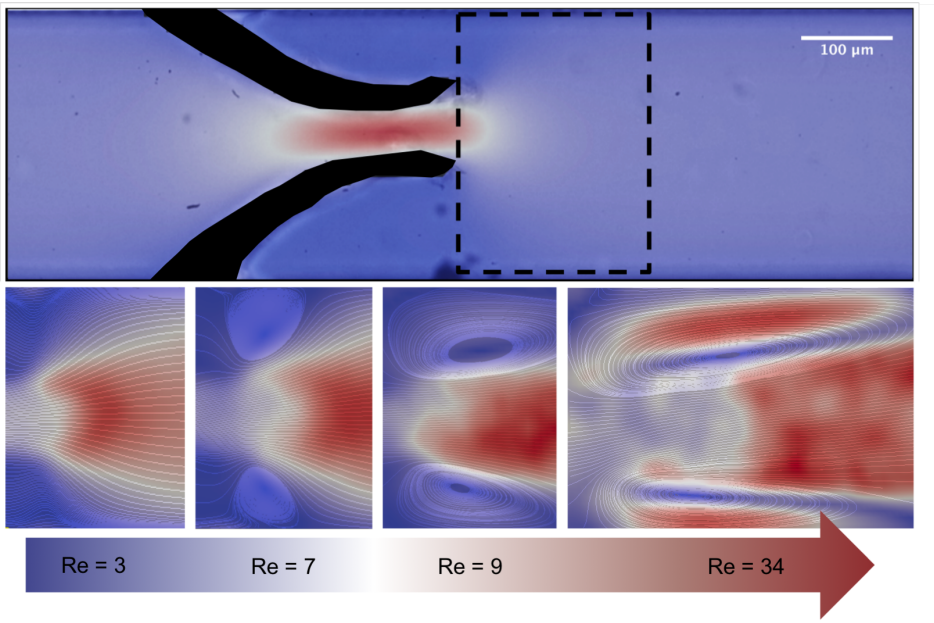

Figure 5.8: A velocity map and streamlines highlighting how as Re increases the size of the vortex also increases. The valve properties are 2 % w/v [PI] and 40 % w/v [PEGDA]).

Not only did the vortex increase in size, the tangent velocity also increased. PIVlab uses Kutta-Joukowski theorem to calculate the recirculation of flow [125]. The circulation has the units m^2/s and is measured by integrating vorticity over the area of the centre of the vortex [125]. The integrals are then calculated for a series of circles. Then by taking the maximum value for the tangent velocity for the largest 'circle' (outer most loop in the vortex), it can be plotted in multiple ways, as function of deflection (figure 5.11) as well as flow rate (figure5.9).

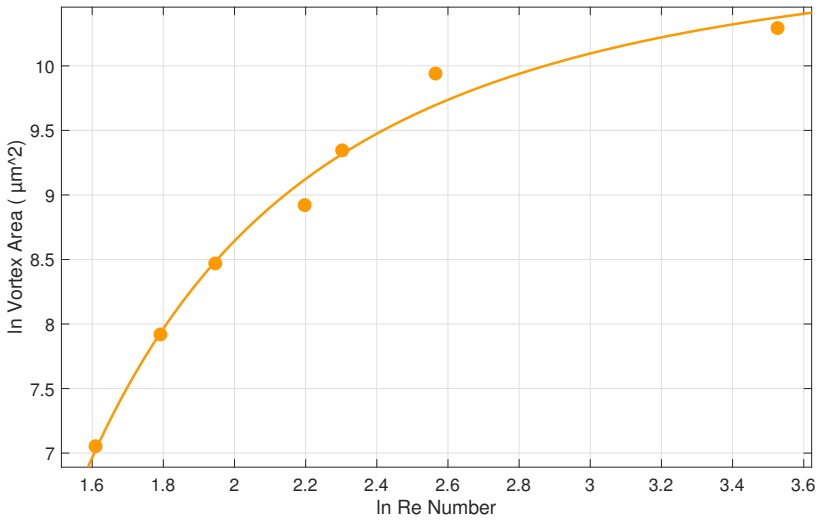

Figure 5.9: A representation of how vortex area increases with Re. Points are natural log (ln) of both Vortex area and Re number. $R^2 = 0.99$. $f(x) = -12.61 * x^{-2.45} + 10.95$.

As to be expected as vortex area increases so does the tangent velocity, which in turn is also linked to *Re* number. Even though it is shown that a vortex occurs behind the valve when it opens and closes, flow patterns themselves have been relatively disregarded when it comes to their influence of thrombus formation in veins. Yet as mentioned previously, recirculation is important for platelet activation and shown with in figure 5.10 is the influence of *Re* on the recirculation both in size and velocity. It should be noted this is not ignored in arterial and cardiac investigations.

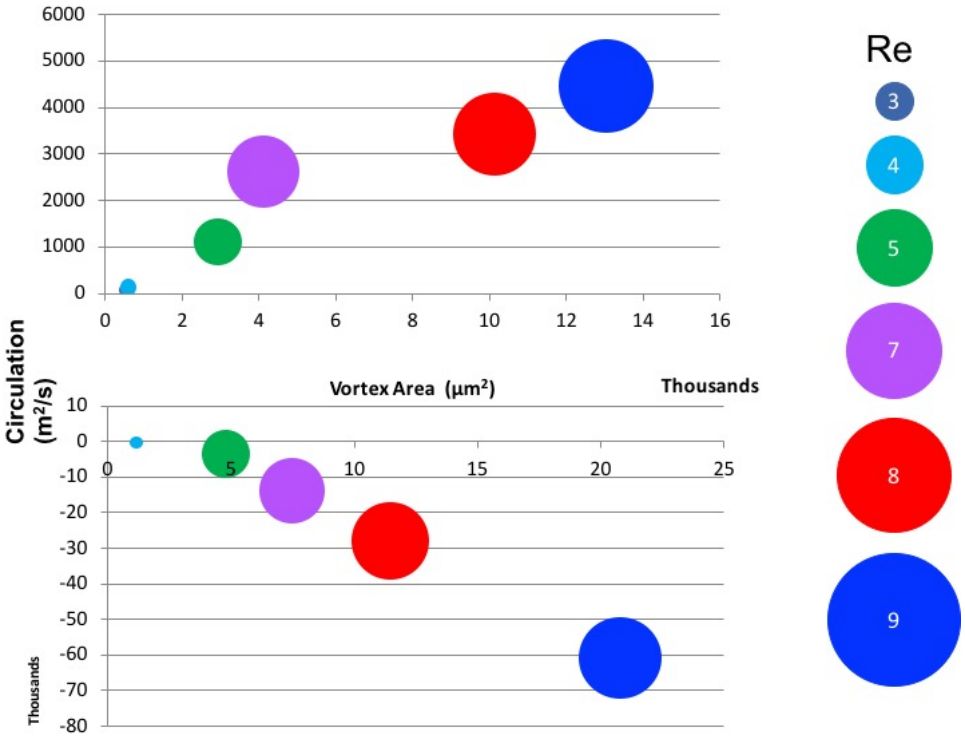

Figure 5.10: Following on from graph 5.9 this plot adds a third dimension to the data indicating the relationship between Re, vortex area and the tangent velocity is linear.

To mimic a 'healthy' vein, the most flexible valve ($E = 22.2 \pm 7$ kPa) was used. This valve opens to its maximum extent at the highest flow rate emptying the stagnant pocket behind the valve. On the other hand, with a stiffer valve, an increased stagnant region and, consequently, a higher residence time of fluid behind the valve is detected. This is representative of elderly people where the valve tissue becomes less flexible due to an increase of fibrotic tissue [160]. The increased stiffness also results in larger vortex occurring at the tip of the valve (figure 5.11).

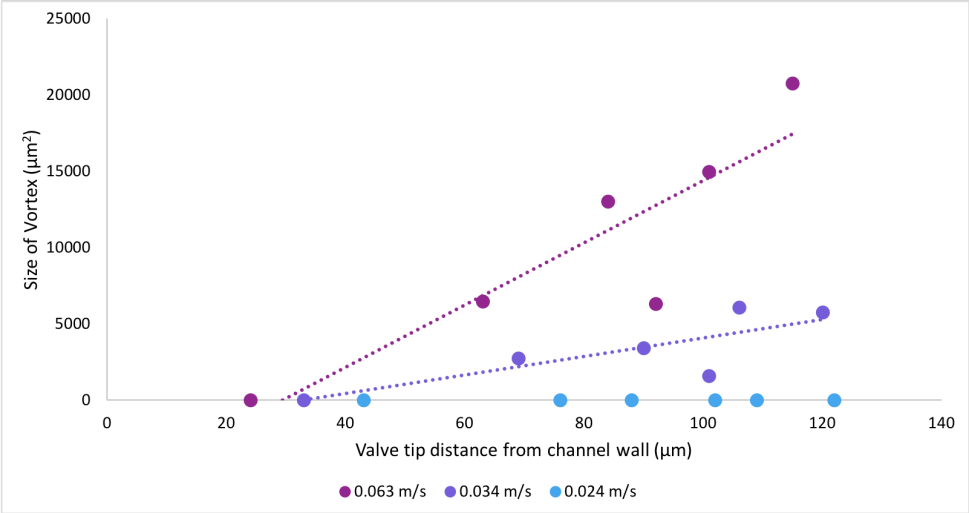

Figure 5.11: A graph to present how the amount of deflection influences the size of the vortex at different velocities.

It was discovered that when the velocity was lower than 0.024 m/s a vortex does not occur. This is a result of the fact that the velocity between the stagnant and flow region is not great enough for the vortex to occur even if the deflection is as great (if not greater) than the faster velocities [161]. This could be emulating thrombus formation *in vivo* and therefore proposes an alternative theory for how thrombus initiation occurs within venous conditions. It may not be due to the stagnant region behind the valve encouraging thrombus formation and it could actually be the presence of a vortex encouraging cell-cell interactions, e.g. collisions. The larger the vortex, the more recirculation, the greater possibility that particle-particle collisions will occur, and thus increasing the likely hood of an aggregate to form at the tip. It should be noted that under laminar conditions, it has not been reported that the PS particles will stick the PEGDA. To emphasise this it is possible to look at the chemical structures of both the PS particles and the PEGDA molecules (5.12).

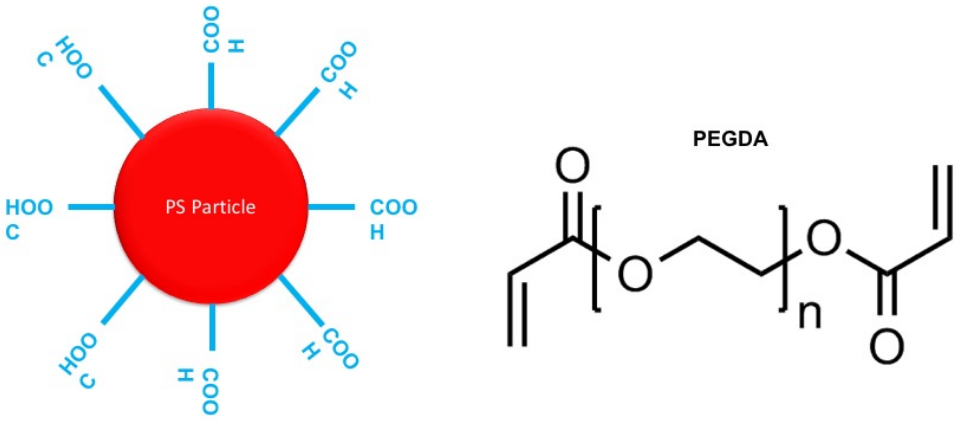

Figure 5.12: A schematic of the PS particle along with the PEGDA molecule.

It can be seen from the above figure 5.12 that the PS particle has carboxy groups on the surface, this will inherently give the PS particle a slightly negative charge. As for PEGDA, the molecule has also a slightly negative charge with the presence of the oxygen groups branching out of the molecule. As both PEGDA and PS particles are negative, this means that they do not exhibit attractive forces between them. Throughout all of the continuous flow experiments it became apparent that the 200 nm PS particles accumulated on the valve tips. In order to investigate this further, pulsed flow conditions were used with larger PS particles (3-10 µm to represent platelets and red blood cells respectively). The vortex was still present during the forward flow of the particle suspension within the pulsed flow conditions.

5.3.1 Particle Accumulation

As mentioned at the beginning of this chapter two flow conditions were investigated. Venous flow is not continuous; the blood is pumped back to the heart by muscle contractions and the valves prevent back flow [162]. These conditions were replicated using the pressure controller to create a pulsed flow. The closing of the valve causes back flow to occur, this change in flow causes a recirculation in the valve pockets. This has been hypothesised and proved using *in silco* models [4]. However, upon opening a vortex occurs at the valve tip, the same as what was seen previously in the continuous flow experiments. This is believed to be the

first experimental result showing this phenomenon at the tip of the valves therefore more investigations are carried out.

Flow and valve stiffness were altered to investigate their influence of flow patterns. Consequently these flow patterns caused the aggregation of 200 nm particles on the valve tips, figure 5.13.

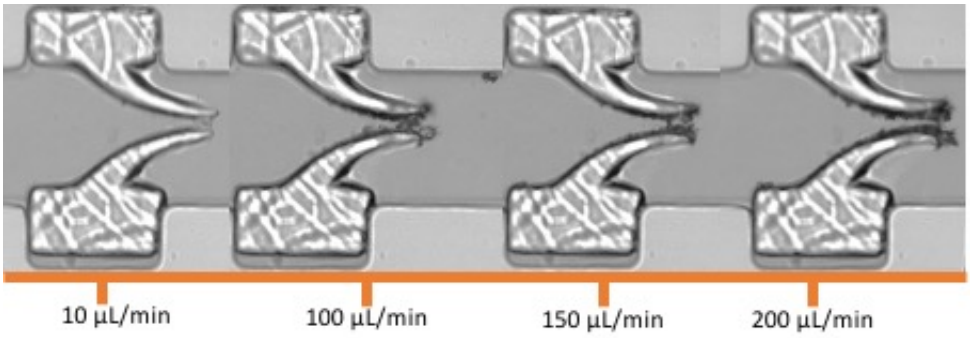

Figure 5.13: A bright field microscopy image of the 200 nm particle accumulation on the valve tips.

To better understand this phenomenon and to represent *in vivo* conditions, larger particles (3-10 μm) were used to portray platelets and red blood cells respectively. It can be seen from figure 5.14 the significant positive correlation of valve stiffness and particle accumulation for both particle sizes. According to previous results it suggested that with stiffer valves there was a larger vortex, this would also coincide with the hypothesis that greater recirculation regions also increases particle-particle interaction. In this case particle-boundary interaction. It could be an explanation as to why developing DVT increases with age, as with recent findings it has also been suggested that valves get stiffer with age [29]. Therefore, it would be appropriate to propose that this model is a beneficial insight into the mechanisms behind DVT, one that has not yet been investigated in depth.

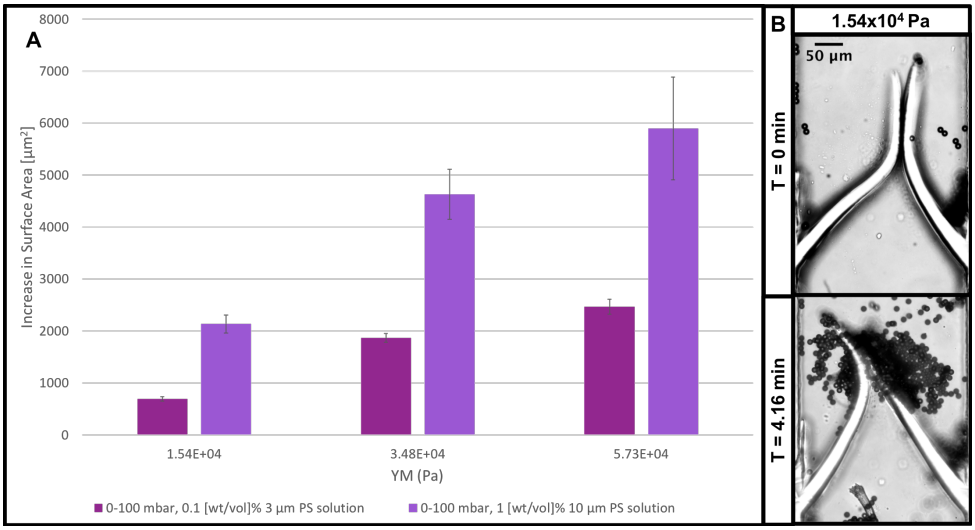

Figure 5.14: A histogram plot showing how the stiffness of the valve encourages particle accumulation on the valve tips. T = time (min).

It should be noted that in our system we can not account for the anti-thrombotic proteins that line the leaflet valves preventing the accumulation of platelets. However, it has been recognised that the valve stiffness increases with old age (as mentioned previously). This could suggest the pathological physiology that presents itself with old age could also reduce the secretion of anti-thrombotic proteins on the valve increasing the likelihood of thrombus formation. In this study it is evident that particles accumulated quicker on stiffer valves suggesting that the vortex is the cause for particle build up on the valve tips. This is potentially the first experiment of its kind observing a localised particle build up on flexible structures within a microfluidic channel. However, it is noted and understood that spherical particles suspended in water are not the most perfect representation of blood cells and blood, the point of these experiments is to simply prove that this phenomenon exists and should not be dismissed when trying to understand blood flow within veins.

In industry it is known that particles 'fall out of suspension' due to accelerated shears [163]. This could also be occurring *in vivo* as this phenomenon also occurs for various shaped particles [163]. The event of particles coming out of suspension is well known within industry and is understood across huge scales. Generally it causes sedimentation and ag-

gregation of particles/polymers within the suspension on an industrial scale and is therefore well understood for determining optimum mixing speeds and fluid conditions. *In vivo*. The valves could be causing a high enough shear rate to instigate the aggregation of platelets or pro-thrombotic proteins. For this reason further investigation needs to be carried out to understand if this occurrence is happening *in vivo* and can be replicated using this *in vitro* model.

It does not seem logical to assume that the valve *in vivo* stiffness will increase at the same rate. An idea only found to be suggested once in literature by Karasu et al. [29]. Consequently, valves were then fabricated with asymmetric stiffness. Presented here in figure 5.15 is that particles accumulate behind the more flexible valve as theorised by clinicians. However, this is opposite to what was seen in the symmetrical valves. The majority of the particle accumulation occurred behind the more flexible valve (figure 5.15 bottom image panel, left hand side valve). This indicates that the particle build up in this case is due to the back flow on the closing of the valve as opposed to the presence of a vortex on the opening of the valve.

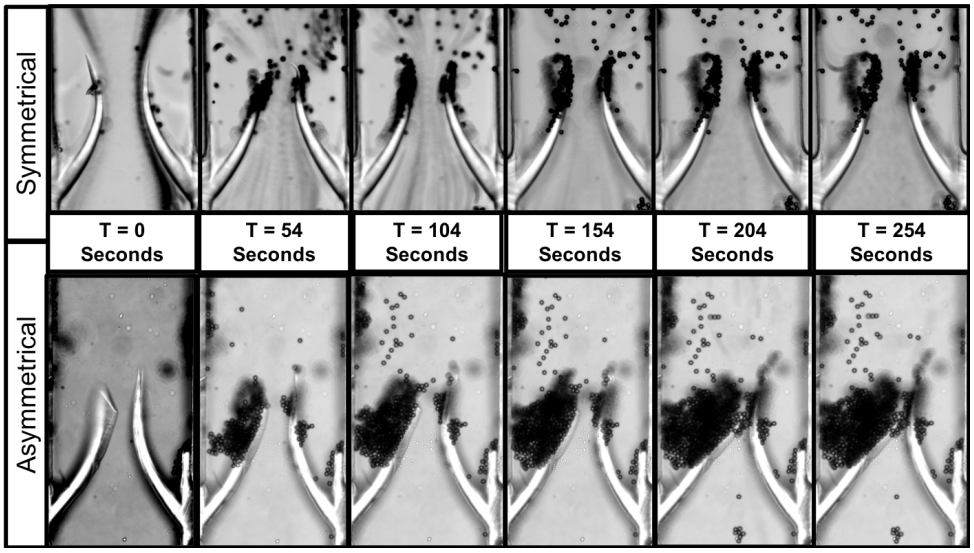

Figure 5.15: Bright field images showing the particle build up over time in symmetrical (top) and asymmetrical (bottom) stiffness of valves. The concentration of 10 μm particles is 1 % w/v. The symmetrical valve has the composition of 4 % v/v PI and 50 % vv PEGDA. The asymmetric valve is the same composition as the symmetrical valves, however the exposure time for the left (most flexible) and right (stiff) are different.

.

In the comparison between the symmetrical and asymmetrical valves seen in figure 5.14 the asymmetrical valve has a greater accumulation of particles. This is possibly a result of back flow forcing the particles onto the back of the valve. This could is a strong indication as to what could be happening to cause DVT. Although, all biological influences have been stripped from this model, the proof that valve stiffness and flow has a strong influence on particle accumulation should be sufficient proof that these parameters should not be ignored when developing the understanding the mechanisms behind DVT.

5.4 3D Printed Valve Geometry

In order to extend this model, 3D printed geometries were used with rigid valves in push the limitations of the microfluidic set up into higher *Re* numbers. The experimental parameters

reached their limit with the proposed flow detection technique. This was overcome with various simulations which will be discussed later ensuring the *Re* number of the *in vivo* case was reached and analysed. The model was progressed further into a more realistic *in vivo* situation, 3D printing was used to achieve higher *Re* numbers. Similar to the stenosis 3D printed device there where complications with the fabrication and assembly of the device. The square cross-section was maintained with the initial geometry (4x4 mm) and valves were cut out of the resin mould.

The first issue was found when the PDMS was poured over the mould, and left to cure. In the peeling away process, the valves were too intricate and did not come out of the mould. This was overcome simply by 3D printing valves as seen in the Material and Methods section 2.2.1. This meant that the valves were confined to being static, however because the valves are implanted into the PDMS, this means there is no leakage around the valves ensuring there is no flow in the z-direction (coming over/under the valve).

Even though the valves did not come out into the PDMS device, the experiment was run anyway to ensure that the 4 mm depth was suitable for GPV. Unfortunately it was found that there was too much interference. This then initiated the fabrication of a $W = 2x4mm$ device. Narrowing the device reduces the signal to noise ratio, it also makes it more comparative to the microfluidic devices which also have a more rectangular geometry as opposed to a square geometry. The addition of valves was also slightly altered. Instead of them being subtracted from the PDMS, they were 3D printed. This meant that they could be stuck to the channel walls, and embedded slightly into the PDMS to prevent leakage, sanded down to the exact channel height (2 mm) and stuck to a glass slide using the epoxy resin. Although not ideal it enabled fabrication of a fully transparent, functioning milli-fluidic chip.

The fabrication and experimental set up was finalised it was possible to explore how higher Re number's influence flow around the valves. It was found that the vortex continues to increase in size as expected in laminar conditions (figure 5.16).

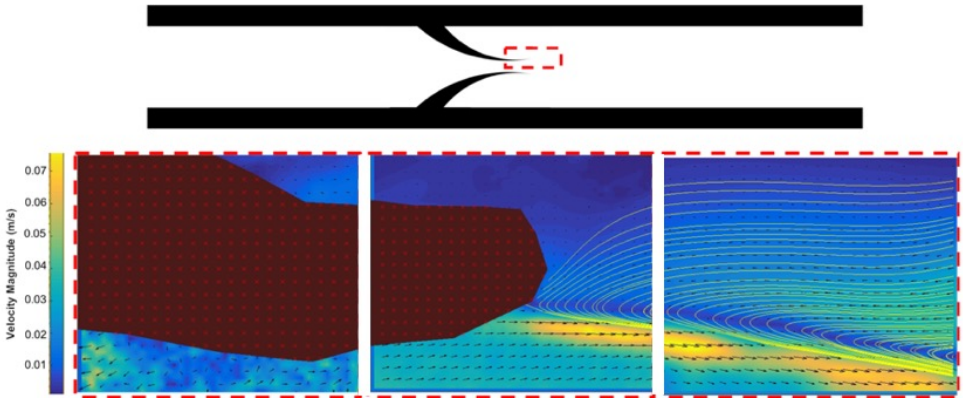

Figure 5.16: A schematic representation of the 3D printed valve device highlighting the region of interest where the results at the bottom of the figure were obtained.

The acquisition of these results was complex, air bubbles were a huge problem and interfered with GPV capture resulting in an unreliable flow regime map being plotted. To remove bubbles a pressure was applied to the outlet adding a counter pressure forcing the air out of the channel. Data collection could continue, but as seen above in figure 5.16, this was only a short term fix. A longer term fix was to clamp either side of the channel to prevent leakage from the PDMS/glass interface, which was not adhered via corona discharge.

5.5 Simulation

Valve length is a key parameter for influencing the flow conditions. Not only does it affect the deflection of the valve induced by various flow conditions it will also effect the size of the vortex at the valve tip. The fact that particle accumulation occurs predominantly at the valve tip suggests the vortex could play a fundamental role. The vortex at the tip of the valve could be trapping particles encouraging an affinity between particles and the valve surface. It should also be mentioned the valves in veins do not close fully meaning that FEM modelling would be an appropriate tool due to the mesh being present meaning that the two solid bodies cannot come together to meet in the middle due to the fluid body being between them.

Originally, the geometry used as the photo-mask was also used as the geometry for the

valves in the simulations. The inlet boundary conditions were altered to have an increasing velocity from 0.01-0.75 m/s while everything else remained constant. The walls and valve boundaries were set to have no slip boundary conditions and the outlet boundary conditions had atmospheric parameters applied. The mesh was refined at the tip of the valve to ensure the CFD model was fine enough to pick up the vortex, this was done by adding points which had a 0.1 refinement factor on the global fine-ness of the mesh. It can be seen from the long valve that the vortex occurs just behind the valve tip. This is different to the experimental results. However in this simulation the valves have no elastic property and the tips are a lot sharper than used in the experiments, which could influence the simulation results. It was seen that at lower velocities there was no vortex occurring and the velocity represented in figure 5.17 indicates that the maximum velocity magnitude is 1.376 m/s which is very high and would not be physically possible in the microfluidic devices. It suggests that the laminar flow regime does not change and the vortex does still occur. This is further indicated by figure 5.18

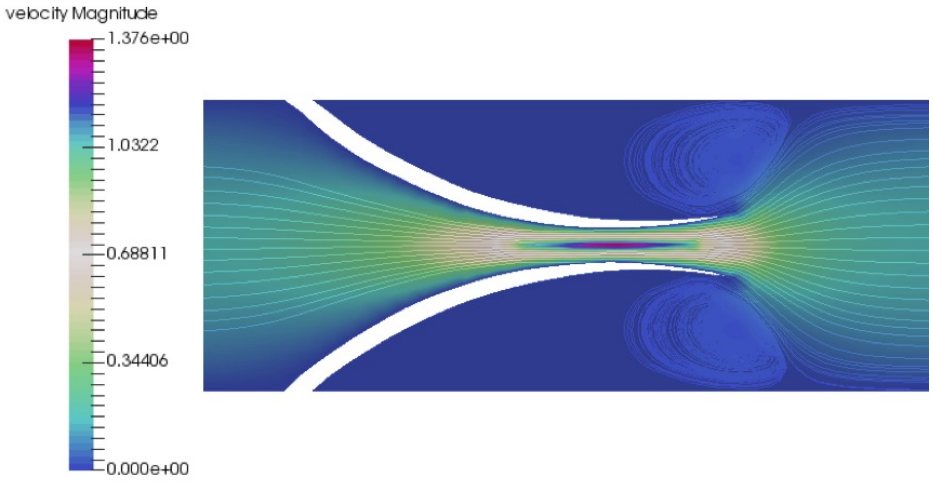

Figure 5.17: A zoomed in velocity magnitude map of featuring the long valves.

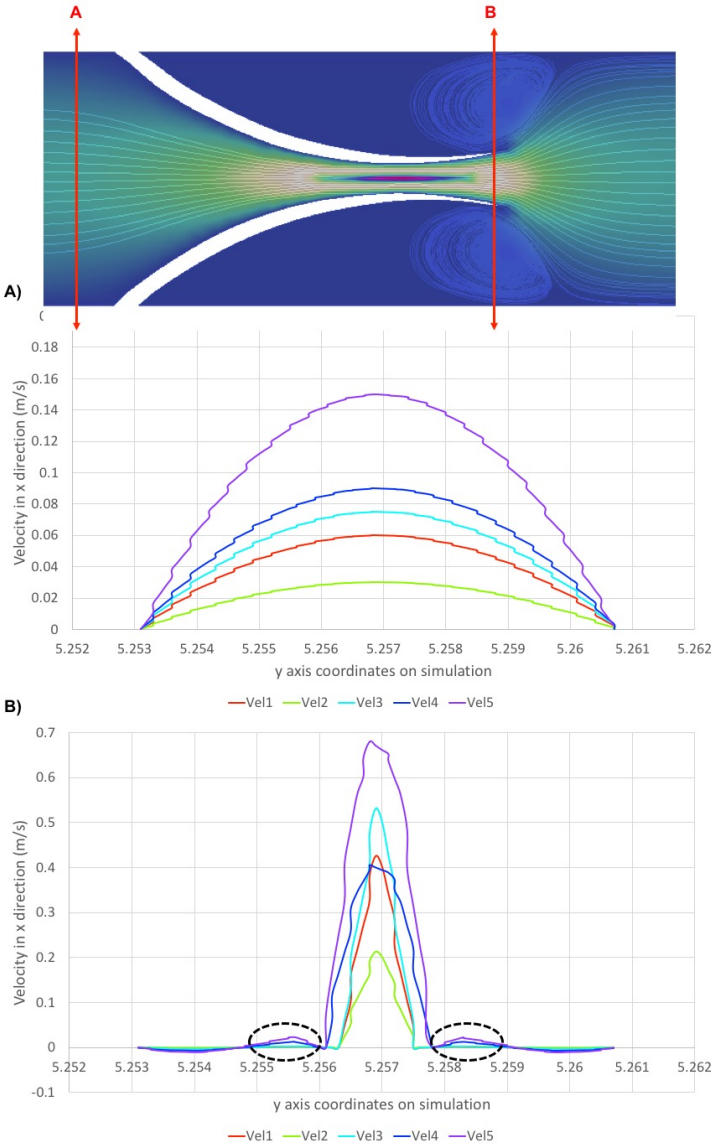

Figure 5.18: The velocity map above the graphs indicate the coordinates on position y in which Plot A) shows the parabolic flow before the valve increasing as the velocity increases. This is also highlighted in plot B), which is the velocity after the valves, it indicates that there is a vortex at velocities 4 and 5 highlighted by the black dashed circles. The Purple line in both plots is the parabolic flow visualised in the previous figure 5.17.

A shorter valve was also investigated with the same boundary conditions 5.19. And although it appears that the vortex increases in size along with the increased Re number, the shape of the vortex also changes. It appears to go from emptying behind the valves at at the experimental *Re* number to recirculating at the valve tips at the higher *Re* number. This

occurs at 0.5 m/s, Re = 61 and increases in size down the channel as seen in experiments.

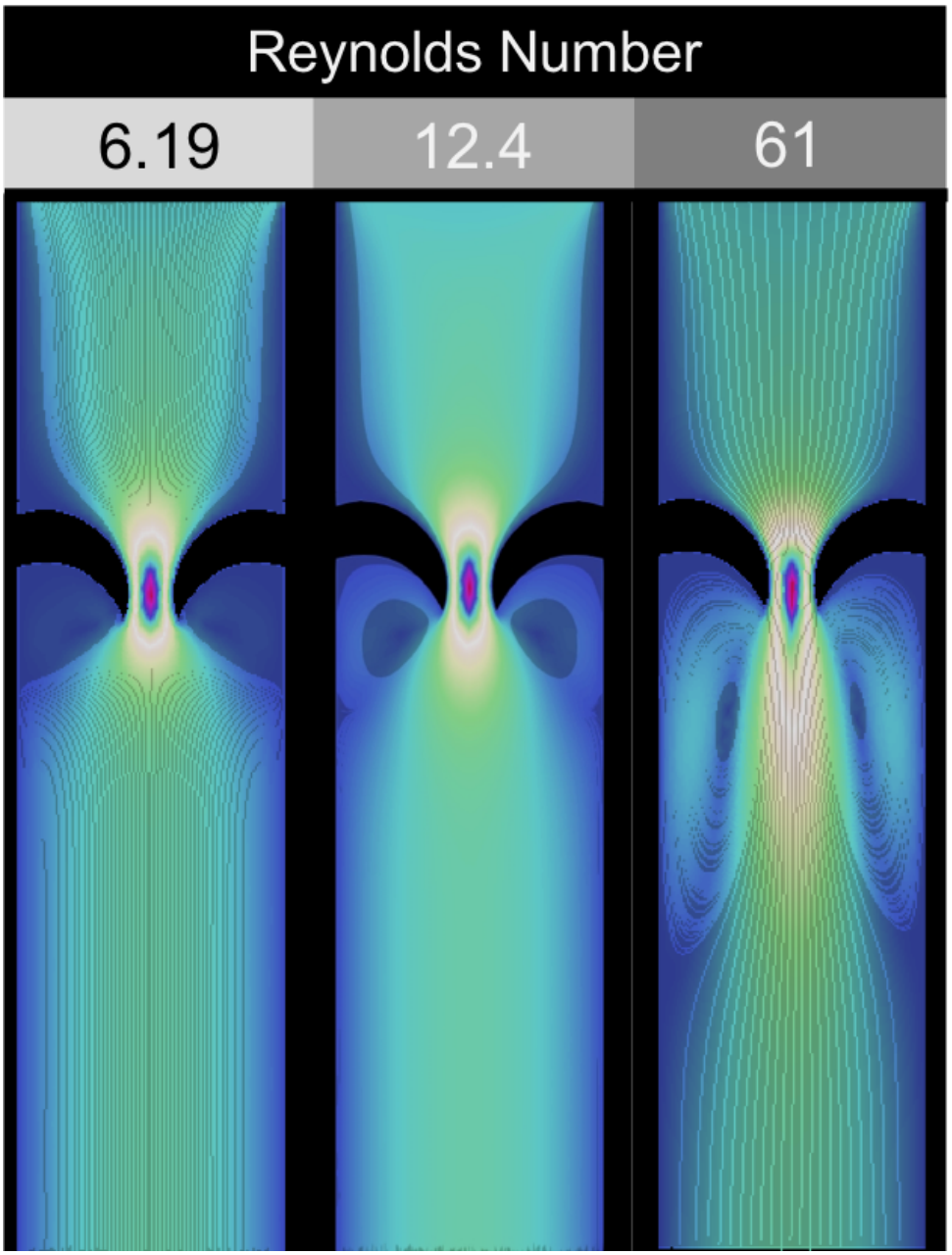

Figure 5.19: Velocity magnitude map of the simulation data showing the presence of a vortex and that it increases with *Re* number.

The reason the simulations cannot be used to validate the experimental results could be due to lack of 3D flow, however, this is unlikely due to the laminar flow profiles. To ensure this is not the case a 3D simulation was carried out, the results were the same. This in mind there must be something wrong with the mesh or the simulation itself. As mentioned previously,

the Elmer results were compared to results obtained in COMSOL, meaning the simulation is unlikely to be wrong. Narrowing it down to the mesh refinement. Another possibility is the shape of the mesh, Gmsh uses triangle/tetrahedral cells for 2D and 3D simulations respectively. Tetrahedral mesh's appear to be most commonly used for fluid flow and elastic structures, demonstrating perhaps the mesh refinement is not optimum for this simulation.

Further investigation into optimising the mesh was carried out with greater localised refinement around the valves in order to be a high enough resolution to compute the vortex. Unfortunately results were the same as witnessed earlier, indicating perhaps a geometrical issue. The valves in the experiments have a slightly rounded tip which could be strongly influencing the flow. In order to prove this the valve geometry was slightly changed to be given a 'curved' tip (figure 5.20). Again, this did not seem to aid in the validation of the experimental results with replicating and advancing the valve model to more *in vivo* conditions. Obviously in the experiments there is a force acting against the fluid because the valves are flexible. Elmer is a multiphysics software meaning it is possible to add deformation of the valve as well as the Navier-Stokes equation. This also did not replicate experimental results.

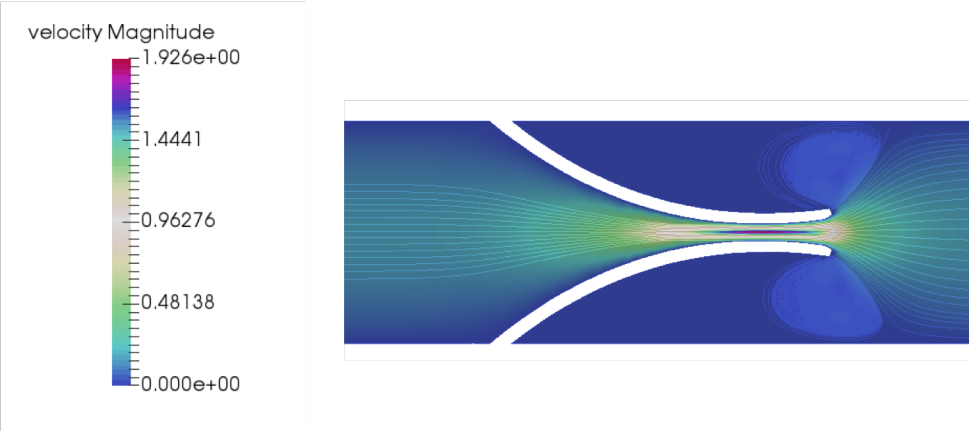

Figure 5.20: A zoomed in velocity magnitude map of featuring the long curved tipped valves.

Simulations do enforce ideal conditions that are not achievable within experiments. For example, if 0.75 m/s was pumped into the microfluidic device the inlet and outlet tubing would detach from the microfluidic device because there would be too much pressure. The aim of the simulations was to strengthen the experimental results as well as extrapolating

the micro- and milli- fluidic results to a more realistic *in vivo* condition:

- Increasing Re number
- Using GPV means that at high Re number the detection becomes unreliable in the 3D printed devices[100]

The overcoming of these limitations was carried out, however the results were not as expected. The similarities lie within the fact the: flow is laminar, the velocity increases through the valve as expected and the velocities are roughly the same as seem in experimental results. Unfortunately the main, crucial difference is the position of the vortex. This could be due to more time required for the optimisation of the mesh or that 3D simulations are definitely needed in order to get a true representation of the experimental results. As in FEM simulations the mesh optimisation is essential for getting accurate results. In this thesis, the mesh still needs refinement around the vortex area in order to get more accurate results.

CHAPTER 6

CONCLUSION AND FUTURE WORK

6.1 Conclusion

With in this thesis various models have been developed answering complex questions. In this section chapters 3-5 will be concluded followed by possible future development of each model. Three models have been developed to investigate different physical parameters which can be useful for understanding DVT. The first two models focussed on geometry and the influence on velocity through the entire device. The final model focussed on the presence of valve and observed the influence on flow patterns and particle accumulation.

6.1.1 Stenosis Model

The design and fabrication of a stenosis model to mimic the geometrical aspects of the *in vivo* murine model was accomplished. It highlighted that although the biological approach is useful for development of anti thrombotic pharmaceuticals has major limitations when it came to understanding the physics behind thrombus formation. There is not a 100% thrombus formation in the stenosis model *in vivo*, the reason for this was unclear [44]. It became clear within the literature review that little was researched in terms of geometrical influence of thrombus formation. For this reason a number of geometries was investigated. Although already known that flow within in a mouse is very unlikely to the turbulent, the *in*

vitro model was designed to prove just that. It became clear that the thrombus formation occurring within the murine model were probably not due to recirculation before the stenosis and is more likely to be due to an accumulation of blood cells at the stenosis causing a thrombus to materialise.

Two geometries where investigated including a square cross sectional device and a 1/2 cylindrical device. The square cross sectional microfluidic devices showed no change in laminar flow regime across a wide range of geometries and flow rates. In this section the GPV set up was established and optimised for micrometer and millimeter scales. Even with curvature the flow was not altered, the parabolic flow was measured in the lateral and medial direction. Unfortunately the fabrication of the full cylinder required a more complex adhesion approach. For this reason the devices following this initial simple model were all square cross sectional devices due to ease of fabrication and reproducibility.

The presence of side branches was also investigated due to reports in literature indicating that there was a recirculation happening before the stenosis preventing a thrombus forming. However, these studies indicate, that with whole blood the flow within the microfluidic dimensions are going to remain laminar with the additional flow coming from the side branch regardless to it being greater or lower than the flow within the main channel (representing the IVC within a mouse). This being said, it would seem that the majority of the murine models ignore the rest of the mouse and the fact that a bypass could be occurring. And, although studies are correct in saying that a presence of the side branch influences thrombus formation and growth the reasons behind this are not understood. Without this preliminary work in the development of the stenosis model the following models would have not been possible.

6.1.2 Bypass Model

The main limitation with this model is the fact that it is a simple geometry and the cardiovascular system is a complex network of various sized vessels which will transport blood around the stenosis. However, it is a simple, smart way to present the possibility of a bypass

which will encourage/discourage thrombus formation depending on its location and width of side branch. It was found that position A (1600 μm away from the stenosis) did not cause a bypass, and therefore has similar results to the stenosis model in that a thrombus could possibly form due to a 'bottle neck' effect increasing cell-to-cell interactions. As for positions B (600 μm) and C (300 μm) a bypass still occurs, and a stagnant region before the stenosis and after the side branch occurs. It was evident that it was dependent on multiple factors, including: width of side branch, flow rate applied to main channel and side branch as well as stenosis.

It was determined that all parameters drastically change the velocity through the channels depending on the flow rates in the side branch and main channel. The difference in flow rates through the side branch and main channel changes the pressure of the device. There will be a pressure drop when the velocity in the side branch is lower than the pressure in the main channel. There will also be a difference in pressure when the main channel has a lower pressure than the side branch. The latter is more likely to occur *in vivo*. These studies indicate that under different flow conditions and different geometries induce stagnant regions at different parts throughout the device. Three regions predominantly have stagnant regions: main channel after the side branch, side branch and bypass. A full bypasses occurred when the flow rate in the side branch was lower than in the flow rate in the main channel independent of position of side branch (B or C) and side branch width. However, this was also due to having a 80 % stenosis. If the stenosis was smaller a bypass is less likely to happen. Thus concluding the main contribution to a bypass is **stenosis** and flow rate in the **side branch**. A restriction is induced *in vivo*, when investigating DVT. With an increased stenosis there is likely to be a stagnant region between the side branch and the stenosis, which is more likely to cause thrombosis. Unfortunately the velocity has not, to my knowledge, been measured *in vivo*.

6.1.3 Valve Model

An advancement from the simplistic stenosis model was carried out with the development of fundamental understanding of fluid structure interactions. In short, the development of a valve model has been achieved. The fabrication and characterisation of flexible valves has been carried out *in situ* developing a more representative *in vitro* model. It was possible to tune the flexibility of the valves by altering concentration of PEGDA, PI and altering the exposure time. After the characterisation of the valves using the straight geometry the movement on to a more physiologically correct geometry was created. This leaflet valve geometry allowed for the observation of complex flow patterns at various flow rates. It was evident that with an increased flow rate encouraged the formation of a vortex which gained in size as the velocity increased. The flexibility of the valve was important here, as with the more flexible valves meant that there was a smaller/if any vortex formation. This was a result of the deformation of the valve being increased and reducing the gap between the valve tip and the channel wall. The stiffness of the valve also affects particle accumulation. The stiffer the valve the more particles accumulate on the valve tips. It is suggested that the vortex is what promotes the localised aggregation of particles. Furthermore, when the valves are asymmetrical the accumulation of particles occurs behind the valves. It is predicted that this happens *in vivo*. The development of this model has raised more crucial questions in order to understand the physical mechanisms behind venous thrombosis. The use of bio-compatible materials: PDMS and PEGDA means that the device is ready for the integration of biology, both materials were picked due to their biocompatibility as mentioned previously. Further development of this model would better integrate biology. In order to do this firstly endothelial cells would be added and the use of the PEGDA hydrogel would enable the development of the extra cellular matrix due to its porous network.

6.1.4 Simulations

The simulations within this thesis were not an advancement of venous flow modelling. There are many elegant *in silco* models of the complex venous system. The purpose of simulations was to validate the experimental model, with the aim to advance into more *in vitro* flow regimes. This was carried out. It was shown that the simulation data matched that of the experimental data in most cases and that the few times where it did not replicate experimental conditions there was an obvious error with the simulation and can be considered inaccurate. All results, positive and negative were presented throughout to explicitly indicate where issues were arising. In particular the 3D simulation in section 3.1.6 the results did not seem reliable. Within the whole stenosis model simulation results, although not a complicated geometry or CFD simulation was certainly successful in terms of learning 3 different software and understanding the process from designing the mesh through to interpretation of the data. A process not learnt in depth when using more conventional software such as Comsol to carry out these simulations which is a more 'black-box' approach. These skills learnt in chapter 3 were used more extensively in chapter 5 section 5.5, where they were advanced further to have moving solid structures within the simulation.

Finally, it should be stated that these simulations where by no means the state of the art, however they served a purpose and should be advanced further. Although, it would be accurate to say that mesh free simulations are more accurate when investigating fluid structure interactions in biology, giving greater control and in some retrospect, increased resolution of results.

6.2 Limitations and Future Work

Starting with the stenosis model, more blood work experiments needs to be carried out to investigate more thoroughly where platelets adhere to the channel depending on size of stenosis. This should also be replicated in the bypass design experiments. As the results could be very different with the implementation of a stagnant region before the stenosis. Another in-

teresting phenomenon not covered in this thesis would be to look at cell-cell interactions. This could involve the addition of endothelial cells to the channel walls and look at physical parameters. This could be implemented by using the different geometric designs suggested in this thesis alongside various flow rates to identify localised adherence and accumulation of platelets (or red blood cells) . It is not to my knowledge that this has been explored. However, I believe it would be an elegant, extensive way to investigate how different flow patterns induce thrombus formation within the murine model.

Throughout the majority of experimental work there has been some degree of accumulation of particles at various points through the microfluidic channel. Whether it be in the centre of the stenosis, to the tips of the valve. More investigations into the theory behind what is happening is paramount to understand how thrombus formation within the veins occurs due to the multitude of flow conditions which can occur.

6.2.1 Stenosis Model

The development of this model was carried out throughout training of GPV capture and theoretical understanding. It was useful at determining optimum microscope settings for GPV capture, as well as the development of skills: such as microfabrication, CFD and 3D printing techniques alike. To progress this in particular model the integration of biology would be useful. Although preliminary data has been collected, further investigation should be carried out. Using different viscosity of fluids, non-Newtonian fluids, alter the flexibility of the microfluidic channel etc.

Possible uses for this device could be the understanding of ageing on the coagulation of blood as well as other fundamental blood properties such as haematocrit number and rheology. Firstly, this can be investigated using blood analogues, followed by different blood samples, healthy and diseased. It could also be used to understand the influences of obesity and chemotherapy on thrombus formation within the deep veins. Using the same geometry and similar experimental set up it will be possible to use different blood samples and determine what causes more platelets to aggregate. It will be possible to investigate particular

biomarkers which may cause the increased aggregation. An area of interest was the anomaly result collected when using whole blood. The majority of blood samples was collected from <50 years of age except one. The one sample that was collected from a volunteer >50 years reproduced the results witnessed in the murine models. This could either be coincidence or a factor of age as mentioned in the introduction, the likelihood of developing DVT increases with age. Therefore further investigation into this factor would be interesting and useful for understanding the physical mechanisms behind DVT. It could also be possible to line the device with cells and look into biomarkers using fluorescent microscopy. Possible markers could be pro-thrombotic proteins: fibrin/thrombin/von Willebrand factor. Another interesting parameter not investigated within this study is the influence of the elasticity of the channel wall. This would be an important factor when trying to understand the biological responses in relation to mechanistic physiology (e.g. increased fibrotic blood vessel tissue would increase the rigidity of the vessel). This is just a couple of ways in which the stenosis model can be expanded and although not investigated in this thesis are parameters that are in need of investigating to truly understand the physical parameters of DVT.

6.2.2 Bypass Model

The bypass model was advancing into a more complex design, involving pumps to constrict the channel from both sides. Unfortunately the PDMS was too stiff to apply a sufficient enough stenosis to the main channel to enforce a bypass. To over come this issue PDMS can be made more flexible by altering the curing agent to PDMS ratio. This would enhance the flexibility thus allowing for more refined control over the stenosis over time. The bypass model, as with the other models, uses water and particle suspensions which is not representative of whole blood. This can be over come by making blood mimicking fluids. The use of more viscous fluid would have different parameters in which induce a bypass. The bypass could also be made more complicated in replication of the complex network of blood vessels *in vivo*.

To push this study further it would have been useful to calculate the pressure drop through-

out the channel. This can be linked to the velocity through the IVC and a side branch *in vivo* it would be an elegant way to begin to understand blood flow through the venous system. Obviously this would not be representative of a human/large mammal case due to the presence of valve but the integration of valves and the bypass design could be a possible solution. This would not negate the whole study, as flexibility of the valve will influence the resistance of fluid being able to flow through the channel and will create a restriction if the valves are stiff enough.

It does need to be determined what is the actual cause of the thrombus before the stenosis and although this model has highlighted that a bypass can happen, it has also demonstrated that there are multiple stagnant regions in which a thrombus can occur as well as the accumulation of particles on the bifurcations. This raises the question is the thrombus forming elsewhere and getting stuck at the stenosis or is it actually forming before the stenosis?

6.2.3 Valve Model

The development of this model has given rise to many more questions and paths to aid in the development of understanding physical mechanisms behind DVT. From a critical perspective the model lacks biological input throughout, however thorough characterisation has been carried out providing an ideal platform to further investigate the link between physical parameter and biological responses in DVT (and potentially other venous diseases). The first obvious advancement would be to flow blood through the valves and determine whether or not they behave similarly to the simple fluid; with the localised particle accumulation at the valve tips. This can be carried out in stages, by using other transparent non-Newtonian fluids to mimic in order to mimic blood before carrying out actual blood experiments. Further down the line, detailed routes such as identifying how haematocrit influences flow patterns and thrombus formation would be very interesting.

Another advancement could be to develop the device itself into more of a vein-on-a-chip with the addition of endothelial cells. This would require extensive characterisation in order to seed the cells into the device and proliferate into a homogenous monolayer across the

surface of the device. In order to aid with the adhesion of endothelial cells various proteins can also be loaded to coat the device prior to cell seeding. Proteins such as collagen and fibrinogen have been used previously. Once the cells are seeded into the device it would enable the investigation of cell-cell interaction. Although, personally, the investigation of different morphologies of cells throughout the device would be the first parameter to look at. The morphology of the cell may influence secretion of pro-thrombotic or non-thrombotic proteins which will itself influence platelet aggregation. The morphology of the cells may change depending on the stiffness of the valve making it a good starting point into trying to understand why valves are important to thrombus formation. Finally it has already been proven that valve stiffness causes different flow patterns around the valve, it would be interesting to see how these flow patterns also influence the endothelial cells.

This will truely become a vein-on-a-chip device to look at various venous diseases understanding fundamental mechanisms behind secretion of specific anti-thrombotic and thrombotic proteins as bio-markers.

6.2.4 Simulations

Although FE simulations are not optimal for carrying out such complex simulations on fluid-structure interactions it does have the added advantage that localised mesh refinement can increase stiffness along the valve. This would be interesting to investigate how localised stiffness can influence the flow through the valve. Another more simple development would be to replicate the experimental results by having the valves acting as two separate physical groups in order to apply asymmetrical stiffness to the valves.

Further development of mesh free simulation software should be carried out to make it more accessible to other disciplines, like FE simulation software. As it currently stands, mesh free simulations are restricted to those who have the suitable expertise and are not yet accessible to the wider academic population. It provides a very powerful tool for looking into biological mechanism, especially for the cases of DVT where there is high variability arising from a physiological and environmental circumstances.

LIST OF REFERENCES

[1] G. E. Raskob, P. Angchaisuksiri, A. N. Blanco, H. Buller, A. Gallus, B. J. Hunt, E. M. Hylek, A. Kakkar, S. V. Konstantinides, M. McCumber, Y. Ozaki, A. Wendelboe, and J. I. Weitz. Thrombosis: A major contributor to global disease burden. *Arteriosclerosis, Thrombosis, and Vascular Biology*, 34(11):2363–2371, 2014.

[2] Manuel Megías Pacheco, Pilar Molist García, and Manuel Ángel Pombal Diego. Atlas of Plant and Animal Histology, Cardiovascular, 2019.

[3] Roberto Cerbino and Veronique Trappe. Differential dynamic microscopy: Probing wave vector dependent dynamics with a microscope. *Physical Review Letters*, 100(18):1–4, 2008.

[4] Mostapha Ariane, Mohamed Hatem Allouche, Marco Bussone, Fausto Giacosa, Frédéric Bernard, Mostafa Barigou, and Alessio Alexiadis. Discrete multi-physics: A mesh-free model of blood flow in flexible biological valve including solid aggregate formation. *PLOS ONE*, 12(4):e0174795, apr 2017.

[5] Caroline a Schneider, Wayne S Rasband, and Kevin W Eliceiri. NIH Image to ImageJ: 25 years of image analysis. *Nature Methods*, 9(7):671–675, 2012.

[6] B J Hunt. The prevention of hospital-acquired venous thromboembolism in the United Kingdom. *British Journal of Haematology*, 144(5):642–652, 2009.

[7] Fritz Ullmann. Ullmann's Chemical Engineering and Plant Design, Volumes 1-2.

[8] Nigel Mackman. New insights into the mechanisms of venous thrombosis. *The Journal of clinical investigation*, 122(7):2331–6, 2012.

[9] Marcos de Bastos, Sandhi M. Barreto, Jackson S. Caiafa, T??nia Boguchi, Jos?? Luiz Padilha Silva, and Suely M. Rezende. Derivation of a risk assessment model for hospital-acquired venous thrombosis: the NAVAL score. *Journal of Thrombosis and Thrombolysis*, 41(4):628–635, 2016.

[10] Chantal Kang, Michel Bonneau, Jean Philippe Brouland, Claire Bal Dit Sollier, and Ludovic Drouet. In vivo pig models of venous thrombosis mimicking human disease. *Thrombosis and Haemostasis*, 89(2):256–263, 2003.

[11] Wei Huang, Robert J. Goldberg, Frederick A. Anderson, Alexander T. Cohen, and Frederick A. Spencer. Occurrence and predictors of recurrence after a first episode of acute venous thromboembolism: population-based Worcester Venous Thromboembolism Study. *Journal of Thrombosis and Thrombolysis*, 41(3):525–538, 2016.

[12] Daniel Theodoro, Michael Blaivas, Sandeep Duggal, Graham Snyder, and Michael Lucas. Real-time B-mode ultrasound in the ED saves time in the diagnosis of deep vein thrombosis (DVT). *American Journal of Emergency Medicine*, 22(3):197–200, 2004.

[13] Gordon J. Betts, Peter Desiax, Eddie Johnson, Jody E. Johnson, Oksana Korol, Dean Kruse, Brandon Pore, James A. Wise, Mark Womble, and Kelly A. Young. *Anatomy & Physiology*. 2017.

[14] A Noble. *The Cardiovascular System*. Systems of the body. Elsevier Churchill Livingstone, 2005.

[15] Scott L. Diamond. Systems Analysis of Thrombus Formation. *Circulation Research*, 118(9):1348–1362, 2016.

[16] Zaverio M. Ruggeri. Mechanisms initiating platelet thrombus formation. *Thrombosis and Haemostasis*, 78(1):611–616, 1997.

[17] M.M. Maria M Aleman, Bethany L B.L. Walton, J.R. James R Byrnes, and A.S. Alisa S Wolberg. Fibrinogen and red blood cells in venous thrombosis. *Thrombosis Research*, 133(SUPPL. 1):S38–S40, 2014.

[18] J F Théorêt, J G Bienvenu, a Kumar, and Y Merhi. P-selectin antagonism with recombinant p-selectin glycoprotein ligand-1 (rPSGL-Ig) inhibits circulating activated platelet binding to neutrophils induced by damaged arterial surfaces. *The Journal of pharmacology and experimental therapeutics*, 298(2):658–64, 2001.

[19] Adeline Vasquez-Parra. Nommer l'Acadien dans les empires britannique et français (1755-1765): Un enjeu politique ou économique? *Acadiensis*, 47(1):86–117, 2018.

[20] Jian Ning Zhang, Angela L. Bergeron, Qinghua Yu, Carol Sun, Larry V. McIntire, José A. López, and Jing Fei Dong. Platelet aggregation and activation under complex patterns of shear stress. *Thrombosis and Haemostasis*, 88(5):817–821, 2002.

[21] P. B. Snyder, R. J. Groebner, A. W. Leonard, T. H. Osborne, and H. R. Wilson. Development and validation of a predictive model for the pedestal height. *Physics of Plasmas*, 16(5):4902–4908, 2009.

[22] Judith M E M Cosemans, Anne Angelillo-Scherrer, Nadine J A Mattheij, and Johan W M Heemskerk. The effects of arterial flow on platelet activation, thrombus growth, and stabilization, 2013.

[23] Hoyoon Lee, Gyehyu Kim, Chaeseung Lim, ByoungKwon Lee, and Sehyun Shin. A simple method for activating the platelets used in microfluidic platelet aggregation tests: Stirring-induced platelet activation. *Biomicrofluidics*, 10(6):064118, nov 2016.

[24] A. D. MCLACHLIN, J. A. MCLACHLIN, T. A. JORY, and E. G. RAWLING. Venous stasis in the lower extremities. *Annals of surgery*, 152:678–685, 1960.

[25] E G Bovill and A van der Vliet. Venous valvular stasis-associated hypoxia and thrombosis: what is the link? *Annu Rev Physiol*, 73:527–545, 2011.

[26] A. Brill, G. L. Suidan, and D. D. Wagner. Hypoxia, such as encountered at high altitude, promotes deep vein thrombosis in mice. *Journal of Thrombosis and Haemostasis*, 11(9):1773–1775, sep 2013.

[27] Chris I. Jones. Platelet function and ageing. *Mammalian Genome*, 27(March):358–366, 2016.

[28] Thuy Pham, Fatiesa Sulejmani, Erica Shin, Di Wang, and Wei Sun. Quantification and comparison of the mechanical properties of four human cardiac valves. *Acta Biomaterialia*, 54:345–355, may 2017.

[29] A. Karasu, A. Šrámek, F. R. Rosendaal, R. J. van der Geest, and A. van Hylckama Vlieg. Aging of the venous valves as a new risk factor for venous thrombosis in the elderly: the BATAVIA study. *Journal of Thrombosis and Haemostasis*, 16(1):96–103, 2018.

[30] Johan Zotterman, Max Bergkvist, Fredrik Iredahl, Erik Tesselaar, and Simon Farnebo. Monitoring of partial and full venous outflow obstruction in a porcine flap model using laser speckle contrast imaging. *Journal of plastic, reconstructive & aesthetic surgery : JPRAS*, pages 936–943, 2016.

[31] S P Grover, C E Evans, A S Patel, B Modarai, P Saha, and A Smith. Assessment of Venous Thrombosis in Animal Models. *Arterioscler Thromb Vasc Biol*, 36(2):245–252, 2016.

[32] Holly Payne and Alexander Brill. Stenosis of the Inferior Vena Cava: A Murine Model of Deep Vein Thrombosis. *Journal of Visualized Experiments*, (130):6–11, 2017.

[33] J A Diaz, D M Farris, S K Wrobleski, D D Myers, and T W Wakefield. Inferior vena cava branch variations in C57BL/6 mice have an impact on thrombus size in an IVC ligation (stasis) model. *J Thromb Haemost*, 13(4):660–664, 2015.

[34] P. K. Henke, L. A. DeBrunye, R. M. Strieter, J. S. Bromberg, M. Prince, A. M. Kadell, M. Sarkar, F. Londy, and T. W. Wakefield. Viral IL-10 Gene Transfer Decreases Inflammation and Cell Adhesion Molecule Expression in a Rat Model of Venous Thrombosis. *The Journal of Immunology*, 164(4):2131–2141, 2000.

[35] Bridget M. Seitz, Teresa Krieger-Burke, Gregory D. Fink, and Stephanie W. Watts. Serial Measurements of Splanchnic Vein Diameters in Rats Using High-Frequency Ultrasound. *Frontiers in Pharmacology*, 7(May):1–10, 2016.

[36] Peter H Lin, Changyi Chen, Scott M Surowiec, Brian Conklin, L Ruth, and Alan B Lumsden. Evaluation of thrombolysis in a porcine model of chronic deep venous thrombosis : An endovascular model. pages 621–627, 1985.

[37] B Geier, L Barbera, I Bolle, and K Militzer. Laparoscopic Ligation of the Infrarenal Vena Cava in Combination With Transfemoral Thrombin Infusion : A New Animal Model of Chronic Deep Venous Thrombosis. 548:542–548, 2005.

[38] J. H. Frisbie. An animal model for venous thrombosis and spontaneous pulmonary embolism. *Spinal Cord*, 43(11):635–639, 2005.

[39] Elodie Darnis, Soren Boysen, Anne Christine Merveille, Loïc Desquilbet, Serge Chalhoub, and Kris Gommeren. Establishment of reference values of the caudal vena cava by fast-ultrasonography through different views in healthy dogs. *Journal of Veterinary Internal Medicine*, 32(4):1308–1318, 2018.

[40] Elizabeth A. Stone and Gwendolyn J. Stewart. Architecture and structure of canine veins with special reference to confluences. *The Anatomical Record*, 222(2):154–163, 1988.

[41] T W Wakefield, R M Strieter, R Schaub, D D Myers, M R Prince, S K Wrobleski, F J Londy, a M Kadell, S L Brown, P K Henke, and L J Greenfield. Venous thrombosis prophylaxis by inflammatory inhibition without anticoagulation therapy. *Journal of vascular surgery : official publication, the Society for Vascular Surgery [and] International Society for Cardiovascular Surgery, North American Chapter*, 31(2):309–324, 2000.

[42] L. J. Downing, T. W. Wakefield, R. M. Strieter, M. R. Prince, F. J. Londy, J. B. Fowlkes, M. S. Hulin, A. M. Kadell, C. A. Wilke, S. L. Brown, S. K. Wrobleski, M. D. Burdick, D. C. Anderson, L. J. Greenfield, and T. B. Baxter. Anti-P-selectin antibody decreases inflammation and thrombus formation in venous thrombosis. *Journal of Vascular Surgery*, 25(5):816–828, 1997.

[43] JD Mortensen, Steven Talbot, and John A. Burkart. Cross-sectional internal diameters of human cervical and femoral blood vessels: Relationship to subject's sex, age, body size. *The Anatomical Record*, 226(1):115–124, 1990.

[44] Nigel Mackman. Mouse models of venous thrombosis are not equal. *Blood*, 127(21):2510–2511, 2016.

[45] Alexander Brill, Tobias a Fuchs, Anil K Chauhan, Janie J Yang, Simon F De Meyer, Maria Ko, Thomas W Wakefield, Bernhard La, Steffen Massberg, Denisa D Wagner, S. F. De Meyer, M. Kollnberger, Thomas W Wakefield, B. Lammle, Steffen Massberg, and Denisa D Wagner. von Willebrand factor – mediated platelet adhesion is critical for deep vein thrombosis in mouse models. *Blood*, 117(4):1400–1407, jan 2011.

[46] Tanja Schönfelder, Moritz Brandt, Sabine Kossmann, Tanja Knopp, Thomas Münzel, Ulrich Walter, Susanne H. Karbach, and Philip Wenzel. Lack of T-bet reduces monocytic interleukin-12 formation and accelerates thrombus resolution in deep vein thrombosis. *Scientific Reports*, 8(1):1–10, 2018.

[47] Mitchell R. Dyer, Qiwei Chen, Shannon Haldeman, Hamza Yazdani, Rosemary Hoffman, Patricia Loughran, Allan Tsung, Brian S. Zuckerbraun, Richard L. Simmons, and Matthew D. Neal. Deep vein thrombosis in mice is regulated by platelet HMGB1 through release of neutrophil-extracellular traps and DNA. *Scientific Reports*, 8(1):1–7, 2018.

[48] J Zhou, A V Ellis, and N H Voelcker. Recent developments in PDMS surface modification for microfluidic devices. *Electrophoresis*, 31(1):2–16, 2010.

[49] Tadayuki Yago, Zhenghui Liu, Jasimuddin Ahamed, and Rodger P. McEver. Cooperative PSGL-1 and CXCR2 signaling in neutrophils promotes deep vein thrombosis in mice. *Blood*, 132(13):1426–1437, 2018.

[50] Anil K. Chauhan, Janka Kisucka, Alexander Brill, Meghan T. Walsh, Friedrich Scheiflinger, and Denisa D. Wagner. ADAMTS13: a new link between thrombosis and inflammation. *The Journal of Experimental Medicine*, 205(9):2065–2074, 2008.

[51] Roberto Weigert. Intravital microscopy: a practical guide on imaging intracellular structures in live animals. *Bioarchitecture*, 2(5):143–157, 2012.

[52] Marie-Luise von Brühl, Konstantin Stark, Alexander Steinhart, Sue Chandraratne, Ildiko Konrad, Michael Lorenz, Alexander Khandoga, Anca Tirniceriu, Raffaele Coletti, Maria Köllnberger, Robert A. Byrne, Iina Laitinen, Axel Walch, Alexander Brill, Susanne Pfeiler, Davit Manukyan, Siegmund Braun, Philipp Lange, Julia Riegger, Jerry Ware, Annekathrin Eckart, Selgai Haidari, Martina Rudelius, Christian Schulz, Katrin Echtler, Volker Brinkmann, Markus Schwaiger, Klaus T. Preissner, Denisa D. Wagner, Nigel Mackman, Bernd Engelmann, and Steffen Massberg. Monocytes, neutrophils, and platelets cooperate to initiate and propagate venous thrombosis in mice in vivo. *The Journal of Experimental Medicine*, 209(4):819–835, 2012.

[53] Jose A. Diaz, Andrea T. Obi, Daniel D. Myers, Shirley K. Wrobleski, Peter K. Henke, Nigel MacKman, and Thomas W. Wakefield. Critical review of mouse models of venous thrombosis. *Arteriosclerosis, Thrombosis, and Vascular Biology*, 32(3):556–562, 2012.

[54] Hassan Albadawi, Avery A Witting, Yash Pershad, Alex Wallace, Andrew R Fleck, Peter Hoang, and Rahmi Oklu. Animal models of venous thrombosis. 7(Suppl 3):197–206, 2017.

[55] B Y C H Barnett, R J Harrison, J D W Tomlinson, and St Thomas. VARIATIONS IN THE VENOUS SYSTEMS OF MAMMALS. pages 442–487, 1957.

[56] Jevgenia Zilberman-Rudenko, Rachel M. White, Dmitriy A. Zilberman, Hari H.S. Lakshmanan, Rachel A. Rigg, Joseph J. Shatzel, Jeevan Maddala, and Owen J.T. McCarty. Design and Utility of a Point-of-Care Microfluidic Platform to Assess Hematocrit and Blood Coagulation. *Cellular and Molecular Bioengineering*, 11(6):519–529, 2018.

[57] Stephanie J. Munger, John D. Kanady, and Alexander M. Simon. Absence of venous valves in mice lacking Connexin37. *Developmental Biology*, 373(2):338–348, 2013.

[58] Katelyn N Brinegar. Iliac vein compression syndrome: Clinical, imaging and pathologic findings. *World Journal of Radiology*, 7(11):375, 2015.

[59] R. Rezakhaniha, E. Fonck, C. Genoud, and N. Stergiopulos. Role of elastin anisotropy in structural strain energy functions of arterial tissue. *Biomechanics and Modeling in Mechanobiology*, 10(4):599–611, 2011.

[60] Stephen C. Terry, John H. Herman, and James B. Angell. A Gas Chromatographic Air Analyzer Fabricated on a Silicon Wafer. *IEEE Transactions on Electron Devices*, 26(12):1880–1886, 1979.

[61] George M. Whitesides. The origins and the future of microfluidics. *Nature*, 442(7101):368–373, 2006.

[62] David C. Duffy, J. Cooper McDonald, Olivier J A Schueller, and George M. Whitesides. Rapid prototyping of microfluidic systems in poly(dimethylsiloxane). *Analytical Chemistry*, 70(23):4974–4984, dec 1998.

[63] NASA) Benson, Tom (Glenn Research Centre. Reynolds Number.

[64] Sara Lindström and Helene Andersson-Svahn. Overview of single-cell analyses: microdevices and applications. *Lab on a Chip*, 10(24):3363, 2010.

[65] Christopher Probst, Stefan Schneider, and Peter Loskill. High-throughput organ-on-a-chip systems: Current status and remaining challenges. *Current Opinion in Biomedical Engineering*, 6:33–41, jun 2018.

[66] João Ribas, Hossein Sadeghi, Amir Manbachi, Jeroen Leijten, Katelyn Brinegar, Yu Shrike Zhang, Lino Ferreira, and Ali Khademhosseini. Cardiovascular Organ-on-a-Chip Platforms for Drug Discovery and Development. *Applied In Vitro Toxicology*, 2(2):82–96, 2016.

[67] Amir Bein, Woojung Shin, Sasan Jalili-Firoozinezhad, Min Hee Park, Alexandra Sontheimer-Phelps, Alessio Tovaglieri, Angeliki Chalkiadaki, Hyun Jung Kim, and Donald E. Ingber. Microfluidic Organ-on-a-Chip Models of Human Intestine. *Cellular and Molecular Gastroenterology and Hepatology*, 5(4):659–668, 2018.

[68] Dongeun (Dan) Huh. A Human Breathing Lung-on-a-Chip. *Annals of the American Thoracic Society*, 12(Supplement 1):S42–S44, 2015.

[69] L G Rigat-Brugarolas, A Elizalde-Torrent, M Bernabeu, M De Niz, L Martin-Jaular, C Fernandez-Becerra, A Homs-Corbera, J Samitier, and H a del Portillo. A functional microengineered model of the human splenon-on-a-chip. *Lab on a Chip*, 14(10):1715, 2014.

[70] Anna Marsano, Chiara Conficconi, Marta Lemme, Paola Occhetta, Emanuele Gaudiello, Emiliano Votta, Giulia Cerino, Alberto Redaelli, and Marco Rasponi. Beating heart on a chip: A novel microfluidic platform to generate functional 3D cardiac microtissues. *Lab on a Chip*, 16(3):599–610, 2016.

[71] Ravi Sinha, Séverine Le Gac, Nico Verdonschot, Albert van den Berg, Bart Koopman, and Jeroen Rouwkema. Endothelial cell alignment as a result of anisotropic strain and flow induced shear stress combinations. *Scientific Reports*, 6(1):29510, sep 2016.

[72] Eunseop Yeom, Jun Hong Park, Yang Jun Kang, and Sang Joon Lee. Microfluidics for simultaneous quantification of platelet adhesion and blood viscosity. *Nature Publishing Group*, (April):1–11, 2016.

[73] Miguel E Combariza, Xinghuo Yu, Warwick S Nesbitt, Arnan Mitchell, and Francisco J Tovar-lopez. Nonlinear Dynamic Modelling of Platelet Aggregation via Microfluidic Devices. *IEEE Trans Biomed Eng*, 62(7):1718–1727, 2015.

[74] Walter H. Reinhart, Nathaniel Z. Piety, Jeroen S. Goede, and Sergey S. Shevkoplyas. Effect of osmolality on erythrocyte rheology and perfusion of an artificial microvascular network. *Microvascular Research*, 98:102–107, 2015.

[75] D P Sarvepalli, D W Schmidtke, and M U Nollert. Design considerations for a microfluidic device to quantify the platelet adhesion to collagen at physiological shear rates. *Ann Biomed Eng*, 37(7):1331–1341, 2009.

[76] Zaverio M Ruggeri, Jennifer N Orje, Rolf Habermann, Augusto B Federici, and Armin J Reininger. Activation-Independent Platelet Adhesion and Aggregation under Elevated Shear Stress Running title : Platelet adhesion and aggregation in flowing blood. *Blood*, 108(6):1903–1911, 2006.

[77] Jevgenia Zilberman-Rudenko, Joanna L. Sylman, Kathleen S. Garland, Cristina Puy, Andrew D. Wong, Peter C. Searson, and Owen J. T. McCarty. Utility of microfluidic devices to study the platelet–endothelium interface. *Platelets*, 00(00):1–8, 2017.

[78] E Gutierrez, B G Petrich, S J Shattil, M H Ginsberg, A Groisman, and A Kasirer-Friede. Microfluidic devices for studies of shear-dependent platelet adhesion. *Lab Chip*, 8(9):1486–1495, 2008.

[79] L.D.C. D Casa and D.N. N Ku. Geometric design of microfluidic chambers: platelet adhesion versus accumulation. *Biomed Microdevices*, 16(1):115–126, 2014.

[80] I Goldstein, B Halpern, and L Robert. © 1967 Nature Publishing Group. *Nature*, pages 44–47, 1967.

[81] Arnost Fronek, Michael H. Criqui, Julie Denenberg, and Robert D. Langer. Common femoral vein dimensions and hemodynamics including Valsalva response as a function of sex, age, and ethnicity in a population study. *Journal of Vascular Surgery*, 33(5):1050–1056, 2001.

[82] Klaus D. Hinsch. Three-dimensional particle velocimetry. *Measurement Science and Technology*, 6(6):742–753, 1995.

[83] J. G. Santiago, S. T. Wereley, C. D. Meinhart, D. J. Beebe, and R. J. Adrian. A particle image velocimetry system for microfluidics. *Experiments in Fluids*, 25(4):316–319, sep 1998.

[84] Stefano Buzzaccaro, Eleonora Secchi, and Roberto Piazza. Ghost particle velocimetry: Accurate 3d flow visualization using standard lab equipment. *Physical Review Letters*, 111(4):1–5, 2013.

[85] B. Lecordier, M. Mouqallid, S. Vottier, E. Rouland, D. Allano, and M. Trinite. CCD Recording method for cross-correlation PIV development in unstationary high speed flow. *Experiments in Fluids*, 17(3):205–208, 1994.

[86] Wing T. Lai, Daniel C. Bjorkquist, Martin P. Abbott, and Amir A. Naqwi. Video systems for PIV recording. *Measurement Science and Technology*, 9(3):297–308, 1998.

[87] Jerry Westerweel, Gerrit E. Elsinga, and Ronald J. Adrian. Particle Image Velocimetry for Complex and Turbulent Flows. *Annual Review of Fluid Mechanics*, 45(1):409–436, 2013.

[88] D. G. Abdelsalam, M. Stanislas, and S. Coudert. PIV camera response to high frequency signal: Comparison of CCD and CMOS cameras using particle image simulation. *Measurement Science and Technology*, 25(8), 2014.

[89] J Westerweel. Fundamentals of digital particle image velocimetry. *Measurement Science and Technology*, 8(12):1379–1392, dec 1997.

[90] F. Alberini, L. Liu, E. H. Stitt, and M. J.H. Simmons. Comparison between 3-D-PTV and 2-D-PIV for determination of hydrodynamics of complex fluids in a stirred vessel. *Chemical Engineering Science*, 171:189–203, 2017.

[91] Sudong Kim, Hyunjae Lee, Minhwan Chung, and Noo Li Jeon. Engineering of functional, perfusable 3D microvascular networks on a chip. *Lab on a Chip*, 13(8):1489–1500, 2013.

[92] Ronald J. Adrian. Particle-Imaging Techniques for Experimental Fluid Mechanics. *Annual Review of Fluid Mechanics*, 23:261–304, 1991.

[93] Graciela Wild Padua and Qin Wang. *Nanotechnology Research Methods for Foods and Bioproducts*. Number 1. Wiley-Blackwell, Oxford, UK, apr 2012.

[94] Richard D. Keane and Ronald J. Adrian. Theory of cross-correlation analysis of PIV images. *Applied Scientific Research*, 49(3):191–215, 1992.

[95] L. Gan. Stereoscopic PIV and Its Applications on Reconstruction Three-Dimensional Flow Field. In *The Particle Image Velocimetry - Characteristics, Limits and Possible Applications*, volume i, page 13. InTech, may 2012.

[96] Rui Lima, Shigeo Wada, Shuji Tanaka, Motohiro Takeda, Takuji Ishikawa, Ken Ichi Tsubota, Yohsuke Imai, and Takami Yamaguchi. In vitro blood flow in a rectangular PDMS microchannel: Experimental observations using a confocal micro-PIV system. *Biomedical Microdevices*, 10(2):153–167, 2008.

[97] B Chu. Laser Light Scattering. *Annual Review of Physical Chemistry*, 21(1):145–174, oct 1970.

[98] Jörg Stetefeld, Sean A. McKenna, and Trushar R. Patel. Dynamic light scattering: a practical guide and applications in biomedical sciences. *Biophysical Reviews*, 8(4):409–427, 2016.

[99] Rhonda Dzakpasu and Daniel Axelrod. Dynamic light scattering microscopy. A novel optical technique to image submicroscopic motions. II: Experimental applications. *Biophysical Journal*, 87(2):1288–1297, 2004.

[100] Marco Riccomi, Federico Alberini, Elisabetta Brunazzi, and Daniele Vigolo. Ghost Particle Velocimetry as an alternative to μPIV for micro/milli-fluidic devices. *Chemical Engineering Research and Design*, 133:183–194, 2018.

[101] N. M. Kovalchuk, J. Chowdhury, Z. Schofield, D. Vigolo, and M. J.H. Simmons. Study of drop coalescence and mixing in microchannel using Ghost Particle Velocimetry. *Chemical Engineering Research and Design*, 132:881–889, 2018.

[102] Chiara Martino, Daniele Vigolo, Xavier Casadevall i Solvas, Stavros Stavrakis, and Andrew J. DeMello. Real-Time PEGDA-Based Microgel Generation and Encapsulation in Microdroplets. *Advanced Materials Technologies*, 1(2):1600028, may 2016.

[103] Tohid Pirbodaghi, Daniele Vigolo, Samin Akbari, and Andrew DeMello. Investigating the fluid dynamics of rapid processes within microfluidic devices using bright-field microscopy. *Lab on a Chip*, 15(9):2140–2144, 2015.

[104] Cengage Learning, All Rights Reserved, and Cengage Learning. *A first course in element method*.

[105] Diego Gallo, Utku Gülan, Antonietta Di Stefano, Raffaele Ponzini, Beat Lüthi, Markus Holzner, and Umberto Morbiducci. Analysis of thoracic aorta hemodynamics using 3D particle tracking velocimetry and computational fluid dynamics. *Journal of Biomechanics*, 47(12):3149–3155, 2014.

[106] Klaus Jürgen Bathe and Hou Zhang. A mesh adaptivity procedure for CFD and fluid-structure interactions. *Computers and Structures*, 87(11-12):604–617, 2009.

[107] M. Simão, J. M. Ferreira, J. Mora-Rodriguez, and H. M. Ramos. Identification of DVT diseases using numerical simulations. *Medical & Biological Engineering & Computing*, 54(10):1591–1609, oct 2016.

[108] T. Bodnár, A. Sequeira, and M. Prosi. On the shear-thinning and viscoelastic effects of blood flow under various flow rates. *Applied Mathematics and Computation*, 217(11):5055–5067, 2011.

[109] Iman Borazjani. Fluid-structure interaction, immersed boundary-finite element method simulations of bio-prosthetic heart valves. *Computer Methods in Applied Mechanics and Engineering*, 257:103–116, 2013.

[110] Karyn S. Kunzelman, David W. Quick, and Richard P. Cochran. Altered collagen concentration in mitral valve leaflets: Biochemical and finite element analysis. *Annals of Thoracic Surgery*, 66(6 SUPPL.), 1998.

[111] J. A. Baier-Saip, P. A. Baier, J. C. Oliveira, and H. Baier. Linear spring stiffnesses for two-dimensional finite element modeling of arteries. *European Journal of Mechanics, A/Solids*, 72(January):57–65, 2018.

[112] Deepanshu Sodhani, Stefanie Reese, Andrey Aksenov, Sinan Soğanci, Stefan Jockenhövel, Petra Mela, and Scott E. Stapleton. Fluid-structure interaction simulation of artificial textile reinforced aortic heart valve: Validation with an in-vitro test. *Journal of Biomechanics*, 78:52–69, 2018.

[113] A L Marsden, A J Bernstein, V M Reddy, S C Shadden, R L Spilker, F P Chan, C A Taylor, and J A Feinstein. Evaluation of a novel Y-shaped extracardiac Fontan baffle using computational fluid dynamics. *J Thorac Cardiovasc Surg*, 137(2):394–403 e2, 2009.

[114] Andrew L. Kuharsky and Aaron L. Fogelson. Surface-Mediated Control of Blood Coagulation: The Role of Binding Site Densities and Platelet Deposition. *Biophysical Journal*, 80(3):1050–1074, 2001.

[115] K P Papadopoulos, M Gavaises, and C Atkin. A simplified mathematical model for thrombin generation. *Med Eng Phys*, 36(2):196–204, 2014.

[116] Alessio Alexiadis. The discrete multi-hybrid system for the simulation of solid-liquid flows. *PLoS ONE*, 10(5):1–26, 2015.

[117] M. Ariane, W. Wen, D. Vigolo, A. Brill, F. G.B. Nash, M. Barigou, and A. Alexiadis. Modelling and simulation of flow and agglomeration in deep veins valves using discrete multi physics. *Computers in Biology and Medicine*, 89(May):96–103, 2017.

[118] I. D. Johnston, D. K. McCluskey, C. K.L. Tan, and M. C. Tracey. Mechanical characterization of bulk Sylgard 184 for microfluidics and microengineering. *Journal of Micromechanics and Microengineering*, 24(3), 2014.

[119] H. Hillborg and U.W. Gedde. Hydrophobicity recovery of polydimethylsiloxane after exposure to corona discharges. *Polymer*, 39(10):1991–1998, may 1998.

[120] Dhananjay Dendukuri, Shelley S Gu, Daniel C Pregibon, T Alan Hatton, and Patrick S Doyle. Stop-flow lithography in a microfluidic device. *Lab on a chip*, 7(7):818–828, 2007.

[121] Camille Duprat, Hélène Berthet, Jason S Wexler, Olivia du Roure, and Anke Lindner. Microfluidic in situ mechanical testing of photopolymerized gels. *Lab on a chip*, 15(1):244–52, 2014.

[122] Jason S. Wexler, Philippe H. Trinh, Helene Berthet, Nawal Quennouz, Olivia du Roure, Herbert E. Huppert, Anke Linder, and Howard a. Stone. Bending of elastic fibres in

viscous flows: the influence of confinement. *Journal of Fluid Mechanics*, 720:517–544, 2013.

[123] Sanjeev Palta, Richa Saroa, and Anshu Palta. Overview of the coagulation system. *Indian journal of anaesthesia*, 58(5):515–523, 2014.

[124] J. C. Dainty. The statistics of speckle patterns. *Progress in Optics*, 14(C):1–46, 1977.

[125] William Thielicke and Eize J. Stamhuis. PIVlab – Towards User-friendly, Affordable and Accurate Digital Particle Image Velocimetry in MATLAB. *Journal of Open Research Software*, 2, oct 2014.

[126] Michael G. Olsen and Ronald J. Adrian. Brownian motion and correlation in particle image velocimetry. *Optics and Laser Technology*, 32(7-8):621–627, 2000.

[127] L. Cipelletti, G. Brambilla, S. Maccarrone, and S. Caroff. Simultaneous measurement of the microscopic dynamics and the mesoscopic displacement field in soft systems by speckle imaging. *Optics Express*, 21(19):22353, 2013.

[128] Christophe Geuzaine and Jean-François Remacle. Gmsh: A 3-D finite element mesh generator with built-in pre- and post-processing facilities. *International Journal for Numerical Methods in Engineering*, 79(11):1309–1331, sep 2009.

[129] Tiina Sikanen, Thomas Zwinger, Santeri Tuomikoski, Sami Franssila, Reijo Lehtiniemi, Carl Magnus Fager, Tapio Kotiaho, and Antti Pursula. Temperature modeling and measurement of an electrokinetic separation chip. *Microfluidics and Nanofluidics*, 5(4):479–491, 2008.

[130] CSC. Elmer GUI Tutorials. 2014.

[131] Arianna Marucco, Ivana Fenoglio, Francesco Turci, and Bice Fubini. Interaction of fibrinogen and albumin with titanium dioxide nanoparticles of different crystalline phases. *Journal of Physics: Conference Series*, 429(1), 2013.

[132] C A Burtis, E R Ashwood, and D E Bruns. *Tietz Textbook of Clinical Chemistry and Molecular Diagnostics - E-Book*. Elsevier Health Sciences, 2012.

[133] Janice T Busher. Serum Albumin and Globulin. In HK Walker, WD Hall, and Hurst JW, editors, *Clinical Methods: The History, Physical and Laboratory Examinations*, chapter 101. Butterworths, Boston, 3rd editio edition, 1990.

[134] Michael Reth. Matching cellular dimensions with molecular sizes. *Nature Immunology*, 14:765, jul 2013.

[135] Harold P. Erickson. Size and shape of protein molecules at the nanometer level determined by sedimentation, gel filtration, and electron microscopy. *Biological Procedures Online*, 11(1):32–51, 2009.

[136] R. Asselta, S. Duga, and Maria Luisa Tenchini. The molecular basis of quantitative fibrinogen disorders. *Journal of Thrombosis and Haemostasis*, 4(10):2115–2129, 2006.

[137] N. M. Reddy, D. Kothandan, S. C. Ligam, and A. Ahmad. A Study on Refractive Index of Plasma of Blood of Patients Suffering from Tuberculosis. *International Journal of Innovative Technology and Creative Engineering*, 2(8):23–25, 2012.

[138] Yi Cao. The Toxicity of Nanoparticles to Human Endothelial Cells. pages 59–69. 2018.

[139] Ulrich J.H. Sachs and Bernhard Nieswandt. In vivo thrombus formation in murine models. *Circulation Research*, 100(7):979–991, 2007.

[140] Smbat Amirbekian, Robert C. Long, Michelle A. Consolini, Jin Suo, Nick J. Willett, Sam W. Fielden, Don P. Giddens, W. Robert Taylor, and John N. Oshinski. In vivo assessment of blood flow patterns in abdominal aorta of mice with MRI: implications for AAA localization. *American Journal of Physiology-Heart and Circulatory Physiology*, 297(4):H1290–H1295, oct 2009.

[141] G Heinze. Whole blood viscosity , plasma viscosity and erythrocyte aggregation in nine mammalian species : reference values and comparison of data Experimental Physiology :. 2007.

[142] A. C. Riches, J. G. Sharp, D. Brynmor Thomas, and S. Vaughan Smith. Blood volume determination in the mouse. *The Journal of Physiology*, 228(2):279–284, 1973.

[143] R. Mehri, E. Niazi, C. Mavriplis, and M. Fenech. An automated method for dynamic red blood cell aggregate detection in microfluidic flow. *Physiological Measurement*, 39(1), 2018.

[144] R Rhoades and D R Bell. *Medical Physiology: Principles for Clinical Medicine*. Lippincott Williams & Wilkins, 2009.

[145] Brian Nesbitt. *Handbook of Valves and Actuators: Valves Manual International*. ButterHeinem ST (25 Jun. 2007), 2007.

[146] Ruiqing Hu, Fen Li, Jiaqi Lv, Ying He, Detang Lu, Takashi Yamada, and Naoki Ono. Microfluidic analysis of pressure drop and flow behavior in hypertensive micro vessels. *Biomedical Microdevices*, 17(3):1–9, 2015.

[147] James R. Byrnes and Alisa S. Wolberg. Red blood cells in thrombosis. *Blood*, 130(16):blood–2017–03–745349, 2017.

[148] J Geddings, M M Aleman, A Wolberg, M L von Brühl, S Massberg, and N Mackman. Strengths and weaknesses of a new mouse model of thrombosis induced by inferior vena cava stenosis: Communication from the SSC of the ISTH. *Journal of Thrombosis and Haemostasis*, 12(4):571–573, 2014.

[149] Mano J. Thubrikar and Francis Robicsek. Pressure-induced arterial wall stress and atherosclerosis. *The Annals of Thoracic Surgery*, 59(6):1594–1603, 1995.

[150] Kytai Truong Nguyen and Jennifer L. West. Photopolymerizable hydrogels for tissue engineering applications. *Biomaterials*, 23(22):4307–4314, 2002.

[151] Kathryn McAvoy, David Jones, and Raghu Raj Singh Thakur. Synthesis and Characterisation of Photocrosslinked poly(ethylene glycol) diacrylate Implants for Sustained Ocular Drug Delivery. *Pharmaceutical Research*, 35(2), 2018.

[152] Xing Zhang, Bin Xu, Daniel S. Puperi, Aline L. Yonezawa, Yan Wu, Hubert Tseng, Maude L. Cuchiara, Jennifer L. West, and K. Jane Grande-Allen. Integrating valve-inspired design features into poly(ethylene glycol) hydrogel scaffolds for heart valve tissue engineering. *Acta Biomaterialia*, 14(1):11–21, mar 2015.

[153] Roberta Caroline Bruschi Alonso, William Cunha Brandt, Eduardo Jose Carvalho Souza-Junior, Regina Maria Puppin-Rontani, and Mário Alexandre Coelho Sinhoreti. Photoinitiator concentration and modulated photoactivation: influence on polymerization characteristics of experimental composites. *Applied Adhesion Science*, 2(1):1–11, 2014.

[154] Quynhhoa T. Nguyen, Yongsung Hwang, Albert C. Chen, Shyni Varghese, and Robert L. Sah. Cartilage-like mechanical properties of poly (ethylene glycol)-diacrylate hydrogels. *Biomaterials*, 33(28):6682–6690, oct 2012.

[155] Author Manuscript, Coagulation Biology, Steven Pavletic, Thierry Martin, Alberto Marmont, and Riccardo Saccardi. NIH Public Access. 70(12):2071–2074, 2014.

[156] P.C. Malone. The aetiology of deep venous thrombosis. *QJM*, 99(9):581–593, aug 2006.

[157] Wei Hsin Tien, Henry Y. Chen, Zachary C. Berwick, Joshua Krieger, Sean Chambers, Dana Dabiri, and Ghassan S. Kassab. Hemodynamic coupling of a pair of venous valves. *Journal of Vascular Surgery: Venous and Lymphatic Disorders*, 2(3):303–314, 2014.

[158] Takeshi Karino and Mineo Motomiya. Copyright (c) lS84 Pergamon Press Ltd . All rights reserved . by Editor J . Hawiger). (c):245–257, 1984.

[159] Jevgenia Zilberman-Rudenko, Joanna L. J.L. Sylman, Hari H.S. H.H.S. Lakshmanan, Owen J.T. O.J.T. McCarty, and Jeevan Maddala. Dynamics of Blood Flow and Thrombus Formation in a Multi-Bypass Microfluidic Ladder Network. *Cellular and Molecular Bioengineering*, 10(1):16–29, 2017.

[160] Michael J. Sherratt. Tissue elasticity and the ageing elastic fibre. *Age*, 31(4):305–325, 2009.

[161] Takuji Ishikawa, Shuzo Oshima, and Ryuichiro Yamane. Vortex enhancement in blood flow through stenosed and locally expanded tubes. *Fluid Dynamics Research*, 26(1):35–52, 2000.

[162] Charles T. Esmon. Basic mechanisms and pathogenesis of venous thrombosis. *Blood Rev*, 23(5):225–229, 2009.

[163] S. Mueller, E. W. Llewellin, and H. M. Mader. The rheology of suspensions of solid particles. *Proceedings of the Royal Society A: Mathematical, Physical and Engineering Sciences*, 466(2116):1201–1228, apr 2010.

APPENDIX A

APPENDIX

A.1 Chapter 2

The following is an example of the .sif code used with Elmer finite element multi-physics software. Each section is spaced and commented in green.

Loads the mesh into the Elmer software, creates space to put results. It is important to keep mesh, geometry and elmer .sif document in the same folder

Header

CHECK KEYWORDS Warn

Mesh DB "." "."

Include Path ""

Results Directory ""

End

Sets the controls. The simulation is steady state as it will not change over time. The section also the name of the results file which is set to .vtu to analyse in paraview. It also selects the .sif file in which to compute the results. coordinate mapping is set 1, 2, 3 for x, y, z this can be altered depending on the orientation of the geometry when inputted into Elmer. The other parameters are default

Simulation

Max Output Level = 5

Coordinate System = Cartesian

Coordinate Mapping(3) = 1 2 3

Simulation Type = Steady state

Steady State Max Iterations = 1

Output Intervals = 1

Timestepping Method = BDF

BDF Order = 1

Solver Input File = case.sif

Post File = case.vtu

End

Applies all the constants

Constants

Gravity(4) = 0 -1 0 9.82

Stefan Boltzmann = $5.67e^{-08}$

Permittivity of Vacuum = $8.8542e^{-12}$

Boltzmann Constant = $1.3807e^{-23}$

Unit Charge = $1.602e^{-19}$

End

Target body is the physical groups determined in gmsh, and the rest states the number of equations used/surfaces and materials used in this particular simulation

Body 1

Target Bodies(1) = 4

Name = "Body 1"

Equation = 1

Material = 1

End

Use of solvers within the Elmer package. Options to add bubbes, destabilisation of the fluid, lumped mass (useful for emulating a thromus). It is possible to alter number iterations

Solver 1

Equation = Navier-Stokes

Procedure = "FlowSolve" "FlowSolver"

Variable = Flow Solution[Velocity:2 Pressure:1]

Exec Solver = Always

Stabilize = True

Bubbles = False

Lumped Mass Matrix = False

Optimize Bandwidth = True

Steady State Convergence Tolerance = $1.0e^{-5}$

Nonlinear System Convergence Tolerance = $1.0e^{-7}$

Nonlinear System Max Iterations = 200

Nonlinear System Newton After Iterations = 30

Nonlinear System Newton After Tolerance = $1.0e^{-3}$

Nonlinear System Relaxation Factor = 1

Linear System Solver = Iterative

Linear System Iterative Method = BiCGStab

Linear System Max Iterations = 5000

Linear System Convergence Tolerance = $1.0e^{-10}$

BiCGstabl polynomial degree = 2

Linear System Preconditioning = Diagonal

Linear System ILUT Tolerance = $1.0e^{-3}$

Linear System Abort Not Converged = False

Linear System Residual Output = 1

Linear System Precondition Recompute = 1

End

Equation used in the solver

Equation 1

Name = "navier stoke"

Active Solvers(1) = 1

End

Starting with an ideal fluid is useful to test the simulation before adding the parameters of water, this is an in built material to chose from

Material 1

Name = "ideal"

Viscosity = 0.01

Density = 1.0

End

The boundary conditions can be labelled and physical parameters can be added here

Boundary Condition 1

Target Boundaries(1) = 1

Name = "Inlet"

Velocity 1 = 0.1

Velocity 2 = 0.0

End

Boundary Condition 2

Target Boundaries(1) = 2

Name = "Oultet"

Velocity 2 = 0.0

End

Boundary Condition 3

Target Boundaries(1) = 3

Name = "Wall"

Noslip wall BC = True

End

A.2 Chapter 3: Stenosis Model

Reports were created using the COMSOL software including information about the mesh, the equations used and the results. The folder is available upon request.

A.3 Chapter 4: Bypass Model

Comparison between the two positions B and C with the side branch width of 100 μm.

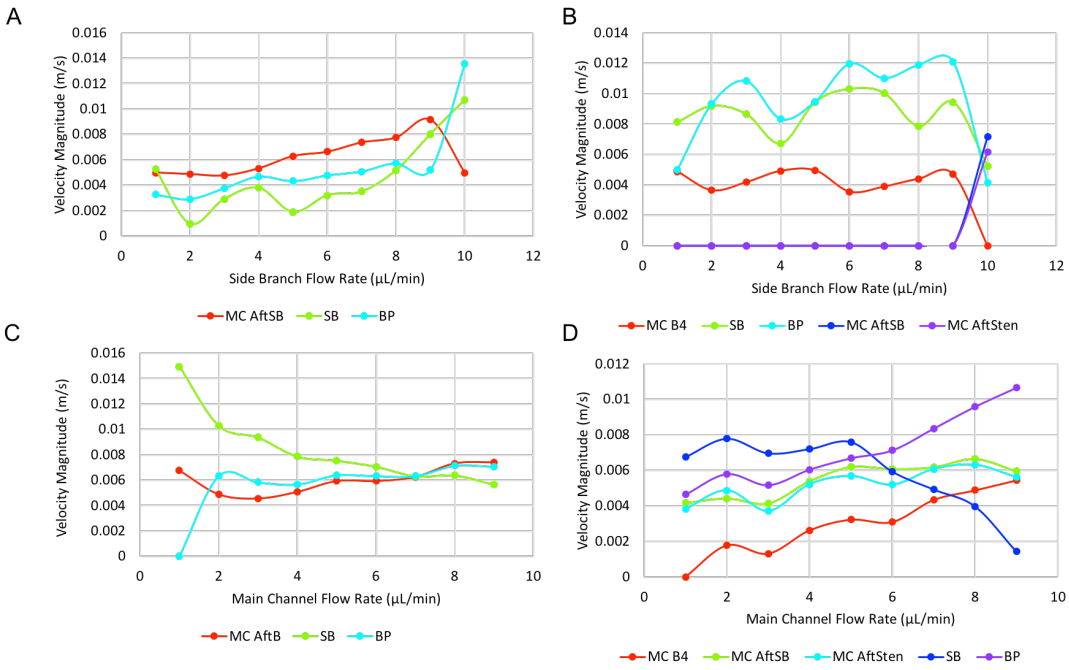

Figure A.1: Comparison between the two positions B and C. Plots A and C show position B side branch and main channel flow rates respectively and plot B and D show position C side branch and main channel flow rates changing.

A.4 Chapter 5: Valve Model

The following figure A.2 is further evidence of the varied velocities through and around the valves.

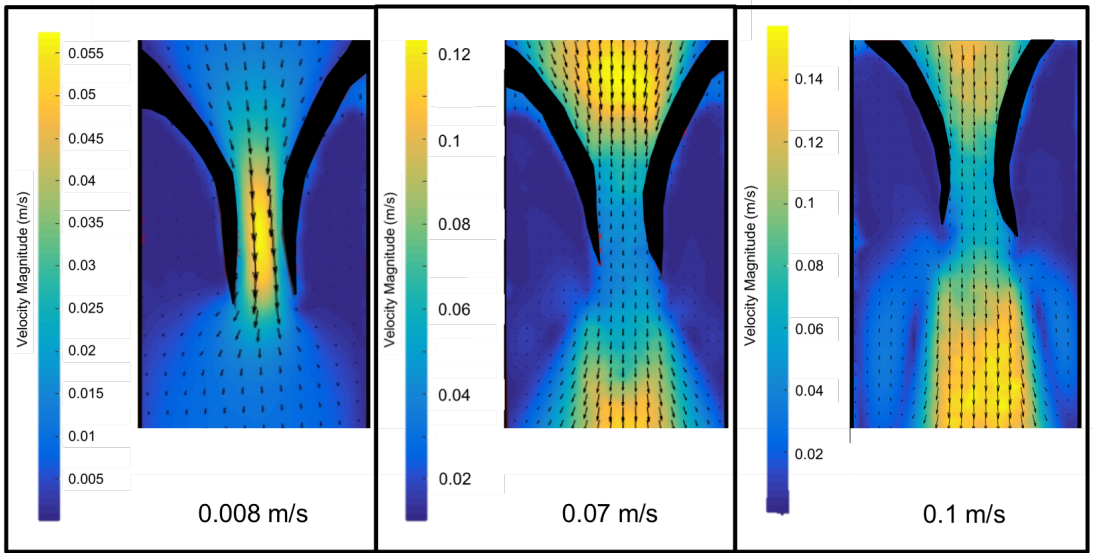

Figure A.2: An example of the different velocities around the valve, indicating the stagnant region behind the valve as well as the fast region through the centre.